Modeling and Control Perspectives of Two-Phase Fluid Systems

with Applications to Bubble Columns

Snezana Djordjevic

Modeling and Control Perspectives of Two-Phase Fluid Systems

with Applications to Bubble Columns

Proefschrift

ter verkrijging van de graad van doctor
aan de Technische Universiteit Delft,
op gezag van de Rector Magnificus prof.ir. K.C.A.M. Luyben,
voorzitter van het College voor Promoties,
in het openbaar te verdedigen op
maandag 27 juni 2011 om 15:00 uur

door

Snezana DJORDJEVIC
ingenieur in de biotechnologie
geboren te Novi Sad, Servië

Dit proefschrift is goedgekeurd door de promotoren:
Prof.dr.ir. P.M.J. Van den Hof
Prof.ir. O.H. Bosgra

Samenstelling promotiecommissie:

Rector Magnificus	voorzitter
Prof. dr. ir. P.M.J. Van den Hof	Technische Universiteit Delft, promotor
Prof. ir. O.H. Bosgra	Technische Universiteit Delft, promotor
Prof. dr. H.A. Preisig	Norwegian University of Science and Technology
Prof. dr. ir. J.M.A. Scherpen	Rijksuniversiteit Groningen
Prof. dr. ir. M. Steinbuch	Technische Universiteit Eindhoven
Prof. dr. R.F. Mudde	Technische Universiteit Delft
Dr.ing. D. Jeltsema	Technische Universiteit Delft
Prof.dr.ir. R.A.W.M. Henkes	Technische Universiteit Delft, reservelid

This thesis has been completed in partial fulfillment of the requirements of the Dutch Institute of Systems and Control for graduate studies. The research described in this thesis was supported by Delft Centre for Sustainable Industrial Processes, Delft University of Technology.

Published and distributed by: Snezana Djordjevic
E-mail: S.Djordjevic@tudelft.nl

ISBN 978-90-8570-767-7

Keywords: microscopic conservation laws, control-oriented modeling of hydrodynamics, boundary actuation, spatially distributed control.

Printed by Wöhrmaan Print Service, Zutphen, The Netherlands

Preface

This thesis is the result of my research during the period from 2006 to 2011 at the Delft Center for Systems and Control, Delft University of Technology, The Netherlands. This thesis describes the research done in the field of modeling and control of fluid flow systems that can be used for future developments in the chemical industry. This thesis contributes to the field and would never have seen light without the support of my promoters, colleagues, and friends who guided me through difficult and frustrating moments during this research period.

Firstly, I am deeply grateful to my promoter Prof. Paul Van den Hof for giving me the opportunity to work on this challenging topic, and for the trust and freedom that he gave me in the course of five years. I also wish to express my deepest gratitude to my second promoter Prof. Okko Bosgra for his extraordinary help and endless patience, without which this work would not have been possible. I also would like to thank Dr. Dimitri Jeltsema for valuable comments on the research material and for always questioning the mathematical descriptions and dynamics of physical phenomena. I am also grateful to Prof. Thomas Bewley for opening the doors of the Flow Control Lab for me at the University of California, San Diego, USA, in 2007. I would like to thank all my colleagues at the Delft University of Technology, Eindhoven University of Technology, and University of California, San Diego, who supported me during this research period and gave me numerous reasons to smile.

Secondly, I would like to thank my ex-Yugoslavian friends in The Netherlands for reminding me that life is more than a conference paper or “a well-posed boundary condition”, and for bringing a piece of home to The Netherlands. I would like to thank all of my Dutch and international friends who showed me differences and similarities between societies and people all over the world.

And finally, I would like to thank my brother Dragan and my family for their unconditional support and everlasting care. I can say in the end that this Ph.D. period was an incredible life journey filled with opportunities, stress, happiness, and struggles that tested my courage.

Snezana Djordjevic
The Netherlands, June 2011

”The purpose of life is to live it, to taste experience to the utmost, to reach out eagerly and without fear for newer and richer experience.”
- Eleanor Roosevelt-

Contents

Chapter 1

Introduction and Problem Formulation

The most recent demands for the development of sustainable solutions in the chemical industry encourage multidisciplinary research which is oriented towards improving process performance with minimum energy consumption and low environmental risks. Operating processes with high efficiency and low operational costs per unit volume on different scales becomes increasingly important. The key challenge in developing suitable solutions is to establish a multiscale technology that can intensify production processes with low environmental risks. Successful implementation of the multiscale technology will eventually lead to sustainable solutions in the chemical industry. This thesis contributes to the developments in this area by introducing different scales of modeling chemical processes using a control-oriented modeling approach to fluid flow systems inside chemical reactors. This introductory chapter provides a brief overview of the issues related to modeling chemical processes on different scales, current modeling problems related to hydrodynamics, and opportunities for future developments in the chemical industry.

1.1 Developments in Chemical Engineering

Under the influence of unprecedented market demands in the petroleum, pharmaceutical, food, and cosmetic industries, the chemical industry has evolved considerably over the last two decades. Following the demands and achievements made in these fields, plant capacities have greatly increased, incorporating new technologies to maintain the enlargement. Most of the new technologies have relied on developments from different fields such as: material science (safe construction of large-size reactors and pipes), mechanical engineering (construction of agitators that enhance the mixing of reactants), chemical engineering (decreasing process time and increasing productivity), and control engineering (safe regulation of pressure and temperature inside the reactors). However, operating chemical processes in an optimal and safe manner is almost impossible for some production processes on the large scale (e.g., mixing inside large-scale reactors, transportation of fluid in long pipelines, distribution of particles in crystallizers, or pressure distribution in distillation columns). These production-related problems cannot be effectively solved with the current reactor design and are still not scaled-up to the optimal volume. Due to the complex nature of the chemical processes and equipment designs, the ability to build plants “a bit bigger” is slowly reaching its limitations [22]. This dictates a growing need to replace current large, expensive, and energy-intensive equipment with smaller, less costly, and more efficient equipment for an optimal production process. In order to be able to replace the current large-scale equipment and to scale-up a plant more efficiently, a better understanding and more accurate mathematical descriptions of the process dynamics are needed. It is, therefore, exceedingly important to derive an accurate mathematical description of a chemical process that can predict the future behavior of the process and can be used for control design. This approach to chemical processes is known as model-based control design. The philosophy behind the model-based control approach is that the process can be manipulated by exploiting the ability of a model to predict the behavior of a process and influence the dynamics in a desirable manner.

This thesis contributes to the developments in the area of model-based control strategy of chemical processes through the introduction of a microscopic scale with a wide range of possible actuation strategies. The main contribution of this project is in the development of a microscopic model-based control approach to two-phase flow inside bubble column reactors with different spatially distributed control strategies to influence the flow. Furthermore, this thesis proposes various control objectives and control designs that can be used to operate fluid flow systems under different flow regimes. The modeling and control perspectives of fluid flow systems are studied on two numerical examples: single-phase and two-phase fluid flow. The main contribution of this thesis is in the control-oriented microscopic approach to the fluid flow inside a chemical reactor, which provides a new way of thinking about the purposes of models in chemical engineering, the relationship between the mass and flow properties in the reactors, and the level of details needed for control designs.

1.2 Mathematical Description of Chemical Processes

1.2.1 Material Properties

The mathematical description of a chemical process plays an important role in the engineering design and operation of the process in modern chemical design. Basic prerequisites for a model-based representation of a process include a thorough analysis of the chemical and physical properties of pure components, transformation of the components in a system of mixtures, ways that the process can be influenced, and available measurement techniques. A model of a chemical process is usually based on mass and energy balance equations observed in each unit (e.g., reactors, separation vessels, filters). The units are integrated into a production network and operate through a process simulator by manipulating the process variables. Since the manipulation of the system is based on models embedded into the process simulators, this means that the production can be both influenced and significantly improved by improving the models used to describe the process. For the model-based scale-up and control design in the chemical industry, it is essential to specify the characteristic length at each scale. The process performance and productivity on different scales improved in such a way eventually leads to more efficient and sustainable productions where a process is intensified over the spatial, temporal, thermodynamical, and functional domain [97]. Factors that have to be considered in order to improve the performance and productivity of a chemical process are transfer rates of mass, momentum, and heat among the components involved in the process.

However, due to the different scales of modeling chemical processes as illustrated in Figure 1.1, the level of model complexity increases as one decreases the characteristic length of observation (i.e., “zooming in”) of material properties. Before we introduce the model complexity, it is important to study the chemical and physical phenomena that exist on different scales, including the model requirements for a model-based control design on each scale.

1.2.2 Modeling Scales

Three different scales are commonly used in chemical process engineering: the plant, reactor, and microscopic scale. Figure 1.1 roughly illustrates those scales. Currently used models in the chemical industry are derived on the reactor or plant scale. The models derived on the reactor or plant scale do not take into account the spatial variation of material properties which can be observed only on the microscopic scale. The reason for this lies in the complex nature of microscopic phenomena that exist on the microscopic scale, which requires advanced analysis. However, the microscopic model-based approach to chemical processes gives a spatially distributed mathematical description of chemical properties and provides a wide range of different actuation strategies. This will be further discussed in Chapter 2. Here, we will briefly outline the scales and major design issues.

1. **Plant scale**

   Chemical plants use a wide range of equipment where materials flow throughout the process, starting as feeds and ending up as products. The models used to describe the flow of material are based either on mass balance equations to model flow between the units or on empirical correlations between material properties that are usually obtained from experiments [94].

2. **Reactor scale**

   On this scale, the process is assumed to be well-mixed or without any variation of the flow properties with respect to space. There are three basic reactor types according to operating modes: batch reactor, continuous stirred-tank reactor (CSTR), and plug flow reactor (PFR). The process behavior inside these

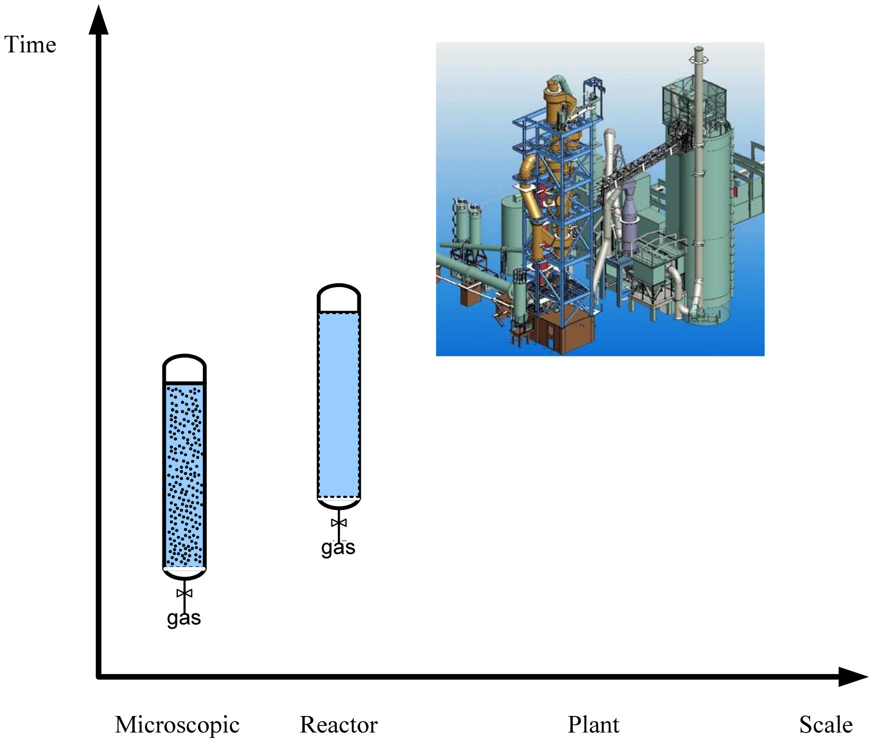

Figure 1.1: Different levels of modeling chemical processes.

reactors is fully determined by the operating mode and properties of the reactants. The reactants include pure fluid or solid components, or a mixture of both. In all three types of reactors, the reactants move inside the reactors creating different flow patterns. The flow patterns cannot be observed on this scale because the material property is assumed to be spatially uniform. Correction of models for flow variation obtained on this scale is done by introducing different correlation factors between flow variables and material parameters for each reactor separately [59, 94].

3. **Microscopic scale**

   A detailed picture of a chemical process can be obtained on the microscopic scale. The process inside the reactor is viewed during the course of the kinetics, mass transfer, hydrodynamics, and heat transfer that occur between components on this scale. However, the downside to modeling on this scale is that the microscopic scale requires not only an increased level of scientific understanding and engineering enhancement, it also requires further advancement in the modeling approach to physical and chemical phenomena which can only be found in the microscopic world. One of the most important properties which can be observed on this scale is the velocity of components, i.e., velocity field. In principle, a velocity field describes different flow patterns which occur in different operating modes. Due to the fact that we can observe the motion of all components, i.e., phases inside a reactor, these systems are also known as systems in motion or multiphase flow systems. The knowledge and techniques used to solve models of fluid flow on the microscopic scale are known as computational fluid dynamics (CFD) [4]. Using the CFD models allows for a rather accurate determination of the velocity field of the entire reactor volume for each component separately or for the whole mixture of components. Deviations and fluctuations of fluid flow properties in CFD models are observed dynamically with respect to space. This, in itself, gives a rather accurate description of physical phenomena on the microscopic scale because this unique aspect of the microscopic models increases possibilities to improve productivity and efficiency per unit volume. On the other hand, due to the complex nature of the physical phenomena on the microscopic scale, the microscopic models are computationally rather involved, which explains why the microscopic models have not yet been used in the chemical industry. The microscopic models have been mostly limited to a few academic examples (e.g., the heated plate and the flow of reactants in a plug flow reactor). In recent years, a great effort has been devoted to modeling different phenomena on the microscopic scale (e.g., convective transport, diffusion, and friction) and to the development of related numerical methods to solve model equations. This is due to the high interest in understanding and manipulating the mixing of the fluid, which can be observed only on the microscopic scale. This will be discussed in detail in Chapter 2.

1.2.3 Model Complexity

In this section, we will emphasize the complexity of the mathematical description of chemical processes on different scales. A mathematical description of a chemical process is usually based on conservation laws of mass, momentum, and energy. Depending on the scale and system boundaries, the models are formulated by a set of ordinary differential equations (ODEs) for spatially uniform processes on the plant and reactor scale, or a set of partial differential equations (PDEs) for spatially non-uniform processes on the microscopic scale. The non-uniformity is related to the spatial distribution of the material properties. This means that the PDE models govern variations of the material properties with respect to time and space. Besides the equations obtained by first principles modeling, some chemical processes involve constitutive and constraint equations which usually lead to a set of differential algebraic equations (DAEs) for the time variation only, and a set of partial differential algebraic equations (PDAEs) for time and space variations. This will be further discussed in Chapter 2.

In general, PDE/PDAE models are more accurate compared to ODE/DAE models. The PDE models allow engineers to improve on existing designs and to understand the influences of physical parameters on the product quality on the microscopic scale. Consequently, the PDE models can be used to manipulate the mixing of fluid, concentration of chemical components, and other microscopic properties on the microscopic level. However, the PDE models, in particular the CFD models, require a comprehensive knowledge of detailed geometric design, numerical methods, the mathematics behind different types of PDEs and extensive modeling effort. This all makes the CFD models complex and computationally involved. Depending on the complexities of the models, it is generally quite difficult to obtain fast simulation models that can be used for real-time control designs.

The development of CFD models is commonly done using commercially available software packages, and it consists of the following steps:

1. *Pre-processing.* In this step, the spatial domain, shapes, and discrete grid divisions have to be defined. In order to approximate the continuous behavior, CFD models are solved numerically where the spatial domain is divided into many grid cells. The number of grid cells in the CFD models are typically in the range of 10^2 to 10^{15} grid cells [72]. This means that the CFD software has to simultaneously solve 10^2 to 10^{15} equations for every time step. Advanced CFD packages usually have a default mesh generator for solving fluid equations (see Section 2.2.3). In this step, it is necessary to specify initial and boundary conditions. As far as the system parameters are concerned, most of the software packages have a database of physical parameters, such as density, viscosity, and heat conductivity with temperature dependence for a wide range of reactants, which simplifies the modeling of fluid systems.

2. *Solving.* This is the most demanding part of the CFD algorithms since it involves discretization of the governing equations, selection of the solvers and numerical algorithms, and iterative calculations needed to solve discretized equations. The computations can take from a few minutes up to a few days or even weeks. This step became shorter with the development of high speed computers, but it is still far from the real-time computation offered by most on-line applications in the chemical industry.

3. *Post-processing.* In this step, the results of the simulations can be visualized in each grid point in graphical interfaces in one-dimensional (1D), two-dimensional (2D) and three-dimensional (3D) plots at all time steps. The simulation results can also be exported to data files for further manipulation and model analysis.

All the above steps are very complex and computationally involved. However, with high speed computers, the number of CFD packages has increased over the last few years. FLUENT, COMSOL (formerly FEMLAB), ANSYS, FEMtools, CD - ADAPCO, and CFX are just a few of the most commonly used software packages for simulation of fluid flow. These packages include static and dynamic structural analysis with linear and nonlinear solvers embedded as an integral part of the software. The choice of software usually depends on the required accuracy and available examples.

Most of the available software packages use different solution routines to shorten the computation time. One of the first routines was developed in FORTRAN and C++. Those programs still offer a wide range of well-worked out examples. The existing routines can be used to modify the CFD models for any particular application or to build new models.

FLUENT plays a central role in the fluid flow engineering design of all the above-mentioned software packages. It has become an essential tool for simulation of fluid flow with a large library of engineering problems, ranging from the chemical industry and oil refineries to the construction of vehicles and buildings. FLUENT's strongest point is its ability to solve problems involving complicated physical phenomena allowing other programs, such as GAMBIT, to design different shapes and complex geometries. The CFD community has tailored different complex geometries using different numerical techniques, and uploaded them to the libraries for FLUENT's users. The main shortcoming of this package is that it does not support most of the chemical and control engineering software.

Another CFD package that recently started to be extensively used in chemical engineering is COMSOL Multiphysics. The COMSOL Multiphysics package is a finite element analysis and solver package for simulating various physics and engineering applications. COMSOL Multiphysics also offers an interface with MATLAB and its toolboxes. This allows for a large variety of programming, pre-processing and post-processing possibilities which can be very beneficial for control design.

Despite the fact that there is a wide range of CFD packages, it seems that we are still far away from implementing developed theory on practical setups. The CFD models are generally too slow and too large to be used in on-line control designs and real-time prediction of fluid motion. Consequently, the applicability of CFD in control design is currently rather limited even with fast computers. For control design, it is exceedingly important to solve the model equations faster than the real-time changes. In this way, the controllers have time to take an action and influence the future system behavior. In addition, fast models are beneficial not only for the control design, but also for on-line tuning of the process parameters and process conditions. This opens new research directions, putting the current flow design into a new control-oriented perspective.

1.3 Control-Oriented Modeling

1.3.1 Input/Output Structures

The strongest connection between control and chemical engineering is shown in the modeling of physical systems and developing tools to simulate the models. However, one of the fundamental differences between control-oriented modeling and modeling in other disciplines lies in modeling interactions between properties. Whereas modeling in other disciplines relies on the balance equations and closure equations that form a set of solutions, the model-based control framework relies on a type of input/output modeling that allows one to influence the system behavior (e.g., regulations, optimization, and disturbance attenuation). Generally speaking, an input/output structure describes variations of outputs (i.e., measured quantities) with respect to inputs (i.e., manipulated variables). As far as different modeling scales are concerned, the input/output structure depends on the selected modeling scale and operating modes. For example, a process on the reactor scale is usually controlled through the regulation of valve positioning at the vassal boundaries for the fluid transportation, regulation of temperature, manipulation of pressure, and concentration of the material transformed throughout the system. In the early days, control engineers used simple controllers, such as proportional-integral-derivative (PID) controllers, to influence chemical processes. The PID controller minimizes the difference between a measured process variable and a desired set-point which stabilizes the overall process around the chosen set-point. The models used in control design were obtained from the simple balance equations and empirical correlations within a control loop. The control loop can be classified on the basis of their properties as: flow, pressure, liquid level, product quality, and temperature control loop. Following developments in the control field over the last few decades, more powerful control techniques have been developed and used in the chemical industry. A typical example is the use of advanced models in the petrochemical industry and the application of model-based predictive control (MPC) design, which improves the purity of some products by 1-5% and yields a very important annual profit per operational unit [20].

The model-based control design involves defining the following tasks:

1. selection of manipulated variables (i.e., inputs),
2. selection of controlled variables (i.e., outputs),
3. selection of a control configuration (i.e., structure of the overall controller that interconnects the manipulated and controlled variables), and
4. selection of controllers for the model which is derived from the first principles.

Any future developments of the modeling tools should be aimed at providing additional knowledge about how to influence the process, how to enhance process performances with minimal effort and a maximal production rate, and how to operate processes on the microscopic scale with higher efficiency. To influence the process in an optimal manner on the microscopic scale, a systematic approach to complex fluid systems is needed. This means that a control-oriented model of a fluid system has to be developed in order to control macroscopic phenomena and scale down current large-scale reactors. This thesis contributes to the development of control-oriented fluid flow systems by studying the two-phase flow inside bubble column reactors, which appear in a wide range of chemical processes.

1.3.2 Two-Phase Fluid Flow

Many examples involving two-phase fluid flow systems appear in the chemical industry, such as the partial oxidation of ethylene to acetaldehyde (i.e., the Wacker-Hoechst process) or the carbonization of methanol to acetic acid. Other occurrences of two-phase flow appear in the injection of steam into oil wells for enhanced oil recovery, in the condensation of higher hydrocarbons, in natural gas pipelines due to low temperatures of surrounding air or soil, in a boiling water nuclear reactor, and in fermentors for the production of enzymes and drugs. For a more extensive overview, we refer to [35].

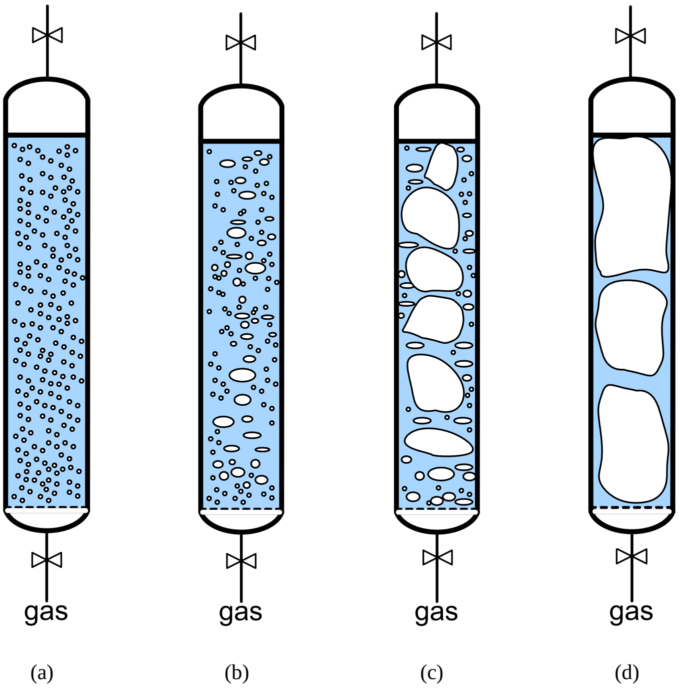

(a) (b) (c) (d)

Figure 1.2: Flow patterns in a vertical bubble column: (a) bubble, (b) bubble-slug transition, (c) slug, and (d) annular.

All these processes take place in reactors that are often referred to as bubble column reactors. As shown in Figure 1.2, a bubble column reactor is a vertical cylinder, where a gas phase enters at the bottom of the column through a gas distributor. The column is filled with liquid which expands under the influence of the gas injection. Different flow regimes can be created on the microscopic scale depending on the magnitude of the gas injection. Figure 1.2 shows different flow regimes and levels of coalescence of bubbles present in the column on a microscopic scale. In the bubble flow, the gas consists of discrete bubbles immersed in the liquid phase that moves against the gas flow. Increasing the gas injection or pressure at the top of the column, these small bubbles coalesce into slugs. The transition from bubble flow (Figure 1.2(a)) towards annular flow (Figure 1.2(d)) depends on the size of the bubbles, injection techniques, and surface-tension effects. The large number of bubbles, which can coalesce into slugs, increases the gas volume fraction and decreases the presence of the liquid phase. Consequently, the gap between the gas and the wall narrows, thus the downward flow dominates the column. This causes a rather strong relative velocity between the gas and the liquid phase. As shown in Figure 1.2(c), the coalescing effect caused by different flow regimes inside the bubble column can be observed only on the microscopic scale.

On the reactor scale, the coalescing of the bubbles into slugs is mainly observed in decreased production rates.

Although the bubble column reactor is characterized by the lack of any mechanical means of agitation, due to the large contact area between the phases, bubble flow is particularly efficient from a mass and energy transfer point of view. The transfer rates are mainly determined by the size of the contact area, the circulation rates of the liquid and gas phase, and can be increased by enlarging the contact area between the phases. A poor liquid circulation has an adverse effect on the transfer rate and residence time of the gas phase, whereas a well-circulated liquid phase increases the reactor volume. In reactor design, the main objective is to keep a large contact area between the phases while maintaining an ideal balance between those two extreme circulation phenomena. In this thesis, we will introduce a new microscopic modeling and control approach to the problem of two-phase fluid flow circulation inside bubble columns rectors.

1.3.3 Control Perspectives

As can be seen in Figure 1.2, the bubble column can operate under different flow regimes which can be observed only on the microscopic scale. These flow regimes depend on the magnitude of the gas injection at the bottom boundaries and the possible actuation strategies (e.g., injection from the bottom boundary, injection from the bottom boundary and side walls). In this setting, the injection strategy can be considered as an input strategy where the valves can be placed at different locations. This will be further discussed in Section 2.4. Furthermore, the operation of bubble columns can also be improved by adjusting the position of gas injection (e.g., bottom boundary, side walls, top boundary). The existing flow patterns inside bubble column reactors can be influenced, introducing additional gas injection and changing the actuation strategies (see Sections 2.4 and 6.2.3). Different actuation strategies can offer a wide range of bubble column designs that can operate with a high efficiency range, reduce reactor volume with minimal energy consumptions, and lead to more sustainable reactor designs. The spatially distributed actuation designs enable the adjustment of existing flows (e.g., plug flow), reduction or enhancement of liquid circulation, improvement of mixing performances, etc. Developing a control-oriented microscopic model that can suggest smart injection strategies can provide answers to the current challenges in the microscopic modeling of chemical processes. The control-oriented two-phase flow model will be introduced in Chapter 4.

1.4 Literature Overview

1.4.1 Introduction

In this section, we will provide an overview of the literature from the fluid community that deals with modeling issues of two-phase flow (i.e., multiphase flow), and the literature from the control community that works towards developing control tools for PDE models. An interdisciplinary perspective to this type of problem is very important to understand fluid systems, process dynamics and control perspective for future developments.

1.4.2 Microscopic Two-Phase Flow Models

The simplest microscopic models of two-phase flow (i.e., bubble flow) are developed under the assumption that the variation of mass is the only property that changes with respect to space, i.e., ideal flow (see Section 2.2.2). These models take into account flow with a constant velocity profile and deviation only in the concentration of the fluid component [3, 18, 36, 43, 95, 102]. The assumption on the uniform distribution of the property in space is rather reasonable because most of the practical applications aim for homogeneous regimes. However, the real flow always deviates from the ideal flow, which is caused by variation in the gas and liquid velocity over the space. By including the variation of the velocity field, a more accurate description of the fluid flow system is possible based on microscopic conservation laws.

Many contributions to the modeling of hydrodynamics of two-phase flow systems have been presented, some in general terms [32, 61] and many others specifically for bubble flow [16, 45]. The latter research ranges from fundamental [63] to more applied and phenomenological [61, 68]. Although the correct formulation of the basic two-phase flow models and the appropriate form of the closure equations have been widely discussed in the past [47, 80], so far no commonly agreed approach has been achieved. An exact description of the hydrodynamics in bubble columns is very difficult to formulate, not only because there are two phases present in the bubble column, but also because there is a strong interaction between the phases that causes turbulence on the microscopic level. A specific concern has been that most models currently used in the large computer codes are based on governing equations which have complex solutions, and therefore do not represent a mathematically well-posed model [80, 92]. We will also address this issue in Chapter 4. Nevertheless, there is common agreement that the pure fluid transport has to be governed by a set of hyperbolic PDEs [73]. This is a very important characteristic of the two-phase flow which will also be discussed in Chapter 4.

Review articles on modeling two-phase flow and the modeling issues are given in [49, 82, 101]. Despite the fact that the modeling of two-phase flow systems and the interaction between the phases have been presented in a large number of publications [47, 62, 83], the concept of causality and stability with respect to the boundary conditions have not yet been studied.

1.4.3 Model-Based Flow Control Designs

Most of the existing control literature that focuses on the problem of spatially distributed systems described by a set of PDEs makes use of special techniques that can either reduce the computational complexity or enforce distributed structure for control design [11, 31, 54, 88]. However, their applicability depends largely on the type of model under consideration (e.g., hyperbolic PDEs or parabolic PDEs) and model representation (e.g., the Fourier transformation or the Laplace transformation) [25].

Some publications on model-based control of the hydrodynamics recently appeared in the control community treating single-phase flow as a microscopic example [14]. In general, the motion of a single fluid is described by the Navier-Stokes equations, where the boundary conditions are considered as manipulated variables, i.e., spatially distributed input. The models include a simple geometry and different boundary conditions. Due to the different boundary conditions, the control literature developed different flow prototypes. The following geometries have been intensively studied: plane channel (one bounded direction and two periodic directions), pipe (two bounded directions and one periodic direction), and cavity flow (no periodic directions). For the channel and pipe flow, different control approaches have been published, starting with a linearized control approach [27, 28, 52, 53, 55, 56], towards more complex algorithms based on the optimal control theory [15]. For the cavity flow, open-loop and closed-loop strategies are usually based on either reduced models or experiments [21, 85–87], since steady-state solutions can be obtained only numerically.

For all the mentioned geometries, the actuation and flow sensing in the proposed algorithms require massive arrays of actuators and sensors embedded in a control design. These massive arrays limit practical applications of the proposed algorithms. The number of actuators needed for a control design has been explored for a channel flow in [8] and for a pipe in [9]. In both cases, the analysis is based on a global stabilization approach using Lyapunov functions. The results show that the spatial changes in the velocities are smooth and small for a homogeneous flow regime, which suggests that in practice a small number of actuators can achieve the same goal regarding mixing criteria given in [1]. The analysis also indicates appropriate values of proportional feedback coefficients which enhance the stability of the homogeneous flow, whereas destabilization of the homogeneous flow yields an excellent mixing of fluid elements [1]. This is a rather promising result for practical applications.

Another well-studied microscopic model of fluid flow is an open-channel fluid flow model, i.e., the Saint-Venant equations, which is a hyperbolic PDE model that describes the fluid flow between two gates in the channel. The control strategy for the open-channel model is mainly based on manipulating fluid properties at the boundaries, i.e., gates. This type of spatially distributed control design is known as boundary control design. Here, we will mention only the most relevant control designs: LQ control methods [10], robust H_∞ control design techniques [65], and boundary PI regulation [100] based on a linearized model. One interesting contribution regarding the open-channel fluid flow model is that the input/output structure has to be defined at the boundaries while the flow between the boundaries can be considered as a space delay function [34]. This suggests that the same boundary control strategy can be applied to other hyperbolic-like PDE models. Another interesting contribution of the open-channel flow is presented in [12]. The boundary control design based on a strict Lyapunov function in [12] gives a direct correlation between exponential stability of a steady-state situation and dissipation of the energy throughout the boundaries. The strict Lyapunov function suggests the control of energy dissipation throughout the boundaries under the assumption that the system of hyperbolic PDEs is diagonalizable with the Riemann invariants [12]. In this case, the time derivative of the Lyapunov function can be made strictly negative by an appropriate selection of the boundary control laws. This result leads to a well-posed boundary control strategy for hyperbolic PDEs and can be applied in a wide range of other models that describe transport of fluid. In Chapter 4, the method of characteristics presented in [34] will be illustrated using the two-phase flow model.

To the best of our knowledge, there has not been any structurally developed work published that deals with the control strategy for two-phase flow using microscopic models that describe the hydrodynamics of two-phase flow. We will make an initial contribution in this thesis which contains the work that has been published in [39, 40].

1.5 Problem Formulation

1.5.1 Overview

As we previously discussed, there is a growing need for the model-based control designs of chemical processes to move from modeling on the reactor scale towards modeling on the microscopic scale. This is because the models that govern spatial variation of the properties under consideration give a more detailed description of the chemical process. However, due to the complexity of microscopic models, it is obvious that the control-oriented microscopic models have to present a trade-off between accuracy and model complexity. The microscopic model does not pretend to have the accuracy of complex solvers (e.g., FLUENT, ANSYS, and FEMtools). Instead, the control-oriented model has to represent the main control input influences on fluid flow behavior and to provide a sensing strategy for real-time control. The current challenge in the chemical industry is to develop a structural analysis of microscopic models and possible input/output strategies in order to operate chemical processes more efficiently and control the processes in a real-time manner. However, due to the complex nature of currently used microscopic models and CFD algorithms, the fluid flow is very often beyond the reach of control analysis. Most of the multiphase CFD work uses trial-and-error manipulation of the boundary conditions to influence the fluid flow inside the given boundaries, or uses different model reduction techniques to obtain lower-order models. For future developments, the focus of fluid flow control design should lie not only on the manipulation of the boundary conditions, it should also focus on developing control-oriented models rather than on the available CFD models. Developing an efficient modeling and control tool for fluid flow systems described by PDEs will lead to a good decision-making strategy for influencing the fluid flow on the microscopic scale, which will eventually lead to more efficient production with minimal operational costs per unit volume.

1.5.2 Research Objective

Our main objective is to offer the control community a unified set of rules and conditions for microscopic modeling of fluid systems in chemical reactors, which can be used to design spatially distributed controllers. Even though in this thesis we have restricted ourselves essentially to simple single-phase and two-phase flow without the reaction between fluid components, the modeling concept for the control design is essentially the same.

The main research objective of this thesis is:

> ***Develop a control-oriented microscopic two-phase flow model with a causal input/output structure that is well-suited for spatially distributed control designs.***

As previously discussed, there are many open problems concerning the model-based control approach to fluid systems (e.g., the complexity of CFD models, computational load, and input/output strictures). Therefore, the topic of flow control can be studied along three main research directions (**RD**).

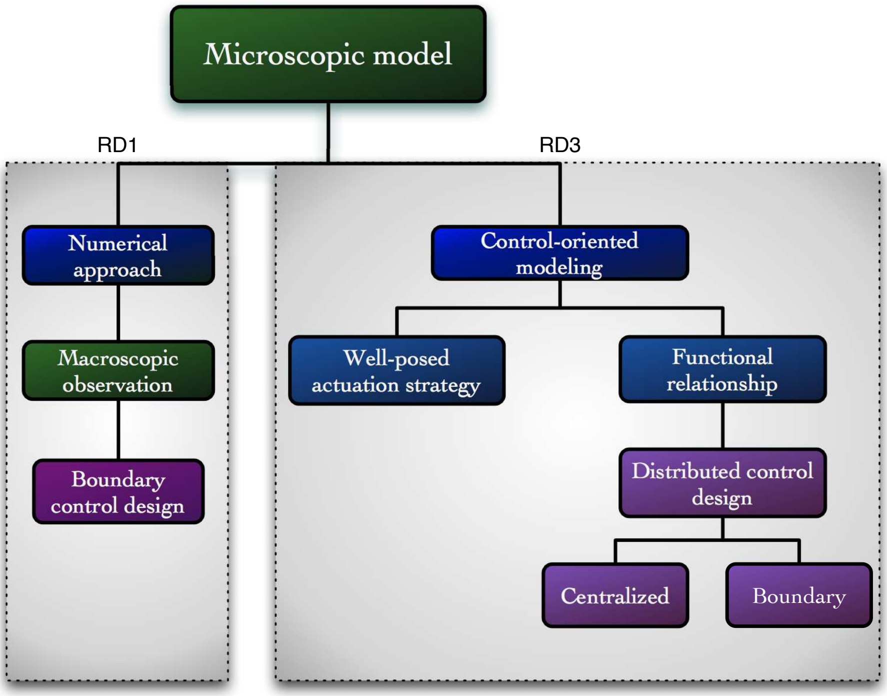

Figure 1.3: Scheme of the contributions of this thesis.

RD1 Numerical approximation of microscopic models

In general, microscopic models are usually approximated by a large number of differential equations using specific discretization methods, where the number of discretization points determines the order of a model. The numerical approximation requires information on a full flow field and is computationally expensive, involving iterative direct numerical simulations (DNS). The DNS allow us to quantify the best possible system performance for given boundary conditions and geometry [15, 53].

- This research direction investigates microscopic modeling tools of fluid properties that are commonly used in chemical reactor engineering using a numerical approach to the microscopic model. This approach is based on a fine spatial discretization of the microscopic model, which results in a large number of flow variables (i.e., microstates).
- For the purposes of flow control, the flow variables may be considered to be aggregated. It is interesting to investigate the level of observation required for control designs (see Chapter 3). In this thesis, we will present a next step in this research direction which moves towards the determination of implementable boundary control strategy to stabilize the fluid flow. The results obtained using this method have been published in [38].

RD2 Model reduction of CFD models

The main motivation behind the model reduction techniques is to reduce the computation time of the corresponding simulations. In system theory, model reduction is associated with model-order reduction, which implies reduction of the number of differential equations obtained from discretized PDE models. The model reduction method that has been widely studied in literature is the Proper Orthogonal Decomposition (POD), which is also known as the Karhunen-Loève decomposition [57, 66]. This method is based on simulation data usually obtained by CFD software packages, and is well suited for reduction of large-scale complex systems [5]. Although there are numerous other factors that can contribute to decreasing the computation time of the CFD models that are studied in along the line of **RD1** illustrated in Figure 1.3, this research direction falls outside the scope of this thesis. For the model reduction techniques, we refer to [5, 69, 89, 96].

RD3 Defining functional relationships between inputs and outputs

The control-oriented microscopic model is intended to study the relationship between model properties and the choice of inputs and outputs on the microscopic scale. This is an important research direction for control-oriented microscopic modeling. It involves not only the physics and first principle models, but also suggests possible control designs and functional relationships between inputs and outputs [11, 55]. Defining functional relationships between inputs and outputs for two-phase flow in the time-space domain is the main focus of this thesis. In the remainder of this section we will provide the solution steps which are the key concepts in the control-oriented microscopic modeling of two-phase flow (see Figure 1.3).

- The main modeling goal is to derive a model that comprises dominant system dynamics, whereas the less dominant dynamics are left for further redesign. The control-oriented microscopic model will be introduced in Chapter 4.
- Important aspects of input/output structures involve causality, boundary conditions, spatial discretization schemes, and numerical methods. These aspects are crucial in setting the theoretical framework for systems described by the microscopic model. This will be discussed in Chapter 5.
- Following a wide range of possible input/output structures, different spatially distributed control designs can be suggested. Recommendations for the practical use of different spatially distributed control designs are given in Chapter 6.

1.5.3 Thesis Outline

This thesis discusses current issues in the modeling of fluid flow for the chemical industry and provides new solutions to current fluid flow problems. The remainder of the thesis is organized as follows:

- Chapter 2 provides basic microscopic conservation laws that govern the behavior of fluid flow treated in the chemical industry. Various aspects of modeling issues are discussed, which need to be understood in order to develop a control-oriented microscopic model of chemical processes that can be used for spatially distributed control design.

- Chapter 3 focuses on several important aspects of Chapter 4 concerning modeling on the microscopic scale, which fall along research direction **RD1**. First, the multiscale modeling aspect of single-phase flow is analyzed in simple geometry, i.e., the lid-driven cavity case. Second, a boundary controller is designed using macroscopic output regulation of the single-phase flow as a test example of the flow control.

- In Chapter 4, we translate the findings of multiscale modeling from Chapter 3 into requirements for the control-oriented modeling of two-phase flow (i.e., **RD3** in Figure 1.3). We propose a new modeling approach to two-phase flow as a starting point to develop a control-oriented two-phase flow model. The well-posedness of the derived control-oriented two-phase flow model is studied using the method of characteristics and eigenvalue analysis, which leads to the determination of a well-posed boundary actuation strategy.

- Chapter 5 is focused on the causality of different input/output structures for the derived control-oriented two-phase flow model. The effect of inputs on the chosen outputs is studied in the Laplace-space domain, which gives the functional relationships between the chosen inputs and the outputs. The Laplace representation of the model leads to a condition for a causal input/output structure. This chapter contains the main contribution of the thesis, namely a strategy to develop a causal input/output structure.

- Chapter 6 proposes different spatially distributed control designs which are easy to implement. We place great emphasis on centralized and boundary controllers, whereas other possible spatially distributed control designs are suggested for future work. The centralized and boundary control designs are tested on the numerical example developed in Chapter 4.
- Finally, the conclusions and recommendations are set out in Chapter 7.

Chapter 2

Modeling on the Microscopic Scale

In this chapter, we will discuss issues related to the microscopic modeling of chemical processes and fluid flow that are important to understand in order to develop a well-posed microscopic model. The issues such as conservation laws, the well-posedness of the problem formulation, general solution, and initial-boundary value problem will be presented. At the end of this chapter, we will summarize the modeling issue and control aspects that have to be considered while developing a control-oriented microscopic model.

2.1 Introduction

As we discussed in Chapter 1, in the microscopic modeling of chemical processes we often encounter a large number of problems related to PDEs. In this chapter, we will investigate the conservation laws that are commonly used to derive microscopic models. This chapter is structured in such a way that readers who are unfamiliar with the complexity of microscopic models used in the chemical industry should be able to gradually build a knowledge of PDE models and related issues. After a brief overview of the idea of balance equations given in Section 2.2, we will discuss issues related to PDEs in Section 2.3, which we will expand in Sections 2.4 and 2.5 addressing the control perspectives of microscopic modeling. After this chapter, one should get a clear idea of what we mean by control-oriented microscopic models and well-posed input/output structures for spatially distributed systems. Since this thesis is concerned with the control of fluid flow systems, we are more interested in how to develop a structural control approach to models that describe fluid flow than the accuracy of the proposed numerical methods for solving microscopic models. To represent the input/output structure, we will use a single-phase flow model as a numerical example in Chapter 3, and a two-phase flow model in Chapter 4.

2.2 Microscopic Models

2.2.1 Microscopic Conservation Laws

In chemical engineering, the flow of material through a system can be quantitatively described by conservation laws. Depending on the quantity Φ under consideration within the system, the conservation laws are classified as:

- mass (m),
- momentum (ρv), and
- energy (E),

with ρ being the density and v being the fluid velocity. In most of the fluid examples, we usually observe more than one quantity which forms a mathematical description of system dynamics, i.e., a model. In such cases, Φ is simply a vector consisting of the following elements: m, ρv, and E of the fluid system. In general, conservation of a system means that there is no net gain or loss of those three quantities, only their redistribution (e.g., conversion of energy).

The conservation laws (e.g., mass and energy) are commonly understood through the transformation of one property to another. The dissipation of mass and energy from a system can simply be seen as an exchange of the system's properties with its surroundings through the system boundaries. According to the discussion presented in Section 1.2.2, the conservation laws can be derived on different scales as illustrated in Figure 1.1, which result in the formulation of different models (see Section 1.2.3). On a reactor scale, as illustrated in Figure 2.1(a), the general balance equation can be written as

$$\frac{\mathrm{d}\Phi}{\mathrm{d}t} = \Phi_{\mathrm{in}} - \Phi_{\mathrm{out}} + S(\Phi), \tag{2.1}$$

where the subscript *in* stands for the inlet flow and *out* for the outlet flow across the system boundaries. The source term $S(\Phi)$ is used to represent all sorts of terms that describe different phenomena (e.g., reaction rate, shear stress, dissipation of energy), which will be discussed later in this section for each property separately. In general, models obtained by (2.1) assume the spatially uniform distribution of Φ and are known as ODE models.

On the microscopic scale, the material properties are observed on a much smaller scale compared to the reactor scale (see Figure 2.1(b)). The rate of change involves all cross-sections along the space (e.g., x_1 and x_2). The overall rate of change can be expressed as an integral on the quantity and flow field in the volume $V = L_x \times L_y \times L_z$ as

$$\frac{\partial}{\partial t}\int_V \Phi dV + \int_A \Phi v \cdot n dA = \int_V S dV, \tag{2.2}$$

where $\Phi v \cdot n dA$ symbolizes the amount of flow of quantity Φ through the area $n dA$ per unit time which is integrated over the whole observed volume V. Equation (2.2)

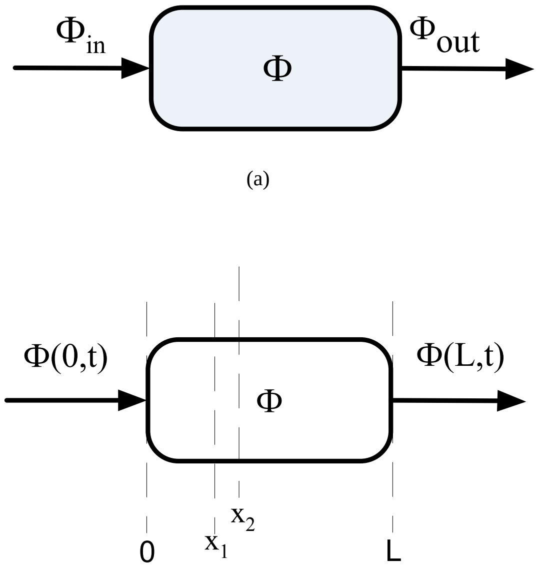

(a)

(b)

Figure 2.1: The flow of Φ on (a) a reactor scale that results in ODE models (i.e., lumped parameter models) and (b) a microscopic scale that results in PDE models (i.e., distributed parameter models).

gives the most general form of microscopic model of a chemical process written as the following PDE

$$\frac{\partial\Phi}{\partial t}+v_x\frac{\partial\Phi}{\partial x}+v_y\frac{\partial\Phi}{\partial y}+v_z\frac{\partial\Phi}{\partial z}=S\left(\Phi,\frac{\partial\Phi}{\partial x},\frac{\partial\Phi}{\partial y},\frac{\partial\Phi}{\partial z},\frac{\partial^2\Phi}{\partial x^2},\frac{\partial^2\Phi}{\partial y^2},\frac{\partial^2\Phi}{\partial z^2}\right), \tag{2.3}$$

where x, y, and z refer to the spatial direction and the right-hand side of (2.3) is the source term which describes the spatial redistribution of Φ. Depending on the quantity under consideration and the microscopic law, the source term can be a function of Φ only, or a function of the spatial gradients of Φ, which depends on the quantity under consideration. This will be discussed in the following sections for each quantity Φ separately.

2.2.2 Models Based on Mass Balance Equations

In chemical engineering, the rate of change in mass is usually observed over a volume element, and therefore instead of m, it is commonly expressed as changes of density ρ in $[kg/m^3]$ or concentration C in $[mol/m^3]$, which is discussed in [17, 30, 64].

The microscopic mass balance equation written as the change of concentration in a 3D system can be given as

$$\frac{\partial C}{\partial t}+v_x\frac{\partial C}{\partial x}+v_y\frac{\partial C}{\partial y}+v_z\frac{\partial C}{\partial z}=D_e\left(\frac{\partial^2 C}{\partial x^2}+\frac{\partial^2 C}{\partial y^2}+\frac{\partial^2 C}{\partial z^2}\right)+r(C) \tag{2.4}$$

where D_e is the effective diffusion coefficient and $r(C)$ is the reaction rate. The right-hand side of (2.4) represents the source term. The formulation of the microscopic mass conservation law given as (2.4) assumes that the velocities v_x, v_y, and v_z are constant values. Usually, the velocity field $v=\begin{bmatrix} v_x & v_y & v_z \end{bmatrix}^T$ is an average estimate of the real velocity field inside a reactor.

The fluid flow and transport mechanism of the flow in (2.4) are described through convective transport $\left(v_x\frac{\partial C}{\partial x}+v_y\frac{\partial C}{\partial y}+v_z\frac{\partial C}{\partial z}\right)$ and diffusion $D_e\left(\frac{\partial^2 C}{\partial x^2}+\frac{\partial^2 C}{\partial y^2}+\frac{\partial^2 C}{\partial z^2}\right)$. For this reason, (2.4) is also known as the *convection-diffusion equation with reaction*[1]. The ratio between the convection and diffusion transportation in the dominant flow direction is commonly defined by the Peclet number [2] as

$$Pe=\frac{\text{convection}}{\text{diffusion}}=\frac{v_x L_x}{D_e},$$

for x-direction as the dominant flow direction. The Peclet number varies between infinity ($D_e=0$) for plug-flow, and zero ($v_x=v_y=v_z=0$) for well-mixed flow. In this way, the back flow is modeled via the diffusion coefficient which is determined experimentally. Due to the assumption that the velocity field is constant over the entire space, the relationship between the diffusion coefficient and the velocity field can be estimated using different empirical correlations for different flow regimes. Over the last few decades a wide range of empirical correlations between v_x and D_e for two-phase flow have been published [102]. These empirical correlations allow us to examine the diffusion coefficient for different practical setups and operational regimes regardless of the properties described by fluid dynamics. Clearly, these correlations give acceptable results for a specific type of flow regime and specific reactor used in the experiments for the estimation of the diffusion coefficient. For a more accurate representation of the fluid flow, the velocity field v has to be derived on the basis of the classical hydrodynamic laws.

2.2.3 Models Based on Momentum Balance Equations

The momentum balance equation is the basic equation of fluid dynamics. It balances the motion of fluid systems (i.e., phases) with respect to time and space. The equations arise from applying Newton's second law to fluid elements [4]. This law is applied under the assumption that the fluid stress is a sum of a diffusing viscous term and a pressure term of each phase in a multiphase fluid flow system [41, 47, 51]. Before we introduce the balance equations for multiphase flow, we will present the momentum

---

[1] In multiphase flow literature, this model is also known as the 1D axial dispersion model.

[2] Alternatively, the term Bodenstein number has been used (see [35, 64]).

balance equations for single-phase flow which is the basis for determining a multiphase fluid flow model.

Single-Phase Flow

The quantities under consideration for momentum balance are the velocity and pressure fields. These two quantities fully determine the direction of the fluid flow inside the observed space. A 3D representation of the basic momentum balance equation for a single-phase flow, often referred to as the Navier-Stokes equations, can be written for each velocity component of v separately as

$$\frac{\partial \rho v_x}{\partial t} + v_x \frac{\partial \rho v_x}{\partial x} + v_y \frac{\partial \rho v_x}{\partial y} + v_z \frac{\partial \rho v_x}{\partial y} = \mu\left(\frac{\partial^2 v_x}{\partial x^2} + \frac{\partial^2 v_x}{\partial y^2} + \frac{\partial^2 v_x}{\partial z^2}\right) - \frac{\partial p}{\partial x} + \rho g_x, \tag{2.5}$$

$$\frac{\partial \rho v_y}{\partial t} + v_x \frac{\partial \rho v_y}{\partial x} + v_y \frac{\partial \rho v_y}{\partial y} + v_z \frac{\partial \rho v_y}{\partial y} = \mu\left(\frac{\partial^2 v_y}{\partial x^2} + \frac{\partial^2 v_y}{\partial y^2} + \frac{\partial^2 v_y}{\partial z^2}\right) - \frac{\partial p}{\partial y} + \rho g_y, \tag{2.6}$$

$$\frac{\partial \rho v_z}{\partial t} + v_x \frac{\partial \rho v_z}{\partial x} + v_y \frac{\partial \rho v_z}{\partial y} + v_z \frac{\partial \rho v_z}{\partial y} = \mu\left(\frac{\partial^2 v_z}{\partial x^2} + \frac{\partial^2 v_z}{\partial y^2} + \frac{\partial^2 v_z}{\partial z^2}\right) - \frac{\partial p}{\partial z} + \rho g_z. \tag{2.7}$$

where p is the pressure, μ is the fluid viscosity, and g is the gravitational acceleration. Note that the gravitational force can act only in one spatial direction (or under angle θ of the given direction). Without loss of generality, we add gravitational force in all three spatial directions, although the gravity is mainly oriented vertically, i.e., $g_x = g\cos(\theta)$, $g_y = 0$, $g_z = 0$. The Navier-Stokes equations govern the motion of nearly all fluid flow systems with some additional terms required for turbulent regimes.

The complexity of the Navier-Stokes solution lies in the implicitly modeled pressure effect and the nonlinearity of the convective term. Therefore, in order to solve the pressure field, an additional equation is required [1, 4, 99]. The additional equation to close the solution set can be obtained from the concept of mass conservation. The mass balance equation is written as a density variation for compressible flow as

$$\frac{\partial \rho}{\partial t} + \frac{\partial \rho v_x}{\partial x} + \frac{\partial \rho v_y}{\partial y} + \frac{\partial \rho v_z}{\partial z} = 0, \tag{2.8}$$

and for incompressible flow as

$$\frac{\partial v_x}{\partial x} + \frac{\partial v_y}{\partial y} + \frac{\partial v_z}{\partial z} = 0. \tag{2.9}$$

Now we have two sets of PDEs which form a set of solutions for v and p in the given domain. The first PDE is obtained from the mass balance equation (2.9), whereas the second set of PDEs is obtained from the momentum balance (2.5)-(2.7). The hydrodynamic models, i.e., CFD models, always involve those two sets of PDEs known as the Navier-Stokes equations. Although the Navier-Stokes equations seem to be the same type of PDE as the convection-diffusion equation (2.4), the implicitly modeled pressure creates an additional complexity which requires different numerical algorithms in order to obtain a solution. This will be further discussed in Chapter 3.

Multiphase Flow

In the classical fluid flow approach, the model equations for multiphase flows are mainly derived by "averaging" equations describing the microscopic flow problem, i.e., the Navier-Stokes equations [41, 47]. This approach results in a set of equations having a similar structure as the Navier-Stokes equations from which they originate.

The mass and momentum balance equations of a multiphase flow are based on the following relations

$$V = \sum_{\ell=1}^{m} V_\ell, \quad \alpha_\ell = \frac{V_\ell}{\sum_{\ell=1}^{m} V_\ell}, \quad \sum_{\ell=1}^{m} \alpha_\ell = 1,$$

where m represents the number of phases, V_ℓ is the volume occupied by phase ℓ, V is the total observed volume, and α_ℓ is the volume fraction of phase ℓ. This means that an observation space is partly occupied by one phase and partly by the others [41]. Based on the aforesaid assumptions, the multiphase balance equations can be written in a compact form as

$$\begin{aligned} \frac{\partial \alpha_\ell \rho_\ell v_\ell}{\partial t} + \nabla \cdot (\alpha_\ell \rho_\ell v_\ell v_\ell) = -\alpha_\ell \nabla p_\ell - (p_{\ell,i} - p_\ell)\nabla \alpha_\ell + \\ + \nabla \cdot (\alpha_\ell \tau_\ell) + \alpha_\ell \rho_\ell g + \nabla \cdot (\alpha_\ell \rho_\ell v_\ell' v_\ell') + (-1)^\ell F, \end{aligned} \tag{2.10}$$

for the momentum balance, and

$$\frac{\partial \alpha_\ell \rho_\ell}{\partial t} + \nabla \cdot (\alpha_\ell \rho_\ell v_\ell) = 0, \tag{2.11}$$

for the mass balance, where $\nabla = \begin{bmatrix} \frac{\partial}{\partial x} & \frac{\partial}{\partial y} & \frac{\partial}{\partial z} \end{bmatrix}^T$ is an operator in the Cartesian coordinate system, ρ_ℓ denotes the density of phase ℓ, v_ℓ is the velocity of phase ℓ, p_ℓ is the pressure, $p_{\ell,i}$ is the interfacial pressure, F is the two-way coupling term, and τ_ℓ is the viscous stress that can be expressed by

$$\tau_\ell = \mu_\ell(\nabla v_\ell + \nabla v_\ell^T) - \frac{2}{3}\mu_\ell \nabla \cdot v_\ell I. \tag{2.12}$$

The term $\alpha_\ell \rho_\ell v_\ell' v_\ell'$ in (2.10) is added in order to model the turbulent stress tensor, which has to be closed by an appropriate multiphase turbulence model [3]. The model is formulated in terms of sets of equations for each phase ℓ [23]. The term F explicitly contains the interaction phenomena between the phases described by different coupling terms. The common expression for the interfacial coupling is

$$F = F_d + F_a + F_l + F_h, \tag{2.13}$$

where F_d is the viscous drag force, F_a is the added mass force due to inertia of the carrier fluid (e.g., liquid phase in bubble columns), F_l is the transversal force due to the

---

[3] The prime sign is commonly used in physics to describe the flow fluctuation and should not be mistaken with time derivatives.

rotational strain, and F_h is the collective memory effects [47, 62]. Many of the presently used advanced models consider different interfacial coupling terms that have complete physical background and closure equations [51]. Most of the closure relations are of an empirical nature, or include some heuristic elements which cannot be completely deduced from the first principles (see Chapter 4) and, therefore, bring an additional complexity into the multiphase flow modeling.

In the multiphase flow models, the effect of pressure is modeled via total pressure and interfacial pressure. This is a unique aspect of multiphase flow. Multiphase flow literature mentions several interfacial pressure correction models [41, 47, 51]. The models that involve interfacial pressure are also known as the *two-pressure models* [80]. The single pressure model is known to be ill-posed due to the assumption that there is only one pressure present [93]. This will be further discussed in Chapter 4 using the method of characteristics to prove this statement. Although it seems reasonable to require that the pressure correction term vanishes once the phase becomes identical, there are still models treated in multiphase flow literature that do not meet this requirement [47].

2.2.4 Models Based on Energy Balance Equations

The formulation of the energy balance equation for a chemical system is much more involved compared to the classical mechanical systems. The energy balance equations for chemical systems involve thermal, chemical, and mechanical energy [6]. In general, energy balance equations are defined by first thermodynamics laws (i.e., balanced thermal and kinetic energy) and second thermodynamics laws (i.e., balanced entropy) [84]. There have been suggestions of additional energy conservation laws [17, 58].

In many cases, thermal energy is the most dominant one, whereas kinetic and chemical energy can be neglected for control design. Here, we give a model which is based on thermal energy (i.e., heat flow) as a form of energy transfer as an illustration of the microscopic energy conservation law

$$\frac{\partial T}{\partial t}+v_x\frac{\partial T}{\partial x}+v_y\frac{\partial T}{\partial y}+v_z\frac{\partial T}{\partial z}=D_T\left(\frac{\partial^2 T}{\partial x^2}+\frac{\partial^2 T}{\partial y^2}+\frac{\partial^2 T}{\partial z^2}\right), \tag{2.14}$$

where $D_T=\dfrac{\kappa}{\rho c_p}$ is the thermal diffusion coefficient with κ being thermal conductivity and c_p being specific heat capacity. Equation (2.14) with $v_x=v_y=v_z=0$ (i.e., without convective transport) is one of the most studied energy balance equations in the literature [17, 25, 64], and it is also known as the *heat equation*.

2.3 Solutions to PDE Models

2.3.1 General PDEs

As presented in the previous section, the conservation laws for systems in motion are mathematically described by a set of PDEs involving a function of several variables and their partial derivatives. According to their specific solution, PDEs belong to fundamentally different types of equations known as the *parabolic*, *hyperbolic,* and *elliptic* PDEs [67] that explain diffusion processes, wave propagation, and static potential phenomena, respectively (see Table 2.1). This classification is based on the discriminant of the highest derivative coefficients in a PDE. To illustrate the concept, we give a simple second-order PDE example

$$a\frac{\partial^2 u}{\partial x^2} + b\frac{\partial^2 u}{\partial x \partial t} + c\frac{\partial^2 u}{\partial t^2} = d. \tag{2.15}$$

where the discriminant can be computed from the given coefficients as $D = b^2 - 4ac$. If $D = 0$, (2.15) is said to be parabolic with real repeated eigenvalues. If $D > 0$ then (2.15) is said to be hyperbolic, which means that the eigenvalues of the hyperbolic equations are real and distinct. The behavior of systems described by hyperbolic equations can be characterized as a wave propagation, where the speed of the wave is specified by the eigenvalue. This implies that the quantity under consideration propagates along a characteristic direction with finite speed. This will be illustrated on a control-oriented two-phase flow model in Chapter 4. The solution to the hyperbolic PDEs may also contain shock-like discontinuities because of the non-dissipative nature of these equations [29, 92]. On the other hand, if $D < 0$, (2.15) is said to be elliptic with complex eigenvalues, where the observed quantity propagates in all spatial directions simultaneously with a closed solution domain [77]. The elliptic equations are characteristic of constraint equations in spatial domain and static potential problems in material science or mechanics (see Table 2.1).

The given classification of the PDE models is based on the coefficients a, b, and c, and it can also be used to analyze PDEs where the coefficients are state independent with nonlinearity on the right-hand side of (2.15), i.e, $d(u)$. For the nonlinear and quasi-linear class of PDEs with the state dependent coefficients $a(u)$, $b(u)$, and $c(u)$, such as the convective terms in the Navier-Stokes equations, the classification is more involved.

Table 2.1: Different types of PDEs with related examples of physical phenomena, and initial-boundary conditions required to obtain a solution.

Example of PDE	Type	Physical phenomena	Conditions
$\frac{\partial \Phi}{\partial t} = \alpha \frac{\partial^2 \Phi}{\partial x^2}$	parabolic	diffusion	initial and boundary
$\frac{\partial^2 \Phi}{\partial t^2} = \alpha \frac{\partial^2 \Phi}{\partial x^2}$	hyperbolic	wave	initial and boundary
$\frac{\partial^2 \Phi}{\partial x^2} + \frac{\partial^2 \Phi}{\partial y^2} = 0$	elliptic	static potential	boundary

The general categorization of solution of PDE models is based on whether the equations are solved using analytical or numerical techniques:

1. *Numerical:* The numerical techniques mainly involves different discretization techniques in order to obtain a solution. To solve the governing PDEs numerically, one has to discretize the equations with respect to space and time [42].

   In spatial discretization, the following methods are commonly used:

   - Finite difference. At each intersection of the lines of the finite difference techniques, the governing equation is replaced by a finite difference approximation.
   - Finite volume. The finite volume method discretizes a volume into a number of cells of an arbitrary shape. Subsequently, the governing equations on these discrete control volumes are solved satisfying conditions for conservation of mass, momentum, and energy between the finite volumes.
   - Finite element. Here, the governing PDEs are solved using a modified mesh domain. The unknown values of the flow property inside an element are approximated by shape functions.

   Besides the spatial discretization, time discretization can also use a wide range of numerical methods to ensure solutions. Examples include the explicit and implicit Euler method, the midpoint rule, and the trapezoid rule [98]. In explicit time integration schemes, the time step for a solver during integration is limited. The limit is determined by the Courant number which defines a ratio between the time and space step $c = v\triangle t/\triangle x$, where $\triangle x$ is the characteristic length of the cell defined between two spatial discretization points, and $\triangle t$ is the time step. To ensure correct computations in explicit methods, the Courant number c may not exceed 1. This condition is often referred to as the Courant-Friedrichs-Lewy (CFL) condition, and it represents a necessary condition for convergence while solving certain PDEs numerically.

2. *Analytical:* In some cases, the governing equations can be solved analytically following a number of simplification steps. In microscopic modeling, it is common to simplify details of the models, such as geometry of the system and detailed phenomena, in order to obtain mathematical models which govern dominant dynamics. The simplified models are usually described by example equations which are given in Table 2.1.

3. *Combination of numerical and analytical:* This method can be applied to models that are solved analytically in some directions and numerically in others.

The PDE models which do not have analytical solutions require the use of extensive numerical computations in order to obtain a solution. As discussed in Chapter 1, the computation in the time-space domain can be rather involved, especially in the case of the Navier-Stokes equations where the pressure term is modeled implicitly. The Navier-Stokes equation and the equations that describe the multiphase flow can be solved only numerically using different numerical schemes and approximations, such as optimization methods for solving pressure field, iterative algorithms for solving constraint equations, linearization or assumptions of weak nonlinearity, small fluctuations, and multigrid algorithms [98]. The high-resolution numerical methods play an important role in obtaining solutions for most of the models used to describe fluid flow. Although it might seem trivial, we would like to stress here the importance of numerical methods to solve the Navier-Stokes equations. For the CFD models based on the microscopic momentum equations, this includes the methods based on the Approximate Riemann Solver, Flux Vector Splitting techniques, and the Split Coefficient Matrix Method [46]. The former two belong to Godinov-type methods based on a finite volume discretization assuming a constant or linear parameter distribution between two discretization points in space. The split coefficient method represents a finite difference technique, where the new time steps of all spatial points are calculated by solving the linearized characteristic form of the governing equations along the characteristic curves. The concept of “up-winding” which combines the preservation of wave propagation along the characteristic directions with the conservation of mass, momentum, and energy for the solution of the convective term is common to all these methods [29, 92]. A large number of publications can be found on this topic.

2.3.2 Initial and Boundary Conditions

One of the fundamental problems of PDEs is an initial-boundary value problem. It is possible to find a general solution of a single PDE for given initial-boundary conditions only in special cases. In most physical problems described by a set of PDEs, the main concern is finding initial and boundary conditions that lead to a unique solution. The initial-boundary conditions are often suggested in problem formulation, such as open boundary conditions for the flow in pipes, no-slip boundary conditions on the side walls of cavities. To solve the 1D flow equation as given in (2.3), we have to define a well-posed initial condition $\Phi(0,x)$ and/or a well-posed boundary condition at $x = 0$, i.e., $\Phi(t,0)$ and at $x = L$, i.e., $\Phi(t,L)$. Table 2.1 presents an analogy between PDEs, physics, and initial-boundary conditions. It is obvious from the table that in addition to having to define the boundary conditions which are functions of time $\Phi(t,0)$ and $\Phi(t,L)$, we also have to define the initial condition $\Phi(0,x)$ for parabolic and hyperbolic PDEs. The boundary conditions of hyperbolic-like PDE problems will be discussed in Chapter 4 and further justified in Chapter 5 for a microscopic two-phase flow model.

2.3.3 Well-Posed Problems

Besides the initial-boundary value problem, the well-posedness of a PDE problem is another very important attribute to modeling any physical problem. The physical intuition suggests that we have a well-posed problem if a PDE gives a unique solution for time-dependent problems. Parabolic and hyperbolic PDE systems are known to be well-posed problems with a stable and unique solution, whereas elliptic PDE systems are ill-posed with a solution that propagates in all directions which is characteristic of time independent problems, i.e., static potential problems. In general, an ill-posed problem usually means that the PDE has to be solved backwards, which is not physically possible in the time domain, and therefore it represents ill-posed problems with respect to time.

Here, we also use the term *well-posed* initial-boundary condition to refer to a PDE problem defined by associated initial-boundary conditions which ensure a solution. A problem involving a PDE defined in a given domain that is not well-posed is often said to be an improperly posed or ill-posed initial-boundary condition. There are several fundamental issues associated with the initial-boundary value problem [50, 67]:

- *existence of solutions*,
- *uniqueness*,
- *continuous dependence*, and
- *stability*.

The existence of a solution depends on the nature of the PDE and the initial-boundary conditions. Posing too many initial and boundary conditions or conditions that cannot be satisfied might lead to the absence of a solution, i.e., ill-posed boundary conditions. On the other hand, posing fewer conditions can lead to the existence of more than one solution, i.e., the nonuniqueness of the solution. Another requirement of a physical problem is stability. The stability of a solution of a PDE subject to the initial and boundary conditions is a natural expectation when modeling physical problems. The stability means that if the initial condition is changed by only a small amount, the system should behave in almost the same way. Mathematically, this is translated into the statement that the solution should depend continuously on the initial value. A similar statement can be made for boundary value problems. To be more precise regarding these fundamental issues, we need to satisfy several inequalities with regard to a stable solution, e.g., Cauchy theory and Poincare inequality [77]. There are numerous articles published dealing with the existence and uniqueness of a single solution of a PDE, its structure, and asymptotic behavior, which are properties that depend on the class of PDEs used to model the microscopic behavior of a system [19, 67]. These are just a few of the issues in the study of PDEs. The primary issues, however, from the point of view of applied analysis of PDEs, are the methods of solution available to obtain either an exact or approximate solution, and the way the solution can be influenced. These issues will be addressed in subsequent chapters using microscopic momentum balance equations for the single-phase and two-phase fluid flow systems. These control-oriented microscopic models will eventually lead to spatially distributed control strategies that can be used to influence the fluid flow systems.

2.4 Input/Output Structures

For the model-based control strategy, a substantial difference in actuation strategies exists between problems described by a set of ODEs and by a set of PDEs. Figure 2.2 illustrates the different input/output structures for ODE and PDE systems. As shown

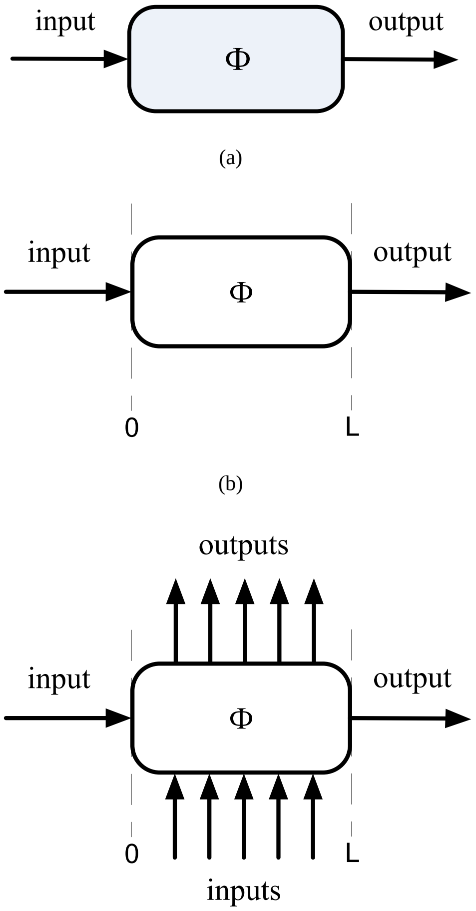

(a)

(b)

(c)

Figure 2.2: Input/output structures on (a) the reactor scale, (b) the microscopic scale with a boundary actuation, and (c) the microscopic scale with spatially distributed actuation.

in Figure 2.2(a), for the systems described by a set of ODEs an input/output does not depend on the spatial domain. The manipulated variable Φ_{in} in Figure 2.1(a) represents the input as shown in Figure 2.2(a). In contrast to these ODE models, PDE models allow an independent actuation access at each point in the defined spatial domain as illustrated in Figures 2.2(b) and 2.2(c). Discretization of PDE models leads to a large number of ODEs that can be written in a state-space form, where the states are the properties in each grid block and the inputs are defined in each block [75, 79, 91].

In Figure 2.2(b), the choice for the input/output structure is based on the boundary conditions (see Figure 2.1(b)). The boundary condition $\Phi(t,0)$ represents the input whereas $\Phi(L,0)$ represents the output. This means that the model-based control design with the input/output structure as shown in Figure 2.1(b) for systems described by microscopic conservation laws is based on manipulating the boundary conditions. As illustrated in Figure 2.2(c), the inputs may also be placed at each grid block which creates a distributed network of inputs on the spatial domain [78]. In this way, we can manipulate the spatial distribution of flow property $\Phi(t,x)$. A similar difference exists in sensing of ODE systems and spatially distributed sensing of PDE systems. Different actuation and sensing strategies for the microscopic two-phase flow model will be discussed in Chapter 6 for the bubble column reactor which is described in Chapter 1.

2.5 Control-Oriented Modeling

In order to obtain a microscopic model for practical use, we need a set of PDEs that describe dominant dynamics of a process based on a set of simplifying assumptions. These simplifying assumptions may involve, for example, modeling in 1D only, dominance of convection transport over the diffusion, empirical correlations between some properties, such as diffusion and velocity. However, the simplification of the microscopic model should not be an end in itself. Instead, it should contain a clear strategy of how to use the models in improving process performances in the chemical industry. For example, for the purpose of control design, the microscopic modeling of fluid systems should ideally aim to develop a simplified model with a well-developed input/output structure, whereas all the detailed phenomena should be left for redesign. The input/output structure can be further used to design a controller which can influence the system behavior and improve the overall process performance. In this thesis, we refer to models obtained in this way with a clear control strategy in mind for a particular example, as a *control-oriented microscopic model*, or a *control-oriented model*, for short. The benefits of the control-oriented modeling can be significant since it provides additional understanding as to how to influence the fluid flow inside a reactor, instead of only getting an accurate microscopic model. While developing a control-oriented model, we have to observe the following aspects of a given problem:

- *Model complexity.* The model complexity is to be kept as low as possible. Focusing on the dominant dynamics and desired process performance is the first step in deriving a simple control-oriented model which provides the insights needed for control design. It is favorable to keep the computational load as small as possible. We will study this aspect in Chapter 3 for the single-phase flow and in Chapter 4 for the two-phase flow. For the two-phase flow, this complexity is mainly caused by the interactive terms between the phases and turbulence effect.

- *Multiscale modeling*. As discussed in Section 1.2.2, the aggregation of fluid elements can appear on different scales. However, the microscopic scale and reactor scale are two extremes of continuous and discrete space observation. The molecules are usually aggregated in large formations (e.g., a large number of bubbles in bubble columns). This scale is defined by design, and we can refer to it as a macroscopic scale or compartmental scale. On this scale some of the detailed phenomena can be neglected or taken as an average quantity. In Chapter 3, we will use single-phase flow to illustrate the concept of multiscale modeling and possibilities for control designs.

- *Accuracy.* Although accuracy is an obvious requirement, it is still important to state our exact objectives in this matter. We have to accurately predict the behavior of the fluid system, the well-posedness of the model, and initial-boundary conditions; all other details can be left for redesign. For example, for control purposes, lower accuracy is acceptable since it can be seen as a model uncertainty. This implies that the major performance determining fluid flow should be predicted accurately with well-posed initial-boundary conditions, whereas numerical issues can be considered later in control design. Furthermore, it is preferable to have functional relationships between inputs and outputs that do not rely on discretization methods. These functional relationships can be used to simplify distributed control designs (see Chapter 6).

- *Multiphase modeling.* The multiphase modeling can be described by the governing equations of fluid mechanics where several fluid and solid components move at the same time. One of the simplest examples of the multiphase modeling involves only two phases (e.g., gas and liquid, gas and solid). The multiphase modeling studies the flow of the fluid and solid components either separately or as mixture flow. The main contribution of this theses is in the two-phase fluid flow modeling, which is the simplest case of the multiphase modeling. Chapters 4, 5, and 6 describe the use of a control-oriented two-phase flow model for control design.

- *Geometry.* The geometry of a chemical reactor, where the motion of fluid takes place, often presents an additional problem in the microscopic modeling of chemical processes. It is very difficult to generate a refined mesh without using a CFD package, which was discussed in Section 1.2.3. Given the model requirements and the complexity of geometry involved, the model geometry can be simplified retaining the main modeling framework. In Chapter 3, we study single-phase flow in 2D on a rectangular domain, whereas in Chapter 4 we derive a 1D two-phase flow model.

The main challenge for new developments in the field of microscopic modeling is to study the above given aspects for a chemical process and to develop a control-oriented strategy that can influence the microscopic system behavior. The following chapters will give a detailed description of the control-oriented flow models and spatially distributed control designs for single-phase and two-phase flow systems.

2.6 Discussion

This chapter outlined the available modeling tools for derivation of models on a microscopic scale and introduced notation that will be used in further chapters. In this chapter, we first presented the basic microscopic conservation laws used in modeling chemical processes, after which we discussed the main issues related to problems described by PDEs. As has been shown, the more details we try to model using the microscopic conservation laws, the more the models become computationally involved. The microscopic model becomes computationally unfeasible and requires advanced CFD packages to fully simulate the motion of fluid systems. Especially in case of microscopic momentum equations, the two-phase flow model may lead to a CFD model that has a limited use for on-line application due to the long computation time and model complexity. In order to obtain a solution to a CFD model, a large number of numerical techniques and discretization schemes have to be employed. The CFD models are tailored in order to mathematically describe different interactive terms, e.g., added mass and virtual mass, in order to establish the cause of problems that arise from coalescing and bubble size distribution. The CFD complex models often aim to describe most of the phenomena that exist on the microscopic scale rather than being constructed to assess an overall performance. As a result, many complex CFD models have been beyond the reach of engineers in the chemical industry and have limited practical use for control designs.

In the following chapters of this thesis, we will derive control-oriented strategies for different fluid flow systems that are of high relevance for the chemical industry. In Chapter 3, we will use a single-phase flow in a closed geometry to illustrate the concept of multiscale modeling which is beneficial for boundary feedback control design. Complementary to the single-phase flow, in Chapter 4, we will propose a control-oriented two-phase flow model with a well-posed actuation strategy that can eventually be used for a wide range of different control designs that will be presented in Chapter 6.

Chapter 3

Control of Macroscopic Properties of Single-Phase Flow

After a brief overview of the microscopic modeling presented in Chapter 2, in this chapter we will set out a numerical approach to the microscopic models that describe single-phase flow in simple geometry. In this chapter, different modeling scales will be used to design a boundary controller for the single-phase flow. The main focus of this chapter is on a boundary control design based on macroscopic observation, i.e., a higher level of aggregation of controlled variable in the single-phase flow systems. In order to demonstrate the applicability of the macroscopic quantitative varables for the boundary control design, the results are illustrated using a lid-driven cavity case, which has a broad range of industrial applications.

3.1 Introduction

As we discussed in Chapter 1, the microscopic models that describe the motion of fluid are usually very complex, and they can only be solved numerically using various types of discretization methods (see Section 2.3.1). In general, the numerical approach to a microscopic fluid flow model uses fine grids to obtain microstates which can be manipulated and measured. However, the flow properties modeled on the microscopic scale give a very detailed picture of the fluid flow that, in many cases, is not directly measurable. Thus, concentrating large efforts on fine discretization schemes does not necessarily provide a solution to the control related problems.

In Chapter 2, we discussed the most important aspects of control-oriented modeling and their contribution to control designs. In this chapter, we will investigate two aspects: the input/output structures and the multiscale modeling aspects of fluid flow using the numerical approach described as **RD1** in Chapter 1. The analysis presented in this chapter will eventually lead to a computationally efficient system with a well-posed input/output structure (see Section 3.4.1) that can be easily used for boundary control design (see Section 3.4.2). The concept of macroscopic control design will be introduced in Section 3.2, after which every derivation step of the macroscopic properties needed for the design will follow. As an illustration example of the single-phase flow in simple geometry, in Section 3.3.1 we will introduce a lid-driven cavity case [24]. The lid-driven cavity flow study is useful for improving many practical application prototypes such as drying chambers, rotating reactors, short-dwell coaters, and melt-spinning processes in forming continuous metal ribbons. As a result of the proposed macroscopic output regulation of the fluid flow, we will establish a macroscopic boundary control technique for regulation of the fluid flow system. Results contained in this chapter have been published in [38].

This chapter is structured in such a way that readers who are unfamiliar with the complexity of the single-phase flow (i.e., the Navier-Stokes equations) and the numerical approach to the problem of single-phase flow should be able to gradually build an understanding of the complexity behind the fluid flow models.

3.2 Macroscopic Control Design

The main objective of the multiscale modeling is to explore the possibility of using macroscopic quantities for regulating different fluid flow regimes. Despite the modeling scale, the fluid flow regimes can be categorized as *homogeneous* (i.e., laminar) and *heterogeneous* (i.e., turbulent). The homogeneous regimes are characterized by uniform, laminar flow with hardly any mixing, i.e., plug flow. On the other hand, the heterogeneous regimes have good mixing properties due to the turbulent effect and circulation of fluid systems with a tendency to create a chaotic behavior of fluid elements. The main control goal in fluid flow regulation control is to bring a fluid system to a desirable fluid behavior and stabilizing the flow around the desired fluid flow. According to the desired flow regime, different control objectives can be defined [1, 44]:

- stabilization of laminar flow,
- delaying or advancing transition from laminar to turbulent flow,
- suppressing or enhancing turbulence, and
- preventing or enhancing separation of phases in multiphase flow systems.

Benefits that can be gained from these control objectives include drag reduction, lift enhancement, mixing enhancement, and flow-induced noise suppression. These aspects are very important for increasing process productivity in the chemical industry.

As we discussed in Section 1.4, many different control methods have been presented in the control literature dealing with the flow control problem, starting from control designs that stabilize laminar regimes [27, 28, 52, 53, 55, 56], towards more complex optimal control designs that control turbulence [15]. The most common flow control approach is based on the linearized Navier-Stokes equation where the laminar flow inside a pipe or a channel can be stabilized using different distributed control methods [8]. A shortcoming of this method is that the proposed distributed input/output

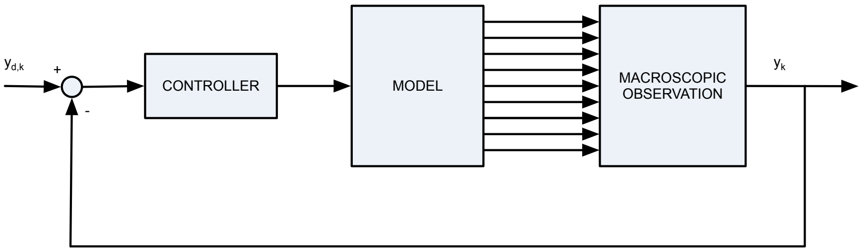

Figure 3.1: Block diagram of a control design based on a macroscopic observation of fluid flow obtained from the microscopic model.

structure might not be implementable in practice since it suggests a massive array of actuators and sensors.

Recent results published in [2, 9] have shown that the spatial changes of the fluid flow are smooth and small, which suggests that in practice a smaller number of actuators can achieve the same goal. This analysis also indicates appropriate values of control coefficients which enhance the $\mathcal{L}_2$ stability of the flow, pointing out that destabilization of the flow yields an excellent result for fluid mixing [1]. The results published in [2, 9] also raise an additional question about the number of sensors needed for the control design and accuracy of the measurement with respect to space. However, not much attention has been given to the control requirements for the flow sensors and size of images that describe velocity fields which should be embedded in the distributed control design.

The work presented in this chapter deals with multiscale modeling and sensing of fluid properties on a higher level of aggregation. In this chapter, a macroscopic output regulation as illustrated in Figure 3.1 is introduced. The macroscopic control design can be seen almost as a filtering of the microstates obtained by fine discretization of the flow properties. In essence, this means that the individual fluid elements (i.e., microstates) are observed by an aggregation of fluid elements (i.e., macrostates) as controlled variables. This will be discussed in detail in Section 3.4.2. In the next section, we will present a single-phase flow in a lid-driven cavity case to illustrate the microstates and macrostates of the single-phase flow properties.

3.3 Single-Phase Flow in Simple Geometry

3.3.1 Lid-Driven Cavity Case

The lid-driven cavity case is a simple case of fluid flow in a square domain that has three stationary sides and one moving side [85]. The geometry of the lid-driven cavity case is illustrated in Figure 3.2. In order to model the velocity fields of the lid-driven cavity

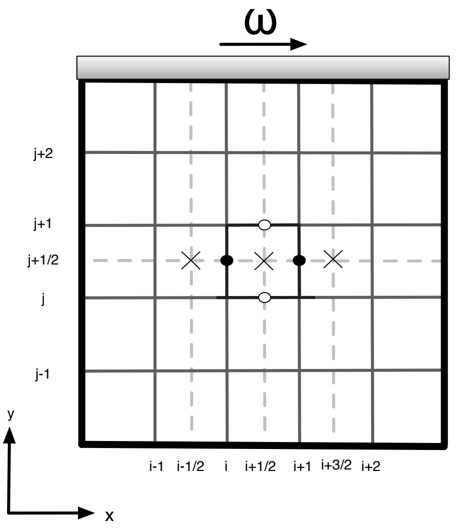

Figure 3.2: Geometry of the lid-driven cavity case with a staggered grid. The spatial discretization is performed on the staggered grid with the pressure $p_{i+\frac{1}{2},j+\frac{1}{2}}$ *in the cell midpoint (×), the velocities* $u_{i,j+\frac{1}{2}}$ *and* $u_{i+1,j+\frac{1}{2}}$ *placed on the vertical cell interfaces (○), and the velocities* $v_{i+\frac{1}{2},j}$ *and* $v_{i+\frac{1}{2},j+1}$ *placed on the horizontal cell interfaces (●).*

case, we consider a dimensionless form[1] of the single-phase flow model derived from the Navier-Stokes equations (see Section 2.2.3) and defined on a rectangular domain $\Omega = [0,1] \times [0,1]$

$$\frac{\partial u}{\partial x} + \frac{\partial v}{\partial y} = 0, \tag{3.1}$$

$$\frac{\partial u}{\partial t} = -u\frac{\partial u}{\partial x} - v\frac{\partial u}{\partial y} + \frac{1}{Re}\left(\frac{\partial^2 u}{\partial x^2} + \frac{\partial^2 u}{\partial y^2}\right) - \frac{\partial p}{\partial x}, \tag{3.2}$$

$$\frac{\partial v}{\partial t} = -u\frac{\partial v}{\partial x} - v\frac{\partial v}{\partial y} + \frac{1}{Re}\left(\frac{\partial^2 v}{\partial x^2} + \frac{\partial^2 v}{\partial y^2}\right) - \frac{\partial p}{\partial y}, \tag{3.3}$$

where the dimensionless variables u and v are the velocity components in the x and y-direction, p is the pressure, and Re is the Reynolds number. The gravitational effect and viscous dissipation outside this rectangular domain are neglected. Note also that the dimensionless form of the Navier-Stokes equation has only one parameter which is the Reynolds number.

The initial conditions for the velocity field are $u(t,x,y) = 0$ and $v(t,x,y) = 0$ for $t = 0$. According to the geometry shown in Figure 3.2, the boundary conditions are the

---

[1] Dimensionless in the sense that the variables are scaled without physical units.

velocity component in the x-direction on the top wall (lid), and the no-slip conditions for the velocity components at the bottom wall and the two sides walls, i.e.,

$$\begin{aligned} u(t,x,1) &= \omega, & u(t,x,0) &= 0, \\ v(t,x,1) &= 0, & v(t,x,0) &= 0, \\ u(t,0,y) &= 0, & u(t,1,y) &= 0, \\ v(t,0,y) &= 0, & v(t,1,y) &= 0, \end{aligned}$$

where ω is the velocity of the lid.

The momentum equations (3.2) and (3.3) describe the time evolution of the velocity vector field (u,v) under inertial and viscous forces, whereas the pressure p is an implicit variable that satisfies the incompressibility condition (3.1). This was discussed in Section 2.2.3. As we already discussed in Section 2.2.3, the incompressibility condition is not a time evolution equation but an algebraic condition instead. Therefore, the pressure term can be solved only by projecting the momentum equations onto the divergence-free velocity field [90]. The CFD has developed a large number of numerical schemes and softaware packages that are able to solve these equations (see Section 1.2.3). Here, the numerical schemes based on DNS is used to spatially discretize (3.1)-(3.3). In the remaining of this section, we will discuss the spatial discretization of the given equations and numerical issues related to the chosen discretization method.

Spatial Discretization

In order to illustrate the concept of projection of the momentum equations onto the divergence-free velocity field, we will first start with the discretization method as shown in Figure 3.2. The figure emphasizes three types of markers that will be used to explain the discretization scheme. Any point inside the cell marked as ”$\times$” is an interior point, while the points marked as ”$\circ$” and ”$\bullet$” are the grid points. The body forces are positioned in the midpoints, while the surface forces are positioned at the cell interfaces. The terms which contain the spatial derivatives are approximated using the interior grid points to obtain the numerical solution of (3.1)-(3.3) as follows:

- *Approximation of the first derivatives:*
  The first derivatives (i.e., convective terms and pressure gradient) in a grid point can be approximated by a centered stencil as

  $$\frac{\partial u}{\partial x} \approx \frac{u_{i+1,j} - u_{i-1,j}}{(x_{i+1} - x_{i-1})} = (u_x)_{i-1,j}.$$

  This approximation of the first derivative for the nonlinear term $u\dfrac{\partial u}{\partial x}$ might cause different numerical instabilities [4, 98]. This is the reason why we introduce the staggered grids as illustrated in Figure 3.2 to overcome the problem of numerical instabilities. The principle behind the staggered grid is to create the data in the midpoints by averaging the flow properties at grid points $i+1$ and $i-1$ for the x-direction, and $j+1$ and $j-1$ for the y-direction. This means that we approximate the value in the middle using data between the points $u_{i+1,j}$ and $u_{i,j}$, which is, in essence, a stable centered approximation of u_x

$$(u_x)_{i+\frac{1}{2},j} \approx \frac{u_{i+1,j} - u_{i,j}}{x_{i+1} - x_i}.$$

In the staggered griding of (3.2)-(3.3), this position is the position of pressure $p_{i,j}$. The pressure term in the staggered griding will be discussed later in this section.

- *Approximation of the second derivatives*
  The second derivatives (i.e., viscous terms) are approximated by a finite difference method for the grid point at the centered stencil. Approximation of the second derivatives at any interior point (i,j) is done by

$$\frac{\partial^2 u}{\partial x^2} + \frac{\partial^2 u}{\partial y^2} \approx \frac{u_{i-1,j} - 2u_{i,j} + u_{i+1,j}}{(x_{i+1} - x_{i-1})^2} + \frac{u_{i,j-1} - 2u_{i,j} + u_{i,j+1}}{(y_{j+1} - y_{j-1})^2} = (u_{xx})_{i,j} + (u_{yy})_{i,j},$$

  where one or two of the neighboring points (e.g., $i+1$ and $i-1$ in the x-direction) might be the boundary points.

- *Approximation of the nonlinear terms:*
  The approximation of nonlinear terms on the staggered grid cannot be applied directly. It requires an additional numerical approximation. For instance, the product uv is not directly defined at the position (i,j), since the velocities $u_{i,j}$ and $v_{i,j}$ are defined at different positions. In order to update the velocity $u_{i,j}$, we need the following terms $(u_x)^2_{i,j}$ and $(u_{i,j}v_{i,j})_y$.[2] If the flow in each time step is shown to be slow, we can use the same centered staggered derivatives at the position $(i+\frac{1}{2}, j\frac{1}{2})$. This requires the use of different positions in space in order to define the velocity terms, e.g., $u^2_{i,j}$ has to be defined in the cell centers and $u_{i,j}v_{i,j}$ has to be defined in the cell corners

$$u^2_{i+\frac{1}{2},j} = \left(\frac{u_{i,j} + u_{i+1,j}}{2}\right)^2,$$
$$u_{i,j+\frac{1}{2}} = \left(\frac{u_{i,j} + u_{i,j+1}}{2}\right),$$
$$v_{i+\frac{1}{2},j} = \left(\frac{v_{i,j} + v_{i+1,j}}{2}\right).$$

  The above centered differencing is appropriate if the quantities are not transported too far in each time step [4, 98]. This was discussed in Section 2.3, and for the numerical algorithm we refer to Appendix A.

---

[2] Note that $u\frac{\partial u}{\partial x} = \frac{1}{2}\frac{\partial u^2}{\partial x}$.

Table 3.1: Boundary conditions.

Type of boundary conditions	Mathematical expressions
Neumann	$\frac{\partial u}{\partial x} = 0$
Dirichlet	$u = 0$

- *Boundary conditions:*
  In the lid-driven cavity case, we use the Dirichlet boundary conditions for $u_{i,j}$ and $v_{i,j}$, and the Neumann boundary conditions for $p_{i,j}$ (see Table 3.1). This is because the points ”$\circ$” and ”$\bullet$” lie on the boundaries, whereas the point “$\times$” has the boundary between two neighboring “$\times$” points. The value at the points that lie on the boundary is directly prescribed by the given boundary conditions. For example the velocity u_N at the left boundary, often referred as the right-wall boundary, has to satisfy the Dirichlet boundary condition given in Table 3.1. The same analogy holds for the velocity $u_{i,j}$ at the bottom boundary, as well as for the velocity $v_{i,j}$ at the right-wall and left-wall boundary. For the pressure, the derivatives $\frac{\partial p}{\partial x}$ and $\frac{\partial p}{\partial y}$ at the boundaries are defined using two points which are placed in the middle. For instance, the Neumann boundary conditions at the top wall give a solution of pressure at the top boundary. This means that the following condition holds for this point

  $$\frac{p_{i,j+1} - p_{i,j}}{y_{j+1} - y_j} = 0.$$

  If the boundary conditions are not properly defined, or the domain is not properly discretized, then the solution to the PDE problem does not exist. This was also discussed in Section 2.3 in terms of ill-posed boundary conditions.

For the full numerical algorithm that is used to compute the velocity and pressure fields in the time-space domain, we refer to Appendix A.

3.3.2 Summary of the Numerical Approach to the Single-Phase Flow Model

In this section, we briefly summarize the outcome of the numerical approach to the single-phase flow model in the lid-driven cavity case. First, we used the spatial discretization method based on the staggered gridding to obtain a solution to the dimensionless Navier-Stoke equations written as (3.1)-(3.3). Once the staggered grid has been defined, we proposed a finite difference approach to determine approximate expressions for the necessary derivatives of the flow variables in the x and y-direction. Such a numerical approach to the Navier-Stokes equations resulted in a large number of microstates ($u_{i,j}$,$v_{i,j}$, and $p_{i,j}$) in the given spatial domain Ω. Numerical results of this approach will be given in Section 3.5.

The next step in the macroscopic control design is to define an appropriate input/output structure that can capture the system behavior, i.e., flow regime, which can be used to influence the flow regime. The flow regime, whether laminar or turbulent, is a very important feature of any fluid system. The level of mixedness, which determines the energy required to maintain the desired flow, depends on the level of observation of the aggregated fluid elements and on the available measuring techniques. For the lid-driven cavity case, the boundary conditions at the top wall (i.e., the lid velocity) are considered as the inputs, whereas the outputs will be determine as the flow properties on the macroscopic scale. As discussed in Section 3.2, the main control objective is to design a controller using a higher level of aggregation of the fluid elements. In the following sections, we will discuss how to use the microstates obtained in Section 3.3.1 to quantify the macroscopic properties of the fluid flow that can be used for the control design illustrated in Figure 3.1.

3.4 Boundary Control Design

3.4.1 Interconnected Form of a Large-Scale System

In order to develop a control strategy for the previously discussed microscopic fluid flow, an appropriate control framework is required. First, for the proposed model-based control design shown in Figure 3.1, we start with analyzing the microscopic variables. An interconnection between the microscopic variables for the cavity case previously discussed is illustrated in Figure 3.3. After the spatial discretization of (3.1)-(3.3), the Navier-Stokes equations are approximated with a large number of finite-dimensional differential equations with algebraic constraints for the pressure correction (see Appendix A). The discretized model is described by the following state vector

$$z_{i,j} = \begin{bmatrix} u_{i,j} \\ v_{i,j} \end{bmatrix}, \tag{3.4}$$

where $i = 1,2,...,n$, $j = 1,2,...,n$ are the spatial indexes and $z_{i,j}$ is the state vector in $\mathbb{R}^{2n^2}$ as illustrated in Figure 3.3. The number of grid points in the x and y-direction is chosen to be equal. This discretization method results in a large number of nonlinear equations with algebraic constraints that can be represented in a general form as interconnection of subsystems $\sum_{i,j}$ with the following model equations

$$\begin{aligned} \dot{z}_{i,j} = {} & f_{i,j}(z_{i,j}, z_{i-1,j}, z_{i+1,j}, z_{i,j-1}, z_{i,j+1}, p_{i,j}) \\ & + g_{i,j}(z_{i,j}, z_{i-1,j}, z_{i+1,j}, z_{i,j-1}, z_{i,j+1}, p_{i,j}) w_{i,j} \end{aligned} \tag{3.5}$$

$$0 = \phi_{i,j}(z_{i,j}, z_{i-1,j}, z_{i+1,j}, z_{i,j-1}, z_{i,j+1}, p_{i,j}), \tag{3.6}$$

where $w_{i,j}$ is the input, $f_{i,j}$ and $g_{i,j}$ are the nonlinear functions. The indexes $i-1$, $i+1$, $j-1$, and $j+1$ are complementary indexes which illustrate the way subsystems are coupled [13, 76, 78]. The functions $f_{i,j}$ and $\phi_{i,j}$ are smooth functions that approximate the time evolution of the velocity field (3.1)-(3.3) and the constraint equation (3.1), respectively. The velocity vector of the top wall (see Figure 3.3) is considered to be the boundary input $w_{i,1}$

$$w_{i,1} = \begin{bmatrix} u_{i,1} \\ v_{i,1} \end{bmatrix} = \begin{bmatrix} \omega \\ 0 \end{bmatrix}.$$

Equations (3.5)-(3.6) represent a system consisting of n^2 subsystems $\Sigma_{i,j}$ that are interconnected by the complementary state vectors, $z_{i-1,j}$, $z_{i+1,j}$, $z_{i,j-1}$, and $z_{i,j+1}$, to the systems $\Sigma_{i-1,j}$, $\Sigma_{i+1,j}$, $\Sigma_{i,j-1}$, and $\Sigma_{i,j+1}$, respectively. In this way, the stability of the interconnected system is reduced to the stability problem of the subsystems. On the other hand, the controllability and observability of the interconnected system are reduced to the influence of the complementary state vectors $z_{i-1,j}$, $z_{i+1,j}$, $z_{i,j-1}$ and $z_{i,j+1}$ on the state vector $z_{i,j}$. Since the flow regimes are characterized by *Re*, the value of *Re* determines the stability regions. The overall flow is considered to be stable for low *Re* and unstable for high *Re*. The unstable flows are characterized by the growth of small fluctuations from the steady velocity profile which can, eventually, cause instability of the velocity profile.

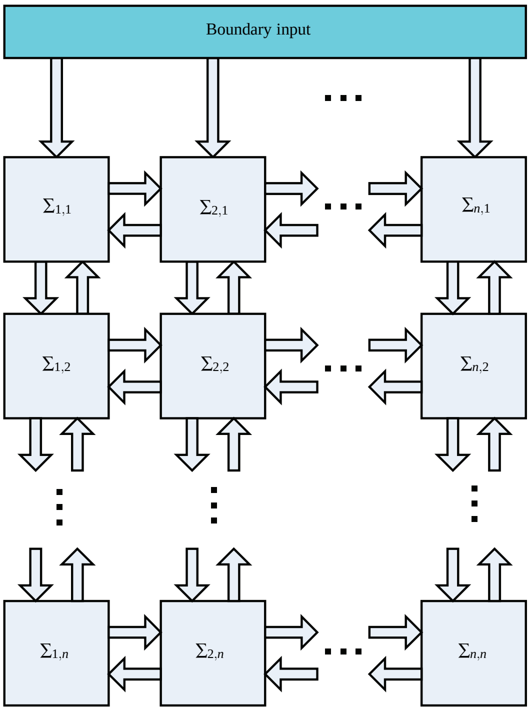

Figure 3.3: Two-dimensional interconnection of subsystems.

3.4.2 Macroscopic Output Regulation

For the large-scale system which contains many states that can be controlled and measured, the measurable variables have to be chosen in such a way that the overall system can be evaluated. This means that, instead of observing the microstates $z_{i,j}$ in the domain $\Omega_{i,j}$, we introduce macroscopic domain $\overline{\Omega}_{k,k}$ over which the controlled variables are defined, i.e.,

$$\overline{\Omega}_{k,k} = \Delta x_k \cdot \Delta y_k, \qquad k = 1,2,...,r.$$

The index k is a macroscopic observation index which specifies the macroscopic domain $\overline{\Omega}_{k,k}$. The number of grid points in the x and y-direction for the macroscopic space equals r. We should emphasize that the number of discretization points in the macroscopic space is much smaller than the microscopic one, i.e., $r \ll n$. As illustrated in Figure 3.1, the microstates obtained from the fine numerical discretization of the dimensionless Navier-Stokes equations serve as basis to derive the macroscopic controlled variables

$$y_{k,k} = \frac{1}{\overline{\Omega}_{k,k}} \sum_{i=\frac{(k-1)}{r}n+1}^{\frac{k}{r}n} \; \sum_{j=\frac{(k-1)}{r}n+1}^{\frac{k}{r}n} h_{i,j}(z_{i,j}), \tag{3.7}$$

where $y_{k,k}$ is the output in $\mathbb{R}^{r^2}$, and $h_{i,j}(z_{i,j})$ is the output function. Here, we consider an average function as mapping between the microstates derived in (3.5)-(3.6) and the macrostates as the controlled variables, although other functions can be used as well. The proposed macroscopic output regulation shown in Figure 3.1 is applicable to any system where the changes in microstates of each subsystem are small and bounded in time. This will be discussed in detail in Section 3.5.

Following the control design presented in Section 3.2, our control objective is to find a boundary controller $w_{i,1}$ such that the system output converges to a desired point with an arbitrary fast exponential decay. In general, a stable system with a constant input reaches a steady-state if the output of the system approaches a constant value as time increases [48]. However, if the states $z_{i,j}(t)$ approach constant values when t goes to infinity, then $z^*_{i,j}(\infty)$ is the steady-state response of the system for the given input, which can be considered as the desired output trajectory on the microscopic scale. According to the macroscopic scale, the desired macroscopic trajectory $y^d_{k,k}$ can be obtained using the following expression

$$y^d_{k,k} = \frac{1}{\overline{\Omega}_{k,k}} \sum_{i=\frac{(k-1)}{r}n+1}^{\frac{k}{r}n} \; \sum_{j=\frac{(k-1)}{r}n+1}^{\frac{k}{r}n} h_{i,j}(z^*_{i,j}(\infty)) = const. \tag{3.8}$$

where $z^*_{i,j}(\infty)$ is considered as the microstate at $t = \infty$. For the stable system, $z^*_{i,j}(\infty) =$ const. For example, suppose that the system governed by (3.5)-(3.6) is actuated with a specific constant input $w^*_{i,1}$. In that case, the system will have a certain response to the input that can be considered as an open-loop response.

The next step in the control design is to find a controller that maintains the desired output $y^d_{k,k}$ produced by the model under the effect of $w^*_{i,1}$. Note that the boundary input

$w_{i,1}$ can have only one value ω since the lid can have only one velocity component in the x-direction (see Figure 3.2). The error between the output and the desired set can be defined by the following equation

$$e_{k,k} = y_{k,k} - y^{d}_{k,k}. \tag{3.9}$$

Then, the output feedback controller that achieves the control objective can be given by a simple PI controller that has a goal to minimize the error $e_{k,k}$ for the chosen macroscopic space (k,k), i.e.,

$$w_{k,1} = K^{P}_{k,k}(y_{k,k} - y^{d}_{k,k}) + K^{I}_{k,k}\xi_{k,k}, \tag{3.10}$$

$$\dot{\xi}_{k,k} = y_{k,k} - y^{d}_{k,k}, \tag{3.11}$$

where $K^{P}_{k,k}$ and $K^{I}_{k,k}$ are the control parameters that can be tuned. In fact, if we apply the boundary conditions $w^{*}_{i,1}$ without the controllers given in (3.10), we will still obtain the same steady-state solution, but the settling time will be longer compared to the controlled flow. This clearly implies that, for any arbitrary $w_{i,1}$ in the laminar flow regime, there is a microscopic velocity field with unique macroscopic flow properties. This will be discussed in Section 3.5 and illustrated on the lid-driven cavity case where we will present the macroscopic output regulation and tuning of the control parameters for two different *Re* in the laminar regime.

The procedure for tuning the control parameters in this macroscopic output control framework can be summarized in the following steps:

1. Select the initial condition $u(0,x,y)$ and $v(0,x,y)$ for the entire microscopic domain $\Omega = [0,1] \times [0,1]$.

2. Define well-posed boundary conditions.
   For the lid-driven cavity case, the boundary conditions are defined by the design (see Section 3.3.1).

3. Simulate the microscopic model by using an appropriate numerical algorithm (see Appendix A) and a spatial discretization method (see Section 3.3.1).

4. Analyze the steady-state solution that is obtained by applying an arbitrary boundary input $w^{*}_{i,1}$. As mentioned earlier, if the states $\lim_{t\to\infty} h_{2,2}(z_{i,j}) = \text{const}$, then $z_{i,j}(\infty)$ can be considered as a steady-state response of the system for the given initial and boundary conditions and chosen *Re* for the dimensionless Navier-Stokes equations given as (3.1)-(3.3).

5. Introduce the macroscopic domain $\overline{\Omega}_{k,k}$ that will be used to obtain the macrospic output $y_{k,k}$.
   The output function $h_{i,j}$ is chosen to be an energy function since it preserves the stability of the proposed control designs illustrated in Figure 3.1.

6. Now that we have the well-posed input/output structure with a stable steady-state solution, we can tune the control parameters $K^{P}_{k,k}$ and $K^{I}_{k,k}$ such that the system output converges to the desired point with an arbitrary fast exponential decay.

The above steps show the procedure that can be easily used to design the stabilizing boundary controller for the chosen macroscopic space in the given geometry. The same procedure can be used for other geometries with an additional modification of the output function $h_{i,j}$ and the macroscopic domain $\overline{\Omega}_{k,k}$.

3.4.3 Macroscopic Energy of Fluid Motion

In Section 3.4.1, we discussed the velocity field with components in the x and y-direction and the boundary conditions for the lid-driven cavity case, where the system is fully driven by the lid velocity $w_{i,1}$. In general, the work done by the boundary input influences the velocity and, consequently, influences the energy distribution over the domain Ω. Since the system under consideration is an incompressible fluid with no heat exchange, the rate of energy changes over the rectangular domain Ω is proportional to the kinetic energy of the subsystems. Using the expression for kinetic energy, we can obtain a kinetic energy distribution that can represent the flow patterns defined by the microscopic velocity field

$$y_{i,j} = E_{i,j} = \frac{1}{2}(u_{i,j}^2 + v_{i,j}^2). \tag{3.12}$$

In this way, we can obtain the macroscopic variables from (3.12) using the averaging procedure given in (3.7). The macroscopic variables in the domain $\overline{\Omega}_{k,k}$ equal

$$y_{k,k} = \overline{E}_{k,k} = \frac{1}{\overline{\Omega}_{k,k}} \sum_{i=\frac{(k-1)}{r}n+1}^{\frac{k}{r}n} \sum_{j=\frac{(k-1)}{r}n+1}^{\frac{k}{r}n} E_{i,j}. \tag{3.13}$$

The fact that the energy level for the given initial and boundary conditions is bounded in time can be used to assign the desired output for the control design. In the following section, we will numerically demonstrate the derived macroscopic control design based on the macroscopic output regulation of the fluid flow inside the cavity, which was illustrated in Figure 3.1.

3.5 Numerical Example

To demonstrate the numerical approach to the fluid flow systems, we used the single-phase flow for the lid-driven cavity case shown in Figure 3.2. The single-phase flow model, which is based on the Navier-Stokes equations in the given geometry, is solved in Matlab using the algorithm developed by [90]. In the given algorithm, (3.1)-(3.3) are discretized on 64 × 64 grid points in the spatial domain. To improve the numerical stability, the viscous term, which is a linear part of (3.2)-(3.3), is treated implicitly; and the convective term, which is a nonlinear part of (3.2)-(3.3), is treated explicitly (see Appendix A).

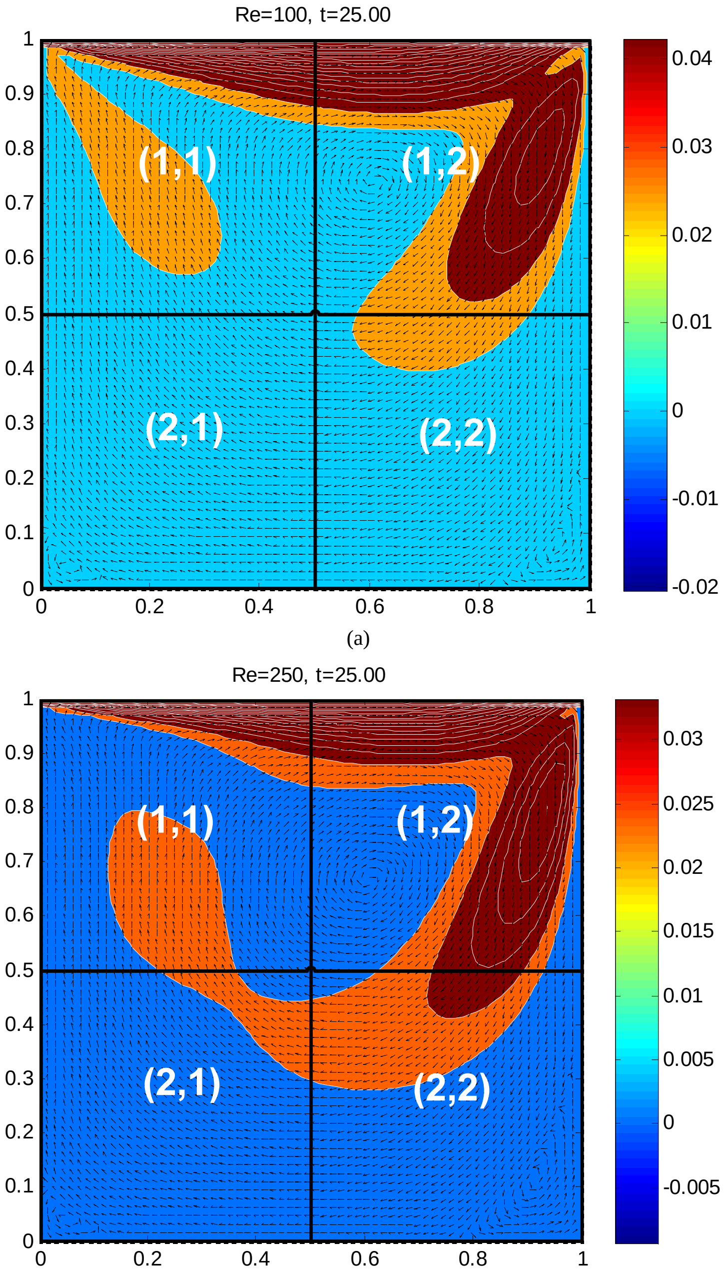

(a)

(b)

Figure 3.4: Microscopic energy distribution $E_{i,j}$ *in* $\Omega_{i,j}$ *and the macroscopic spaces* $\overline{\Omega}_{k,k}$ *where* $k = 1,2$ *at* $t = 25$ *for (a)* $Re = 100$ *and (b)* $Re = 250$.

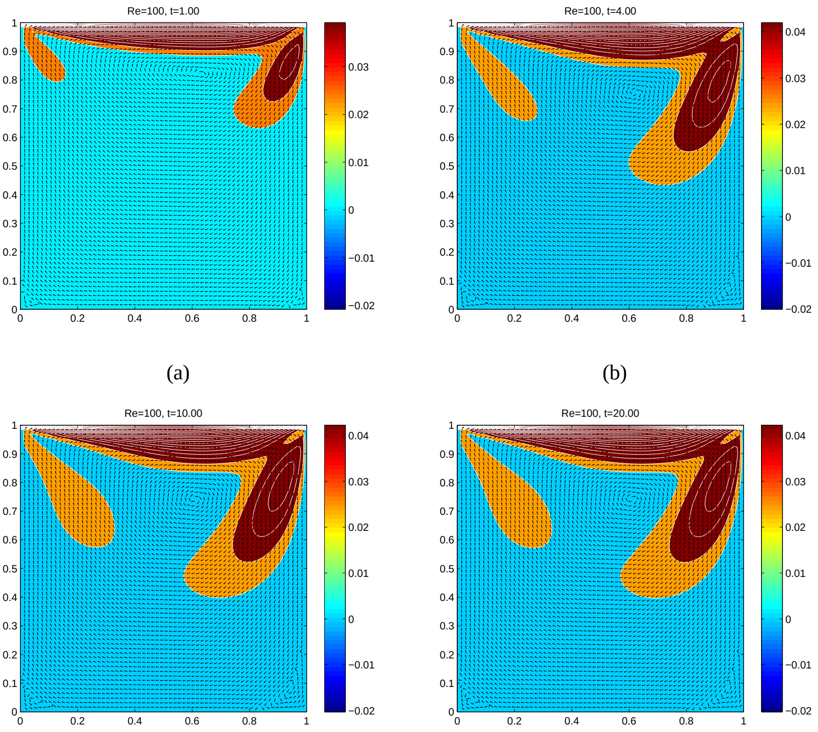

(a) (b)

(c) (d)

Figure 3.5: Time sequences of the velocity vector field and the energy field in the lid-driven cavity at $Re = 100$ *(a) t=1, (b) t=4, (c) t=10, and (d) t=20.*

Figures 3.4(a) and 3.4(b) show the steady-state simulation results of the velocity field and energy distribution for two different Reynolds numbers in the steady-state for $Re = 100$ and $Re = 250$, respectively. In Figures 3.4(a) and 3.4(b), we marked four macroscopic spaces (k,k), where $k = 1,2$, that will be used later for control design.

The time evolutions of the velocity field and energy distribution are shown in Figure 3.5 for $Re = 100$ and in Figure 3.7 for $Re = 250$. In all of these cases, the fluid flow in the cavity is strongly dominated by the recirculating vortexes in the counter-clockwise.

As shown in Figures 3.5 and 3.7, the flow is characterized by the primary dominance of a clockwise rotating subspace which are joint with two counterclockwise secondary rotating subspaces at the corners of the bottom wall. The regions with the highest energy levels are located near the top right corner at each time step and are illustrated in Figures 3.5(a), 3.5(b), 3.5(c), and 3.5(d) for $Re = 100$ at $t = 1$, $t = 4$, $t = 10$, and $t = 20$, respectively. The corresponding pressure fields are shown in Figure 3.6. In the very first stage of the lid motion, the pressure follows the formation of the rotating subspaces (see Figures 3.5(a) and 3.5(b), after which the established pressure

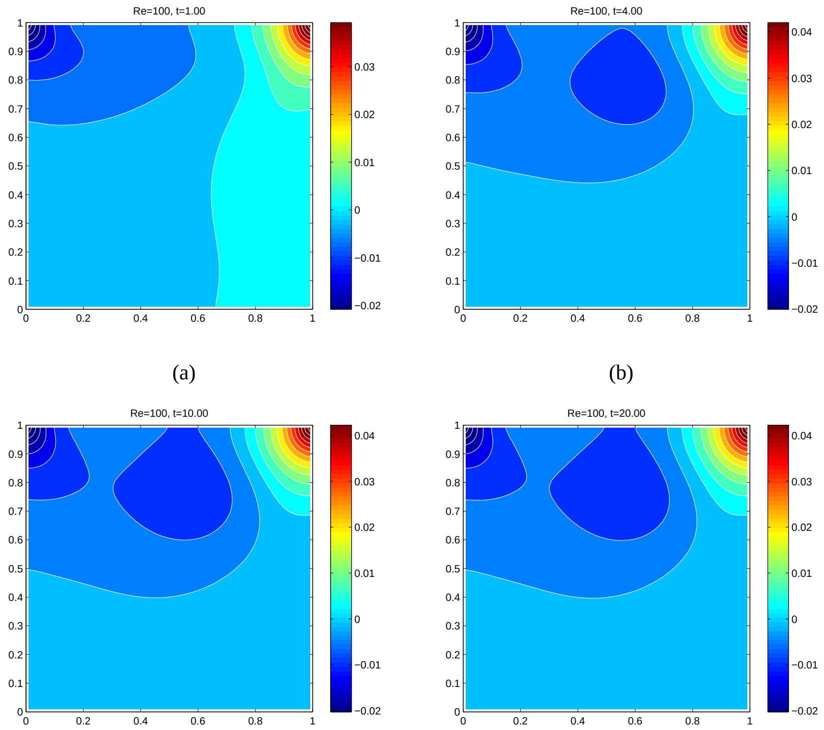

(a) (b)

(c) (d)

Figure 3.6: Pressure fields for $Re = 100$ at time (a) t=1, (b) t=4, (c) t=10, and (d) t=20.

at $t = 10$ (see Figure 3.5(c)) takes on a radial form that remains the same at $t = 20$ (see Figure 3.5(d)). These four time sequences shown for $Re = 100$ indicate formation of a small-scale circulation pressure zone located at the top right corner (see Figure 3.6), which cooresponds to the velocity filed with the highest energy level (see Figure 3.5).

The similar observation can be made for $Re = 250$. The time evolutions of the velocity field and energy distribution are given in Figure 3.7 with the corresponding pressure field shown in Figure 3.8. The energy level decreases in the same manner as shown for $Re = 100$, starting from the top wall to the bottom wall. This causes a non-uniform distribution of the energy.

Now, following the theoretical framework presented in Section 3.4.2, the macroscopic spaces $\overline{\Omega}_{k,k}$ are used to quantify the macroscopic properties as described in Section 3.4.3. First, an equilibrium-like profile is evaluated from the energy level $\overline{E}_{k,k}$ in each subspace $\overline{\Omega}_{k,k}$ over the time domain, which is defined by (3.13) and illustrated in Figures 3.9(a) and 3.9(b) for $Re = 100$ and $Re = 250$, respectively. Figures 3.4(a) and 3.4(b) show four different microscopic spaces marked as $(1,1)$, $(1,2)$, $(2,1)$, and

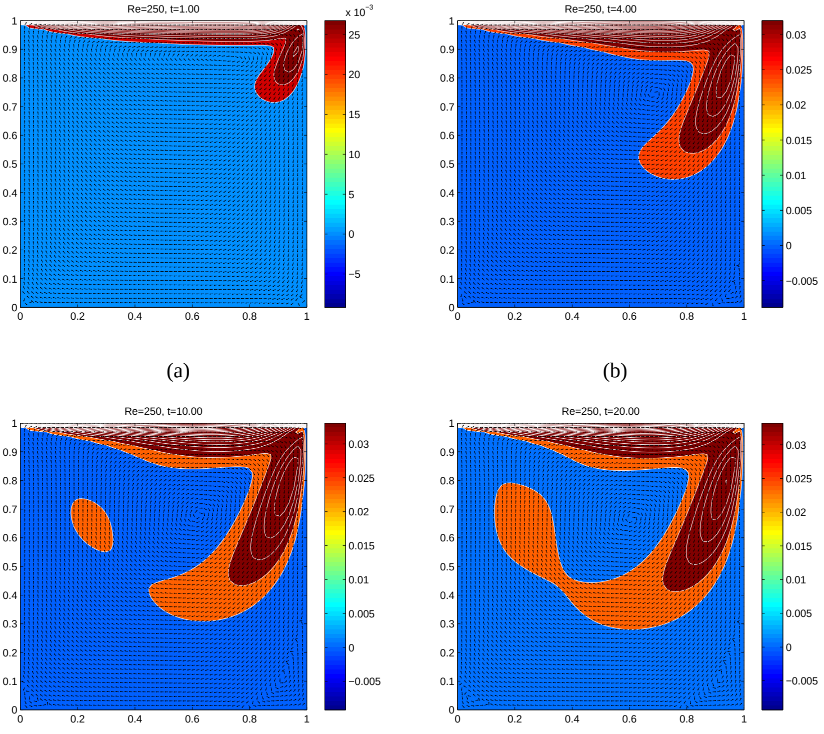

(a) (b)

(c) (d)

Figure 3.7: Time sequences of the velocity vector field and the energy field in lid-driven cavity at Re $= 100$ *(a) t=1, (b) t=4, (c) t=10, and (d) t=20.*

$(2,2)$, which give four different macroscopic functions evaluated in Figure 3.9. We choose $\overline{\Omega}_{2,2}$ as the macroscopic space to quantify the energy level $E_{2,2}$. The energy level in $\overline{\Omega}_{2,2}$ is the most sensitive energy level compared to the other energy levels.

As expected, for low *Re* the energy level of each subspace approaches constant values when time increases. Furthermore, the macroscopic energy trajectories of each subspace $\overline{\Omega}_{k,k}$ show stable responses with respect to time and the macroscopic flow behavior under influence of the boundary input. The considerable influence of the boundary input is noticed in $\overline{\Omega}_{2,1}$ and $\overline{\Omega}_{2,2}$, where the secondary vortex enlarges by increasing the boundary input. Thus, the macroscopic energy level of $\overline{\Omega}_{2,2}$, which corresponds to the constant values, is considered to be the controlled variable.

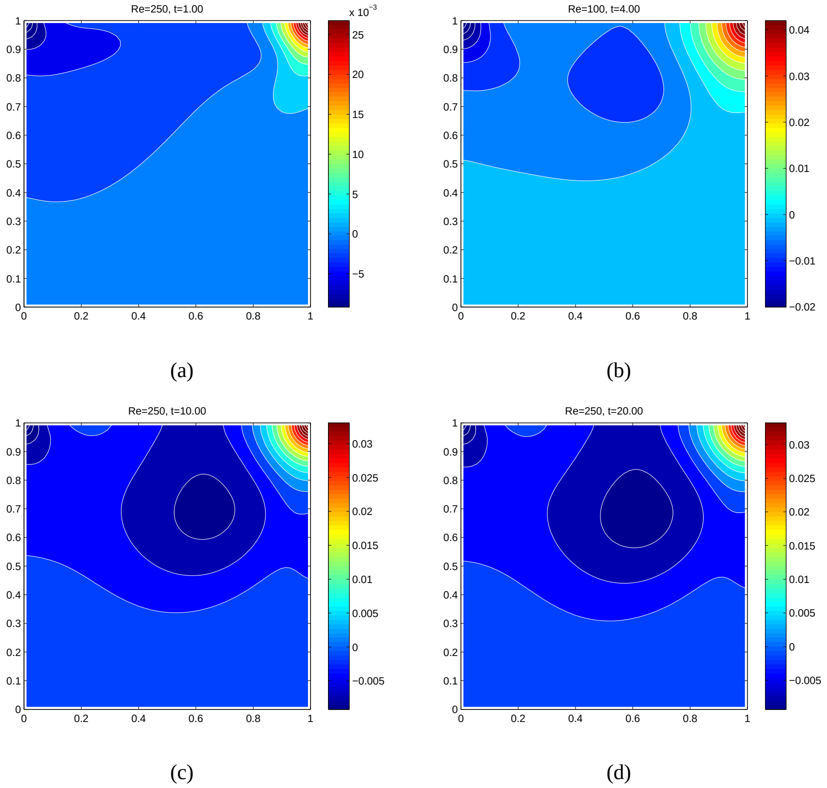

(a) (b)

(c) (d)

Figure 3.8: Pressure fields for $Re = 250$ *at time (a) t=1, (b) t=4, (c) t=10, and (d) t=20.*

The desired macroscopic point $y^d_{2,2}$ for $Re = 100$ is 0.0081 and for $Re = 250$ is 0.0152, as illustrated in Figures 3.9(a) and 3.9(b), respectively. After $y^d_{2,2}$ is determined, the parameters $K^P_{2,2}$ and $K^I_{2,2}$ can be tuned to enhance the asymptotic output regulation for the chosen macroscopic space, i.e., $\lim_{t\to\infty} h_{2,2}(z_{i,j}) = \overline{E}^d_{2,2}$ and $\lim_{t\to\infty} e_{2,2} = 0$. By tuning the control parameters the $K^P_{2,2}$ and $K^I_{2,2}$, the error convergences to zero, and the desired output is reached arbitrary fast. The control parameters can be tuned until a desired performance is obtained. The effectiveness of the controlled (i.e., closed-loop) system achieved by tuning the control parameters is shown in Figure 3.10 for $Re = 100$ and Figure 3.11 for $Re = 250$. First, it was observed that applying a high gain leads to flow instability and transition regimes that need longer time to be stabilized by the controller. Second, for small values of $K^I_{2,2}$, the observed macroscopic energy level moves towards the reference level, whereas for larger values of $K^I_{2,2}$, the error approaches zero with a small bounded oscillation.

The satisfactory output regulation of the chosen macropic energy level in $\overline{\Omega}_{2,2}$ for

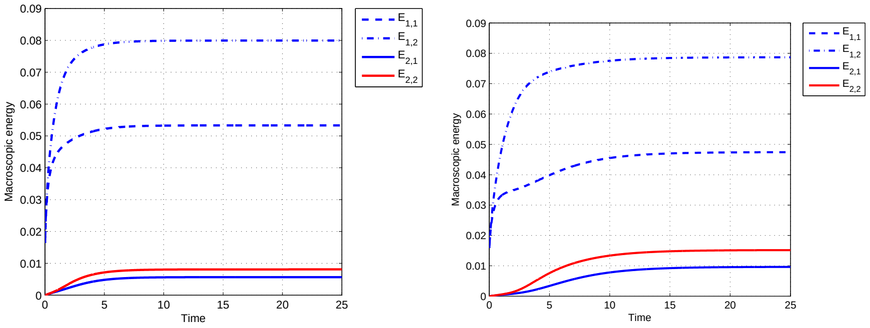

(a) (b)

Figure 3.9: Time evolution of the macroscopic energy distributions $E_{k,k}$ *in* $\overline{\Omega}_{k,k}$ *domain for (a)* $Re = 100$ *and (b)* $Re = 250$.

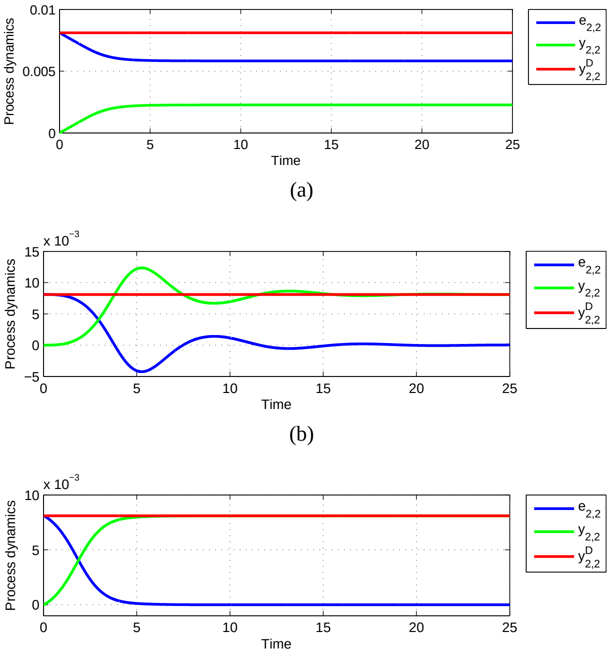

(a)

(b)

(c)

Figure 3.10: Feedback control of the lid-driven cavity case for $Re = 100$ *with the control parameter: (a)*$K^P_{2,2} = 100$, *(b)* $K^I_{2,2} = 62$, *and (c)* $K^P_{2,2} = 100$ *and* $K^I_{2,2} = 62$.

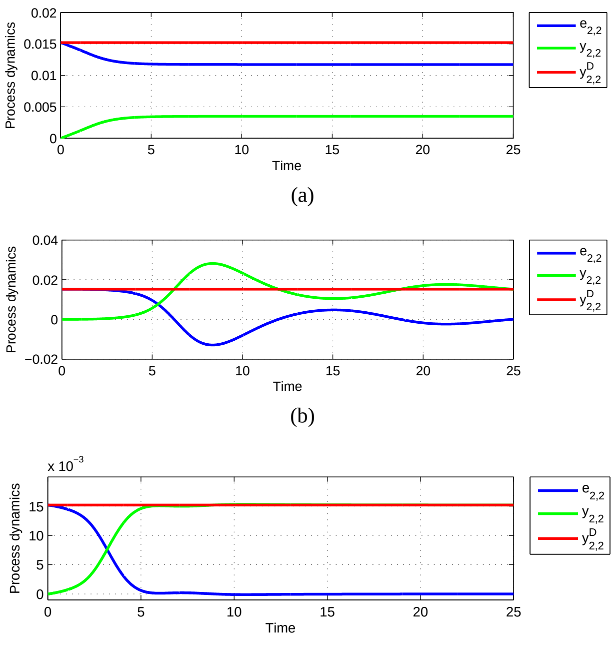

(a) (b) (c)

Figure 3.11: Feedback control of the lid-driven cavity case for $Re = 250$ *with the control parameter: (a)*$K^P_{2,2} = 60$*, (b)* $K^I_{2,2} = 21$*, and (c)* $K^P_{2,2} = 60$ *and* $K^I_{2,2} = 21$.

both *Re* are guaranteed with the control parameters given in Table 3.5.

Table 3.2: Control parameters for macroscopic output regulation of energy level in $\overline{\Omega}_{2,2}$.

Re	$\overline{E}_{2,2}$	$K^P_{2,2}$	$K^I_{2,2}$
100	0.0081	100	62
250	0.0152	60	21

To examine the controlled and uncontrolled flow, we compare the microscopic energy fields for the controlled and uncontrolled flow. The steady-state flow without any control action is obtained at $t = 25$ for both *Re*, whereas the controlled flow reaches the same energy distribution at $t = 4$ for $Re = 100$, and at $t = 7$ for $Re = 250$. The simulation results show that the structural numerical approach to the fluid flow control can be effectively used for the flow regulation in the cavity at $Re = 100$ and $Re = 250$.

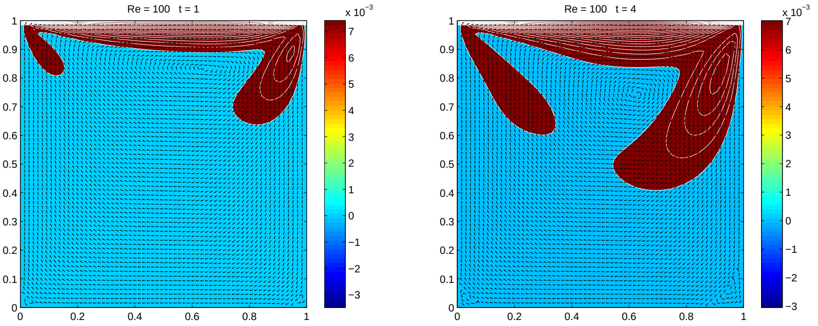

(a)

(b)

Figure 3.12: Time sequences of the controlled velocity vector field and the energy field for $Re = 100$ $Re = 100$ *at time (a) t=1 and (b) t=4.*

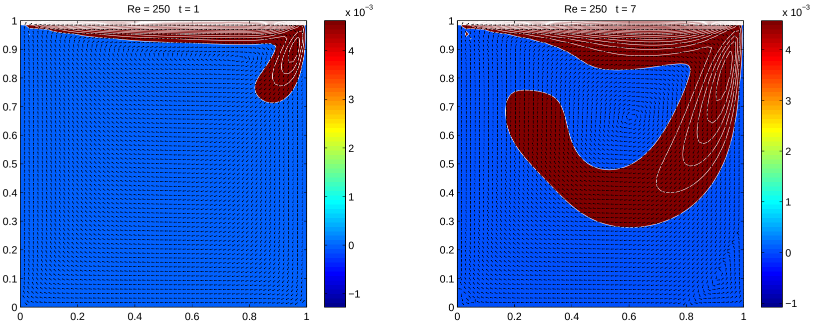

(a)

(b)

Figure 3.13: Time sequences of the controlled velocity vector field and the energy field for $Re = 250$ *at time (a) t=1 and (b) t=7.*

It is important to mention that the algorithm used in this example cannot capture dynamics of turbulent flow regimes; however, it can capture any fluctuations from the desired energy level. Therefore, it is highly appreciated to have a well-suited numerical algorithm in order to obtain a solution to the microscopic fluid flow model, and it is also crucial for a reliably quantification of the corresponding macroscopic output. Finding a good compromise between the microstates for accurate and the macrostates for the control design is important for stable computations and applicability of the macroscopic control designed presented in Section 3.4.2.

3.6 Discussion

In this chapter, we presented the numerical approach to a microscopic model that describes fluid flow. This research direction was discussed in Chapter 1 along the research direction **RD1** illustrated in Figure 1.3. The main contribution of this chapter is in the proposed output regulation based on a macroscopic quantity of fluid properties. In fact, we use the microscopic scale to guarantee a solution to the PDE, and the macroscopic scale for control design. We have shown that the complexity of the control design in fluid flows can be considerably reduced by taking into account different modeling scales (i.e., multiscale modeling). In contrast to the microscopic phenomenological approach which falls under the classical domain of physics, control-oriented modeling aims to describe the dominant dynamics of the fluid flow and understand the dynamics in order to design a control strategy. Therefore, the macroscopic control design presents a valuable contribution of theory to practice in the chemical industry.

From the simulation point of view, the macroscopic simulation approach seems to be less attractive than the microscopic approach due to the low accuracy. However, from the control perspective, the macroscopic approach to the fluid system has enormous potential for industrial applications since it requires only four outputs for the given design. The macroscopic flow regulation is a simple trade-off between simplicity and accuracy that leads to a structural control design based on the centralized boundary control design. The control approach to the hydrodynamics gives the closed-loop form of the fluid system, where the control parameters can be tuned to obtain the desirable performance determined by the production process. The most important feature of the control approach to the hydrodynamics is that it offers a wide range of possibilities to influence the hydrodynamics otherwise unreachable by a classical physics approach to fluid systems. In classical physics, influencing the fluid system is usually done by a trial-and-error approach to the boundary conditions. This trial and error approach to the boundary conditions can easily lead to stability problems, to problems of choosing inappropriate numerical schemes and discretization method, etc. Since the main control objective is to control and manipulate processes in a structural and easy way, this trial-and-error approach is unacceptable. For this reason, the multiscale modeling is a very important aspect in fluid flow modeling that can be very advantageous for control designs. Furthermore, the concept of a macroscopic output regulation can be tested for a wide range of feedback and feedforward control designs available.

In the next chapter, we will derive a microscopic control-oriented two-phase flow model that can be used for designing a similar boundary controller, and we will verify the importance of control-oriented microscopic modeling of fluid flow systems for control design.

Chapter 4

Control-Oriented Modeling of Two-Phase Flow

In the previous chapters, we introduced the microscopic model of single-phase flow and a boundary control strategy based on the numerical approach to microscopic models (see **RD1** in Chapter 1). In this chapter, we will develop a control-oriented microscopic two-phase flow model for the flow inside bubble columns based on a set of assumptions that can be used to reduce the model complexity of the multiphase flow discussed in Section 2.2.3. At this stage of the development of a control-oriented two-phase flow model, we will focus mainly on understanding the complex nature of hydrodynamics behind the two-phase flow and on development of different input/output structures. In this chapter, particular attention is given to the issues related to well-posedness, coupling terms, eigenvalues, steady-state solutions, and boundary actuation strategies for the derived two-phase fluid flow system.

4.1 Introduction

In this chapter, we will derive a control-oriented microscopic two-phase flow model which will be treated in the remaining chapters of this thesis. The derived control-oriented microscopic two-phase flow model provides a new aspect of modeling two-phase flow systems and control of two-phase flow systems. The key aspect in developing the control-oriented two-phase flow model is that a very strong mathematical theory is needed to study the well-posedness of the model formulation and the well-posedness of boundary conditions before using any numerical methods to approximate the solution. As discussed in Chapter 1, the model-based control strategy for two-phase fluid flow systems should not rely on the numerical methods behind the currently used CFD models. Instead, it should provide a theoretical framework for the development of different input/output strategies using available analytical tools. Furthermore, in this chapter, we will introduce a list of modeling assumptions, according to the aspects stated in Section 2.5, which eventually lead to the derivation of the final compact form of the control-oriented two-phase flow model for gas-liquid systems. The main focus of this chapter is on the well-posedness of the derived control-oriented two-phase flow model and on the methods available to relate the well-posed problems to the type of PDE models as discussed in Section 2.3.3. The method based on eigenvalue analysis which directly links the model formulation with the well-posed boundary conditions will be used to derive a well-posed actuation strategy. To motivate this observation, we will introduce the linearization technique and coordinate transformations for which a very general decomposition theorem is applicable. The coordinate transformations will enable developments that will be presented for causal input/output relationships between boundaries in Chapter 5, and for different spatially distributed control designs in Chapter 6.

This chapter starts with a brief description of two-phase fluid flow systems (see Section 4.2.1), with an overview of the literature presented in Chapter 1. This overview is intentionally not complete, and it aims only to present the important concepts and issues related to the microscopic modeling of two-phase flow. There are many other results in the field that can be found in the CFD and multiphase flow literature. Section 4.2.2 contains a set of modeling assumptions used to derive a 1D two-phase flow model. The well-posedness of the model is studied in Section 4.2.4. In Section 4.3, we introduce the method of characteristics for the derived PDE model to define a well-posed boundary actuation strategy for the given control-oriented microscopic two-phase flow model. The problem of the well-posed boundary actuation strategy is studied on a linearized PDE model which is obtained using a linearization technique similar to the linearization technique presented in [1] for the single-phase flow. The linearized model allows us to introduce the definition of decoupled systems which will be the subject of Section 4.3.4 of this thesis and later chapters. Finally, in Section 4.5, we present numerical results which illustrate the presented theoretical framework.

4.2 Two-Phase Flow Models

4.2.1 Introduction

Two-phase flow is of great relevance for many industrial applications ranging from the chemical industry to oil production and nuclear engineering. It is generally understood as a simultaneous flow of two interactive and different phases (see Chapter 1). In most cases, the phases are simply referred to as gas/vapor, liquid, or solid state [1]. According to the combinations of the phases, it is easy to classify two-phase mixtures as

- gas-liquid,
- gas-solid, and
- liquid-solid.

---

[1] Plasma is lately considered to be a distinct state of matter as well.

For a long time, the analysis of two-phase flow processes was limited to mostly empirical correlations, or to largely simplified engineering models [18, 36, 37]. In recent years, due to the wide range of applications, great effort has been spent on the analysis of fluid dynamics in two-phase systems, and on the development of related numerical simulation methods [47, 51, 92]. The microscopic models for two-phase flow in the fluid dynamics approach have been mostly derived from the fluid dynamics of the single-phase flow with specific interactions between the phases (see Section 2.2.3). The result of this approach is a set of equations having a similar structure as the single-phase flow (i.e., the Navier-Stokes equations) from which they originated. The currently used models rely on different interactive phenomena between the phases with specific physical background and closure equations [51].

In this chapter, instead of using CFD two-phase flow models, we will develop a control-oriented model which comprises the findings from the previous chapters and multiphase flow literature. The results contained in this chapter have been published in [39].

4.2.2 1D Two-Phase Flow Model for Gas-Liquid Systems

In order to develop a comprehensive strategy for a two-phase flow system inside a reactor column illustrated Figure 1.2, the first step is to define a problem of our interest and a set of assumptions needed to simplify the problem (see Section 2.5). The following assumptions have been made in order to derive a control-oriented microscopic two-phase flow model based on the microscopic conservation laws discussed in Chapter 2:

- The fluids (gas and liquid) are considered to be incompressible.
- The entire volume is occupied by gas and liquid and is defined by the volume fractions of the gas phase α_g and the liquid phase α_l, and for each volume element $\alpha_g + \alpha_l = 1$ holds.
- The flow over the entire cross section is uniform, i.e., the flow variations occur only in 1D.
- The gas phase is dispersed and consists of bubbles which are spherical in shape and uniform in size. The processes of coalescence and breakage are neglected.
- No mass transfer occurs between the two phases.
- Each phase is treated as a continuum in any size of the domain under consideration.
- In each volume element, there is a sufficiently large number of bubbles that create the continuum gas phase.
- The pressure influence is modeled by distinguishing a bulk pressure and an interfacial pressure.

- The pressure in each volume element is assumed to be shared by the phases proportional to the fractional area occupied by the phases.
- The interfacial tension also causes the pressure $\triangle p_g$ for the tension from the gas side, and $\triangle p_l$ for the tension from the liquid side at the surface.
- The drag force is considered to be the only coupling term between the phases as described in (2.13). All the other coupling terms are neglected.

According to the given assumptions, a 1D form of the microscopic conservation laws can be obtained. The following set of PDEs based on the mass conservation laws (see Section 2.2.2) and the momentum conservation laws (see Section 2.2.3) is obtained. The mass conservation laws for both phases read as

$$\frac{\partial \alpha_g}{\partial t} + \frac{\partial \alpha_g}{\partial x} v_g + \alpha_g \frac{\partial v_g}{\partial x} = 0, \tag{4.1}$$

$$\frac{\partial \alpha_l}{\partial t} + \frac{\partial \alpha_l}{\partial x} v_l + \alpha_l \frac{\partial v_l}{\partial x} = 0, \tag{4.2}$$

and the momentum conservation laws for both phases read as

$$\alpha_g \rho_g \frac{\partial v_g}{\partial t} + \alpha_g v_g \rho_g \frac{\partial v_g}{\partial x} + \alpha_g \frac{dp}{dx} + \triangle p_g \frac{\partial \alpha_g}{\partial x} = -\alpha_g \rho_g g - \beta \left(v_g - v_l\right), \tag{4.3}$$

$$\alpha_l \rho_l \frac{\partial v_l}{\partial t} + \alpha_l v_l \rho_l \frac{\partial v_l}{\partial x} + \alpha_l \frac{dp}{dx} + \triangle p_l \frac{\partial \alpha_l}{\partial x} = -\alpha_l \rho_l g + \beta \left(v_g - v_l\right), \tag{4.4}$$

where α_g is the volume fraction of the gas phase, v_g is the velocity of the gas phase, and v_l is the velocity of the liquid phase, with the drag force closed by the following equation

$$\beta = \frac{3C_d}{4d_b} \alpha_g \alpha_l \rho_l |v_g - v_l|,$$

where C_d is the drag coefficient and d_b is the diameter of a single bubble. In principle, the balance equations are derived for each phase separately and are coupled via interactive terms given as (2.13). According to the given assumption, the drag force is considered to be the most dominant coupling term

$$F = F_d = \beta \left(v_g - v_l\right),$$

which appears on the right-hand side of (4.3) and (4.4). Many of the presently used two-phase flow models use different interfacial coupling terms with sometimes ambiguous physical background and empirical closure equations [51]. Thus, we consider only the most dominant coupling term which is the drag force.

In setting the momentum balance equations, we use the interfacial pressures $\triangle p_g$ and $\triangle p_l$ in (4.3) and (4.4) respectively, which can also be considered as coupling terms since they are functions of v_g and v_l. The liquid interfacial pressure can be obtained from the following expression

$$\triangle p_l = C_p \alpha_l \rho_l (v_g - v_l)^2,$$

where C_p is the interfacial pressure coefficient [71, 80]. The pressure difference $\triangle p_g$ can be neglected due to the low density of the gas phase.

As far as the total pressure is concerned, the momentum balance equations (4.3) and (4.4) share the pressure term proportional to the gas fractions. This fact can be used to derive a more compact representation of the two-phase flow. The pressure term can be eliminated by dividing (4.3) and (4.4) by α_g and α_l, respectively, and subtracting one from the other. Under conditions that $\alpha_g \neq 0$ and $\alpha_l \neq 0$, we can obtain the total momentum equation of the two-phase flow system as

$$\begin{aligned}\rho_g \frac{\partial v_g}{\partial t} - \rho_l \frac{\partial v_l}{\partial t} + \rho_g v_g \frac{\partial v_g}{\partial x} - \rho_l v_l \frac{\partial v_l}{\partial x} + C_p \rho_l (v_g - v_l)^2 \frac{\partial \alpha_g}{\partial x} \\ = -(\rho_g - \rho_l) g - (v_g - v_l) \left(\frac{\beta}{\alpha_g} + \frac{\beta}{\alpha_l} \right).\end{aligned} \tag{4.5}$$

Equation (4.5) describes the total momentum of the mixture with no pressure variation outside the system boundaries. The signs in front of the time derivatives can be assigned to the direction of the velocities.

Before writing the final form of the model, we can make one more simplification step. Due to the assumption that the volume under consideration is occupied with gas and liquid, i.e., $\alpha_g + \alpha_l = 1$, (4.2) can be rewritten in terms of only α_g as

$$\frac{\partial (1-\alpha_g)}{\partial t} + \frac{\partial (1-\alpha_g)}{\partial x} v_l + (1-\alpha_g) \frac{\partial v_l}{\partial x} = 0. \tag{4.6}$$

After rearranging, (4.6) reads as

$$\frac{\partial \alpha_g}{\partial t} + \frac{\partial \alpha_g}{\partial x} v_l - (1-\alpha_g) \frac{\partial v_l}{\partial x} = 0. \tag{4.7}$$

The last step includes subtracting (4.1) from (4.7). Now, the final set of PDEs can be written as

$$\begin{aligned}\frac{\partial \alpha_g}{\partial t} + \frac{\partial \alpha_g}{\partial x} v_g + \alpha_g \frac{\partial v_g}{\partial x} = 0, \\ \rho_g \frac{\partial v_g}{\partial t} - \rho_l \frac{\partial v_l}{\partial t} + \rho_g v_g \frac{\partial v_g}{\partial x} - \rho_l v_l \frac{\partial v_l}{\partial x} + C_p \rho_l (v_g - v_l)^2 \frac{\partial \alpha_g}{\partial x} \\ = -(\rho_g - \rho_l) g - (v_g - v_l) \left(\frac{\beta}{\alpha_g} + \frac{\beta}{1-\alpha_g} \right), \\ \frac{\partial \alpha_g}{\partial x} (v_g - v_l) + \frac{\partial v_g}{\partial x} \alpha_g + (1-\alpha_g) \frac{\partial v_l}{\partial x} = 0,\end{aligned}$$

which in a compact form reads as

$$\mathbf{E} \frac{\partial \Phi}{\partial t} + \mathbf{A(\Phi)} \frac{\partial \Phi}{\partial x} = \mathbf{c(\Phi)}, \tag{4.8}$$

where $\Phi = \begin{bmatrix} \alpha_g & v_g & v_l \end{bmatrix}^T$ is the vector of fluid variables. The matrices

$$\mathbf{E} = \begin{bmatrix} 1 & 0 & 0 \\ 0 & \rho_g & -\rho_l \\ 0 & 0 & 0 \end{bmatrix}, \tag{4.9}$$

and

$$\mathbf{A(\Phi)} = \begin{bmatrix} v_g & \alpha_g & 0 \\ C_p \rho_l (v_g - v_l)^2 & \rho_g v_g & -\rho_l v_l \\ v_g - v_l & \alpha_g & 1 - \alpha_g \end{bmatrix}, \tag{4.10}$$

are the system matrices, and

$$\mathbf{c(\Phi)} = \begin{bmatrix} 0 \\ -(\rho_g - \rho_l)g - (v_g - v_l)\left(\frac{\beta}{\alpha_g} + \frac{\beta}{1-\alpha_g}\right) \\ 0 \end{bmatrix} \tag{4.11}$$

is the coupling force vector. Equation (4.8) is just a simplified representation of (2.11) and (2.10), where the variation of fluid variables is observed in 1D space direction with additional assumptions outlined at the beginning of this section. A similar set of simplification steps has been published in [73] where the coupling forces between the phases were studied using a two-phase flow model for adiabatic two-phase bubble flow. The interfacial momentum exchange includes the surface stress developed on the interface, which is induced by the relative motion of the phases, interfacial pressure, and the drag force. In this work, we focus on the drag force and interfacial pressure only for the incompressible two-phase fluid flow system.

4.2.3 Linearized Model Representation

A linear approximation of nonlinear models aims to analyze the local behavior of a system. This is a very important aspect of the linearized model representation, which is widely used in control theory to design controllers that can stabilize system behavior around the chosen operational regime. In the following sections, we will utilize the linearized model to analyze the well-posedness of the model formulation described by the nonlinear PDAE (4.8) and to define conditions for a well-posed boundary actuation strategy. Even though we will study the linearized model that shows local behavior of the two-phase flow system, the results obtained are very relevant for spatially distributed control designs that will be introduced in Chapter 6 and can be extended for the nonlinear PDAE model.

4.2.4 Well-Posedness of the Model Formulation

As we already discussed in Section 2.3.3, the first step in defining the well-posedness of the model formulation is to classify the derived PDE model and to suggest the well-

Table 4.1: Well-posed regions of the two-phase flow model based on the eigenvalues (4.15) and (4.16) for a wide range of the velocities v_g and v_l, where $\alpha_g = 0.1$, $\rho_g = 1\ kg/m^3$, and $\rho_l = 1000\ kg/m^3$.

Eigenvalues	Velocity conditions obtained from (4.15) and (4.16)	Ratio between the velocities
$\lambda_1 = \lambda_2$	$-0.45v_g + 1.45v_l =$ $= 0.47v_g + 0.53v_l$	$v_l/v_g = 1$
$\lambda_1 > 0$ $\lambda_2 > 0$	$v_l/v_g > -0.89$	$v_l/v_g > 0.3$ $v_l/v_g > 0.3$
$\lambda_1 < 0$ $\lambda_2 > 0$	$v_l/v_g > -0.89$ $v_l/v_g < 0.3$	$-0.89 < v_l/v_g < 0.3$
$\lambda_1 < 0$ $\lambda_2 < 0$	$v_l/v_g < -0.89$ $v_l/v_g < 0.3$	$v_l/v_g > -0.89$

posed initial-boundary conditions. The nature of possible solutions to (4.8) is essentially characterized by coefficients of a characteristic polynomial obtained from the system matrices of the derived model (4.9) and (4.10). For PDAE models, the degree of the characteristic polynomial is smaller than or equal to the number of states. This means that the eigenvalues corresponding to the algebraic part have eigenvalues with infinitely many solutions, and the eigenvalues with the finite solutions correspond to the dynamical part. For the model given as (4.8), the eigenvalue analysis shows that the system has one infinite eigenvalue and two finite eigenvalues which can be obtained from the characteristic polynomial

$$\det(\lambda\mathbf{E} - \mathbf{A}(\Phi)) = a_1\lambda^2 + a_2\lambda + a_3, \tag{4.12}$$

where

$$\begin{aligned}
a_1 &= -\alpha_g\rho_l - \rho_g + \rho_g\alpha_g, \\
a_2 &= 2\,\rho_g v_g - 2\,v_g\rho_g\alpha_g + 2\,\alpha_g\rho_l v_l, \\
a_3 &= -C_p\,\rho_l\,(v_g - v_l)^2\,{\alpha_g}^2 + \left(\rho_g {v_g}^2 - \rho_l {v_l}^2 + C_p\,\rho_l\,(v_g - v_l)^2\right)\alpha_g - \rho_g {v_g}^2.
\end{aligned}$$

The discriminant of (4.12) is then defined by

$$D_c = a_2^2 - 4a_1a_3. \tag{4.13}$$

If $D_c > 0$, the system (4.8) is said to be hyperbolic [50, 77]. In this case, the eigenvalues of the hyperbolic equations are real and distinct. If $D_c = 0$, the system is parabolic with real repeated eigenvalues. If $D_c < 0$, the system is elliptic with complex eigenvalues. In general, elliptic system with one coordinate being time are proven to be ill-posed, whereas parabolic and hyperbolic systems are well-posed with a stable and unique solution [77]. This was discussed in Section 2.3.1. This means that the well-posedness of (4.8) is defined by the eigenvalues of the pair ($\mathbf{A(\Phi)}$,$\mathbf{E}$) and the system parameters of the derived two-phase flow model [80]. In order to define a critical point between the well-posed and ill-posed solutions of the derived two-phase flow model (4.8), we evaluate (4.13) as

$$D_c = D\left(1 - \left(\frac{\rho_l\alpha_g + \alpha_l\rho_g}{\rho_g}\right)C_p\right), \tag{4.14}$$

where $D = \alpha_g\rho_g\rho_l\,(v_g - v_l)^2\,(-1+\alpha_g)$. Since $\alpha_g < 1$, then the discriminant is negative, i.e., $D < 0$ for all values of the velocities v_g and v_l. This implies that the well-posedness of the PDAE model is determined by the interfacial pressure coefficient C_p. The critical C_p, for which the discriminant $D_c = 0$ and the system is parabolic, can be obtained from the system parameters ρ_g and ρ_l, and the volume fraction α_g as

$$C_p = \frac{\rho_g}{\alpha_g\rho_l + \rho_g\alpha_l}.$$

There have been many studies over the last two decades focusing on the interfacial pressure coefficient C_p for different fluid systems [51]. For the air-water system, which will be treated in this thesis, the interfacial pressure coefficient C_p is reported to be between 0.25 and 0.5 [73]. For this value of C_p, the derived two-phase flow model (4.8) is well-posed for a wide range of gas fractions, α_g (see Table 4.1).

4.2.5 Eigenvalue Analysis

After deriving the 1D two-phase flow model, we are in position to obtain the eigenvalues of (4.8) from the following expressions

$$\lambda_1(\Phi) = \frac{\alpha_g\rho_l v_l + \alpha_l\rho_g v_g}{\alpha_g\rho_l + \alpha_l\rho_g} + \sqrt{D_c}, \tag{4.15}$$

$$\lambda_2(\Phi) = \frac{\alpha_g\rho_l v_l + \alpha_l\rho_g v_g}{\alpha_g\rho_l + \alpha_l\rho_g} - \sqrt{D_c}. \tag{4.16}$$

These eigenvalues represent the characteristic velocities of the gas/liquid phase in the two-phase fluid flow system. Due to the fact that $\rho_g > 0$ and $\rho_l > 0$, the signs of the eigenvalues change according to the velocities v_g and v_l. The results of the eigenvalues and the range of the velocities for which the model is well-posed are given in Table 4.1. In the range outside the given velocity ratios, the model is ill-posed. In Figures 4.1 and 4.2, we present an analysis of the eigenvalues for $\alpha_g = 0.1$, $\rho_g = 1$ kg/m^3, and $\rho_l = 1000$ kg/m^3 in order to illustrate the velocity influence on the characteristic polynomial.

Figure 4.1(a) illustrates the influences of the velocity of the gas phase on the characteristic polynomial, whereas the influence of the velocity of the liquid phase on the characteristic polynomial is shown in Figure 4.1(b). The arrows in Figures 4.1(a) and 4.1(b) indicate the direction of the increased gas and liquid velocities, respectively. As

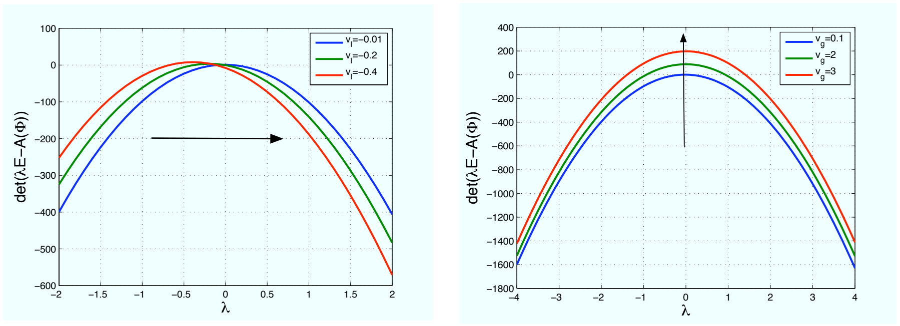

(a) (b)

Figure 4.1: Influence of the velocities v_g and v_l on the characteristic polynomial with the characteristic polynomial det$(\lambda \boldsymbol{E} - \boldsymbol{A(\Phi)})$ for (a) $v_g = 0.2\ m/s$ and (b) $v_l = -0.02\ m/s$.

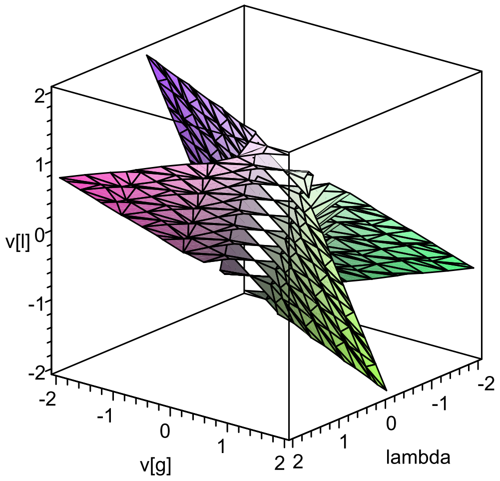

Figure 4.2: Hyperbolic region of the derived two-phase flow model for $\alpha_g = 0.1$.

can be observed from Figure 4.1(b), by increasing the gas velocity v_g, the characteristic curve is shifted upwards, and it crosses zero for a large value of the gas velocity v_g. These cross points are the eigenvalues given as (4.15) and (4.16). Depending on the values of the velocities v_g and v_l, we can determine the well-posed region of the derived two-phase flow model. The influence of v_l on the well-posedness of the solution is to some extent already determined by v_g since there is a strong relation between their eigenvalues. The effect of v_g and v_l on the characteristic polynomial is shown in 3D in Figure 4.2 for $\alpha_g = 0.1$. When $\lambda_1 = \lambda_2 = 0$, the model is parabolic whereas for the rest of the region the model is elliptic. For all possible signs of the eigenvalues, we refer to Table 4.1.

4.2.6 Summary of the Model Formulation

In the previous sections, we have derived a well-posed 1D two-phase flow model which is in agreement with the discussion given in Chapter 2, which describes the microscopic modeling of chemical processes. The given analysis of the well-posedness of the model formulation and influence of different terms in the derived two-phase flow model are written in a comprehensive manner that can be further used to develop actuation strategies. The derived two-phase flow model is similar to the model published in [73]. In contrast to the CFD model presented in [73], which aims to analyze all the effects of bubbles on two-phase flow, we focus mainly on the dominant dynamics of the two-phase flow system that are important for the structural development of well-posed actuation strategies and spatially distributed control designs. Our approach to the two-phase flow model is very different from the CFD models, as we will see in the following sections of this chapter, and in Chapters 5 and 6.

4.3 Boundary Conditions

4.3.1 Introduction

In Chapter 3, we saw that the boundary conditions of the lid-driven cavity case of single-phase flow can be used as inputs to control the flow in a structural way. In this section, we will first study the well-posedness of the boundary conditions for the derived two-phase flow model before we suggest different spatially distributed control strategies (see Chapter 6). Here, we will use the method of characteristics to study the boundary conditions and to define well-posed input/output structures for different flow regimes. Once the well-posed input/output structure has been obtained for all possible regimes, one can return to the original problem to seek the best control design. In general, it is more desirable to have a model which can be simulated with a well-posed input/output structure than to use large numerical algorithms which require a considerable computation time (see Chapter 1).

After the linearization that will be discussed in Section 4.3.3, we will apply a suitable transformation to eliminate the algebraic part of (4.8) and reduce the model to a PDE model (see Section 4.3.4). These two techniques allow us to consider the well-posedness of the boundary conditions and to determine different well-posed input/output structures.

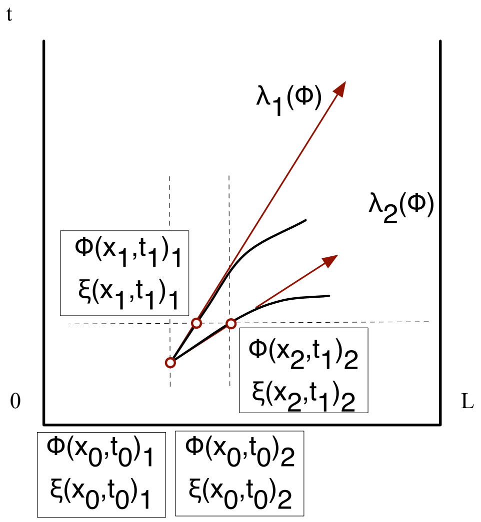

Figure 4.3: Characteristic curves of $\lambda_1(\Phi)$ *and* $\lambda_2(\Phi)$.

4.3.2 Method of Characteristics

As discussed in Chapter 2, the solution to a PDE model involves determining a well-posed boundary condition. Posing too many or fewer boundary conditions on a PDE model can lead to a non-uniqueness of the solution. Therefore, it is crucial for a successful control design to develop a control strategy that relies on a well-posed boundary condition. In order to develop a well-posed boundary actuation strategy for the derived control-oriented model of the two-phase flow, we introduce the characteristic curve analysis of the linearized two-phase flow model based on the method of characteristics. The characteristics represent lines with characteristic directions as shown in Figure 4.3. The curves shown in Figure 4.3 represent nonlinear characteristic curves and their linear approximations. The analysis of the characteristic curves provides several important conclusions concerning the boundary conditions for the model written as (4.8), which will be discussed later in this section.

Using the method of characteristics, a set of PDEs can be transformed into a set of ODEs along the characteristic directions in the (x,t)-plane. To prove this statement, we start with the elementary calculus for a set of nonlinear PDEs where

$$\frac{d\Phi(t,x)}{dt} = \frac{\partial\Phi(t,x)}{\partial t} + \frac{\partial\Phi(t,x)}{\partial x}\frac{dx}{dt}. \tag{4.17}$$

The left-hand side of (4.17) is a total derivative of Φ along curves defined by the coef-

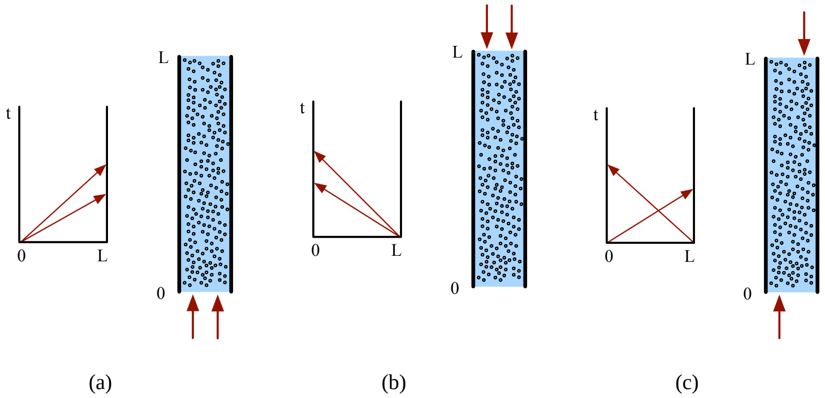

Figure 4.4: The wave propagation along characteristic curves and boundary conditions for (a) $\lambda_1(\Phi) > 0$ *and* $\lambda_2(\Phi) > 0$, *(b)* $\lambda_1(\Phi) < 0$ *and* $\lambda_2(\Phi) < 0$, *and (c)* $\lambda_1(\Phi) > 0$ *and* $\lambda_2(\Phi) < 0$.

ficient in front of the time derivative dx/dt. Since (4.8) belongs to the class of PDAEs with **E** being a singular matrix, (4.17) has to be multiplied by **E**, i.e.,

$$\mathbf{E}\frac{d\Phi(t,x)}{dt} = \mathbf{E}\frac{\partial\Phi(t,x)}{\partial t} + \mathbf{E}\frac{\partial\Phi(t,x)}{\partial x}\frac{dx}{dt}. \tag{4.18}$$

Then the time evolution of (4.8) is set as

$$\mathbf{E}\frac{d\Phi}{dt} = \mathbf{c(\Phi)} \quad \text{along the curves defined by} \quad \mathbf{E}\frac{dx}{dt} = \mathbf{A(\Phi)}.$$

The characteristic curves of the linearized model in (x,t)-plane are shown in Figure 4.3 as vectors with the directions $\lambda_1(\overline{\Phi})$ and $\lambda_2(\overline{\Phi})$.

The directional derivatives, which correspond to the eigenvalues of the system matrices $(\mathbf{A(\Phi)},\mathbf{E})$ along the characteristic curves, can be defined by the following ODEs

$$\frac{d\xi_1}{dt} = \lambda_1(\Phi), \quad \text{and} \quad \frac{d\xi_2}{dt} = \lambda_2(\Phi).$$

The quantities ξ_1 and ξ_2 can be seen as the total derivatives in the (x,t)-plane, along the nonlinear curves defined by the ODEs [26, 34]. The eigenvalues, in essence, describe the direction of the wave propagation of the two-phase fluid flow.

According to the signs of the eigenvalues $\lambda_1(\Phi)$ and $\lambda_2(\Phi)$, different boundary actuation strategies are possible. Figure 4.4 illustrates the direction of the wave propagation according the eigenvalues $\lambda_1(\Phi)$ and $\lambda_2(\Phi)$, and the boundary conditions associated with the flow directions. For example, if the eigenvalues are negative, then the flow along both characteristic curves propagate as $\xi_1 = x - \lambda_1(\Phi)t$ and $\xi_2 = x - \lambda_2(\Phi)t$ in the (x,t) plane (see Figure 4.4(a)). This means that the boundary conditions must be specified at the location $x = 0$ as $\Phi(t,0)$, otherwise the boundary conditions are ill-posed (see Section 2.3.2). However, if the eigenvalues are negative, the flow along the characteristic curves are defined as $\xi_1 = x_1 + \lambda_1(\Phi)t$ and $\xi_2 = x_2 + \lambda_2(\Phi)t$, then the boundary conditions must be defined at the location $x = L$ as $\Phi(t,L)$. This situation is illustrated in Figure 4.4(b). It is rather common to have positive and negative eigenvalues, where for the positive eigenvalue the boundary condition has to be specified at the location $x = 0$ as $\Phi(t,0)$, whereas for the negative eigenvalue the boundary conditions has to be specified at the location $x = L$ as $\Phi(t,L)$. This type of flow represents counter-current flow which will be discussed in detail in Section 4.4. In Figure 4.4 next to the (x,t)-plots, we also show the bubble columns with different actuation strategies in order to give the physical interpretation of the given eigenvalue analysis. As can be seen, the physical interpretation of the characteristic curves analysis is rather straightforward. The waves with the characteristic velocities $\lambda_1(\Phi)$ and $\lambda_2(\Phi)$ carry the gas fraction of phases injected at the boundaries according to the signs of the characteristic velocities. When we inject the gas/liquid phase at the inlet/outlet, the phases will propagate upwards or downwards according to the signs of the eigenvalues $\lambda_1(\Phi)$ and $\lambda_2(\Phi)$.

4.3.3 Linearized Two-Phase Flow Model

In the previous section, we discussed the boundary conditions that immediately follow from the signs of eigenvalues that can be locally obtained (see Figure 4.3). This means that for the derived PDAE model (4.8), in each point in space, we have to determine the eigenvalues and locally approximate the nonlinear PDAE (4.8) by a linear one. This requires a large number of locally linearized equations. Since we are interested in developing an input/output structure for the derived two-phase flow model that can be used to control the fluid flow around different operational regimes, in this section we will introduce the linearization technique that can simplify the approach of the local linearization.

Suppose that $\overline{\Phi}$ is a steady-state solution of the derived two-phase flow model (4.8), and Φ' is a small perturbation around the steady-state solution, then the flow variable Φ can be written as

$$\Phi = \overline{\Phi} + \Phi', \tag{4.19}$$

and the linearized two-phase flow model can be defined as

$$\mathbf{E}\frac{\partial \Phi'}{\partial t} + \mathbf{A(\overline{\Phi})}\frac{\partial \Phi'}{\partial x} + \overline{\mathbf{A}}\mathbf{(\Phi')}\frac{\partial \overline{\Phi}}{\partial x} = \mathbf{F}\Phi', \tag{4.20}$$

with

$$\mathbf{A(\overline{\Phi})} = \begin{bmatrix} \overline{v_g} & \overline{\alpha_g} & 0 \\ C_p\,\rho_l\,(\overline{v_g} - \overline{v_l})^2 & \rho_g\overline{v_g} & -\rho_l\overline{v_l} \\ \overline{v_g} - \overline{v_l} & \overline{\alpha_g} & 1 - \overline{\alpha_g} \end{bmatrix},$$

$$\overline{\mathbf{A}}(\Phi') = \begin{bmatrix} {v_g}' & {\alpha_g}' & 0 \\ 2C_p\,\rho_l\,(\overline{v_g} - \overline{v_l})\,({v_g}' - {v_l}') & \rho_g {v_g}' & -\rho_l {v_l}' \\ v'_g - v'_l & {\alpha_g}' & -{\alpha_g}' \end{bmatrix},$$

representing the linearized system matrices, and

$$\mathbf{F} = \begin{bmatrix} 0 & 0 & 0 \\ 0 & -3/2\,\frac{C_d\,\rho_l \sqrt{\left(\overline{v_g} - \overline{v_l}\right)^2}}{db} & 3/2\,\frac{C_d\,\rho_l \sqrt{\left(\overline{v_g} - \overline{v_l}\right)^2}}{d_b} \\ 0 & 0 & 0 \end{bmatrix},$$

representing the linearized force vector. Here, we present the concept of the local behavior of the linearized two-phase flow, where the linearization procedure is given in Appendix B.

In essence, (4.20) represents the linearized two-phase flow model with the space dependent steady-state solution, according to the term $\frac{\partial \overline{\Phi}}{\partial x}$. The space dependent steady-state solutions, in essence, represent the flow patterns in the observed domain. If there is no variation of the steady-state solution with respect to space, i.e., $\overline{\Phi} = \text{const}$, the linearized two-phase flow model reduces to the following equation

$$\mathbf{E}\frac{\partial \Phi'}{\partial t} + \mathbf{A}(\overline{\Phi})\frac{\partial \Phi'}{\partial x} = \mathbf{F}\Phi'. \tag{4.21}$$

In general, a system of equations written as a linear set of equations represents small variations of properties. Here, the system matrices describe the rate of fluctuation in the neighborhood of $\overline{\Phi}$. If the flow is smooth in a sufficiently small neighborhood of the steady-state solution $\overline{\Phi}$, the fluctuations Φ' are essentially linear. As the fluctuation of the two-phase flow properties Φ' represents the small variation in the linear approximation of the two-phase flow model (4.8), one can think of the linear approximation as a linear deformation described by eigenvalues and eigenvectors of the linearized two-phase fluid flow model.

In order to demonstrate the linearization technique, simulations are carried out using a space independent steady-state solution i.e., quasi steady-state solution, while enforcing the well-posedness of the problem statement. The quasi steady-state solution, which is spatially uniform, can be used as an equilibrium point for the linearization of the two-phase flow model. Section 4.4 will discuss possible quasi steady-state solutions and their physical interpretations.

4.3.4 Coordinate Transformations

In this section, we use the linearized two-phase flow model (4.21) to reformulate the linear PDAE problem into a linear PDE using standard coordinate transformation techniques. It is important to emphasize that the coordinate transformations do not change the system dynamics, instead with the coordinate transformation the model is represented in another coordinate system. The linearized two-phase flow model written as a linear PDE model is beneficial for control designs, which will be illustrated in the following chapters. In Chapter 5, a causality problem of different input/output structures will be discussed, whereas a wide range of spatially distributed control designs will be shown in Chapter 6.

In this section, we introduce two sets of coordinate transformations: one that eliminates the algebraic part of the linearized two-phase flow model (4.21), and one that decouples the characteristic wave velocities $\lambda_1(\overline{\Phi})$ and $\lambda_2(\overline{\Phi})$. The first coordinate transformation is introduced in order to simplify the computations involving the algebraic equation in the linear PDAE model (4.21). First, the system matrix **E** in (4.21) has to be diagonalized, so that in the new coordinate system the linearized PDAE model (4.21) can be reduced by eliminating the algebraic equation. This means that the system can be decomposed into the dynamics part and the algebraic part by diagonalizing **E**

$$\mathbf{E}^D = \mathbf{E}\mathbf{T} = \begin{bmatrix} 1 & 0 & 0 \\ 0 & 1 & 0 \\ 0 & 0 & 0 \end{bmatrix}, \quad \text{and} \quad \mathbf{T} = \begin{bmatrix} 1 & 0 & 0 \\ 0 & {\rho_g}^{-1} & \rho_l \\ 0 & 0 & \rho_g \end{bmatrix} \quad \text{with } \Phi' = \mathbf{T}\Psi',$$

where **T** stands for the coordinate transformation matrix. Now, we can transform the state vector Φ' into a new state vector Ψ' such that according to the given fluid variables (α_g, v_g, and v_l), the new states are given as

$$\Psi' = \begin{bmatrix} \alpha'_g \\ \rho_g v'_g - \rho_l v'_l \\ \dfrac{v'_l}{\rho_g} \end{bmatrix}.$$

The two-phase flow model in the new coordinates Ψ' can be written as

$$\mathbf{E}\mathbf{T}\frac{\partial \Psi'}{\partial t} + \mathbf{A}(\overline{\Psi'})\mathbf{T}\frac{\partial \Psi'}{\partial x} = \mathbf{F}\mathbf{T}\Psi'. \tag{4.22}$$

Due to the simplicity, here, we use a symbolic representation of the linearized model (4.22), and later on we will present some numerical results. We start with the two-phase flow model (4.22) in the coordinates Ψ'

$$\begin{bmatrix} 1 & 0 & 0 \\ 0 & 1 & 0 \\ 0 & 0 & 0 \end{bmatrix} \frac{\partial \Psi'}{\partial t} + \begin{bmatrix} \overline{v_g} & \dfrac{\overline{\alpha_g}}{\rho_g} & \overline{\alpha_g}\rho_l \\ C_p\,\rho_l\,(\overline{v_g} - \overline{v_l})^2 & \overline{v_g} & \rho_g\overline{v_g}\rho_l - \rho_l\overline{v_l}\rho_g \\ \overline{v_g} - \overline{v_l} & \dfrac{\overline{\alpha_g}}{\rho_g} & \overline{\alpha_g}\rho_l + (1-\overline{\alpha_g})\,\rho_g \end{bmatrix} \frac{\partial \Psi'}{\partial x} = \tag{4.23}$$

$$\begin{bmatrix} 0 & 0 & 0 \\ 0 & -\frac{3}{2}\frac{C_d\,\rho_l\sqrt{(\overline{v_g}-\overline{v_l})^2}}{d_b\,\rho_g} & -\frac{3}{2}\frac{C_d\,\rho_l{}^2\sqrt{(\overline{v_g}-\overline{v_l})^2}}{d_b}+\frac{3}{2}\frac{C_d\,\rho_l\sqrt{(\overline{v_g}-\overline{v_l})^2}\rho_g}{d_b} \\ 0 & 0 & 0 \end{bmatrix}\Psi'.$$

The state Ψ'_3 can be obtained from the last equation in the diagonalized matrix form (4.23) as

$$\frac{\partial\Psi'_3}{\partial x}=\frac{(\rho_g\overline{v_g}-\rho_g\overline{v_l})}{\rho_g\left(-\overline{\alpha_g}\rho_l-\rho_g+\rho_g\overline{\alpha_g}\right)}\frac{\partial\Psi'_1}{\partial x}+\frac{\overline{\alpha_g}}{\rho_g\left(-\overline{\alpha_g}\rho_l-\rho_g+\rho_g\overline{\alpha_g}\right)}\frac{\partial\Psi'_2}{\partial x}. \tag{4.24}$$

Equation (4.24) can be used to eliminate the state Ψ'_3 from the linearized two-phase flow model (4.21) given in Ψ' coordinate system. After the elimination of Ψ'_3, the system contains only PDEs. The derived PDE model reads as

$$\frac{\partial}{\partial t}\begin{bmatrix}\Psi'_1\\ \Psi'_2\end{bmatrix}+\mathbf{A}_{\text{red}}\frac{\partial}{\partial x}\begin{bmatrix}\Psi'_1\\ \Psi'_2\end{bmatrix}=\mathbf{F}_{\text{red}}\begin{bmatrix}\Psi'_1\\ \Psi'_2\end{bmatrix}, \tag{4.25}$$

where $\mathbf{A}_{\text{red}}$ has the same eigenvalues as (4.8). The two-phase flow model written as (4.25) captures the flow dynamics in the Ψ' coordinate system, which are described by the eigenvalues of $\mathbf{A}_{\text{red}}$.

Now, we will introduce the second coordinate transformation which is used to decouple the directional derivatives $\frac{\partial\Psi'}{\partial x}$, i.e., diagonalize $\mathbf{A}_{\text{red}}$. First, we introduce the following coordinate transformation

$$\begin{bmatrix}\Psi'_1\\ \Psi'_2\end{bmatrix}=\mathbf{V}\begin{bmatrix}W'_1\\ W'_2\end{bmatrix},$$

where $\mathbf{V}$ is the transformation matrix that gives

$$\frac{\partial\mathbf{VW}'}{\partial t}+\mathbf{A}_{\text{red}}\frac{\partial\mathbf{VW}'}{\partial x}=\mathbf{F}_{\text{red}}\mathbf{VW}', \tag{4.26}$$

which reads as follows in the new coordinate system $\mathbf{W}'$

$$\frac{\partial\mathbf{W}'}{\partial t}+\mathbf{V}^{-1}\mathbf{A}_{\text{red}}\mathbf{V}\frac{\partial\mathbf{W}'}{\partial x}=\mathbf{V}^{-1}\mathbf{F}_{\text{red}}\mathbf{VW}'. \tag{4.27}$$

Equation (4.27) describes the linearized two-phase flow model written as the PDE with the decoupled wave propagation [2]. The final form of the linearized two-phase flow model with the decoupled directional derivatives can be written as

$$\frac{\partial}{\partial t}\begin{bmatrix}W'_1\\ W'_2\end{bmatrix}+\begin{bmatrix}\lambda_1 & 0\\ 0 & \lambda_2\end{bmatrix}\frac{\partial}{\partial x}\begin{bmatrix}W'_1\\ W'_2\end{bmatrix}=\begin{bmatrix}c_{11} & c_{12}\\ c_{21} & c_{22}\end{bmatrix}\begin{bmatrix}W'_1\\ W'_2\end{bmatrix}. \tag{4.28}$$

---

[2] The notation $(\cdot)'$ is used to emphasize the linear approximation of the nonlinear two-phase flow model written in different coordinate systems.

The solutions $W_1'(t,x)$ and $W_2'(t,x)$ represent the fluid variables in the new coordinate system, which are constant along the same characteristic lines $\frac{dx}{dt} = \lambda_1$ and $\frac{dx}{dt} = \lambda_2$ discussed in Section 4.3.2. Note that $\lambda_1 = \lambda_1(\overline{\Phi})$ and $\lambda_2 = \lambda_2(\overline{\Phi})$.

The coordinate transformations used in this section lead to the PDE model formulation of the two-phase flow (4.28) written in the coordinate system $\mathbf{W}'(t,x)$. Due to the model simplicity given in the $\mathbf{W}'(t,x)$ coordinate system, (4.28) is well-suited for different spatially distributed control designs that will be discussed in Chapter 6. In essence, the applied transformations are a permutation of the PDAE, and it also involves a full state transformation. In the case of full state transformation of $\Phi'(t,x)$, the new states $\mathbf{W}'(t,x)$ cannot be associated with physical states any more, but the relationships between new and old states are fixed by the transformation matrices $\mathbf{T}$ and $\mathbf{V}$. There are different arguments to arrive at a suitable coordinate system, which will be discussed in Section 4.5 and further extended in Chapter 5. Although the main purpose of the coordinate transformation presented in this section is to decouple the directional derivatives, the decoupled model also leads to the determination of a well-posed boundary actuation strategy. Furthermore, the coordinate transformations suggest a well-suited numerical scheme for spatial discretization of (4.28), which will be discussed in the next section.

4.3.5 Spatially Discretized Model

Another important aspect of the PDE models discussed in Chapter 2 is the choice of appropriate numerical schemes for the spatial discretization of the PDE models. The PDE models are usually numerically approximated by a large number of ODEs according to the chosen discretization schemes [76, 79]. The size of the derived ODE model depends on the number of discretization points and the accuracy of the discretization method used to approximate the PDE solution. In the fluid dynamics, the number of points depends on the problem formulation and chosen geometry, and it is typically in the range of 10^2 and 10^{15}. Furthermore, for the hyperbolic-like PDE models, the choice of the spatial discretization has to be in agreement with the direction of wave propagation. The direction of the wave propagation, which can be charactarized as positive or negative, has to agree with forward and backward numerical schemes. The forward and backward numerical schemes are given according to the sign of the eigenvalue λ as

$$\frac{dW_i'}{dt} = \lambda \frac{W_{i+1}' - W_i'}{\triangle x} \quad \text{for } \lambda > 0, \tag{4.29}$$

$$\frac{dW_i'}{dt} = \lambda \frac{W_i' - W_{i-1}'}{\triangle x} \quad \text{for } \lambda < 0, \tag{4.30}$$

where $\triangle x$ represents the characteristic length defined between two points in space and index i denotes the point in space. It is also important to point out the consequences of the discretization methods. Choosing inappropriate numerical schemes may lead to numerical instabilities caused by discarding the direction of the wave propagation [42].

The discretized two-phase flow model can be obtained from (4.28) using either (4.29) or (4.30) according to the signs of the eigenvalues λ_1 and λ_1. For example, suppose that the two-phase flow propagates in the vertical column as illustrated in Figure 4.4(c), then the appropriate numerical scheme has to contain both discretization schemes. For $\lambda_1 < 0$, we use the forward discretization scheme (4.29) with the well-defined boundary conditions at the location $x = L$, whereas for λ_2 the backward discretization scheme (4.30) is necessary in order to obtain a numerically stable solution. After the spatial discretization, the spatially discretized two-phase flow model can be written as a large-scale linearized ODE model

$$\frac{d}{dt}\begin{bmatrix} \mathbf{W}'_{1,i} \\ \mathbf{W}'_{2,i} \end{bmatrix} = \begin{bmatrix} \mathbf{A}_{11} & \mathbf{A}_{12} \\ \mathbf{A}_{21} & \mathbf{A}_{22} \end{bmatrix} \begin{bmatrix} \mathbf{W}'_{1,i} \\ \mathbf{W}'_{2,i} \end{bmatrix} + \begin{bmatrix} \mathbf{B}_1 \\ \mathbf{B}_2 \end{bmatrix} W_{\text{in}}, \tag{4.31}$$

where

$$\mathbf{A}_{11} = \begin{bmatrix} -\lambda_1 + c_{11} & \lambda_1 & & & \\ & -\lambda_1 + c_{11} & \lambda_1 & & \\ & & \ddots & \ddots & \\ & & & -\lambda_1 + c_{11} & \lambda_1 \\ & & & & -\lambda_1 + c_{11} \end{bmatrix}, \quad B_1 = \begin{bmatrix} 0 \\ 0 \\ \vdots \\ 0 \\ \lambda_1 \end{bmatrix},$$

corresponds to the forward spatial discretization for $\lambda_1 > 0$, and

$$\mathbf{A}_{22} = \begin{bmatrix} \lambda_2 + c_{22} & & & & \\ -\lambda_2 & \lambda_2 + c_{22} & & & \\ & \ddots & \ddots & & \\ & & -\lambda_2 & \lambda_2 + c_{22} & \\ & & & -\lambda_2 & \lambda_2 + c_{22} \end{bmatrix}, \quad B_2 = \begin{bmatrix} -\lambda_2 \\ 0 \\ \vdots \\ 0 \\ 0 \end{bmatrix},$$

corresponds to the backward spatial discretization for $\lambda_2 < 0$. The off-diagonal matrices $\mathbf{A}_{12}$ and $\mathbf{A}_{21}$ in (4.31) contain only the coupling elements c_{12} and c_{21}, respectively.

$$\mathbf{A}_{12} = \begin{bmatrix} c_{12} & & & \\ & c_{12} & & \\ & & \ddots & \\ & & & c_{12} \end{bmatrix}, \quad \mathbf{A}_{21} = \begin{bmatrix} c_{21} & & & \\ & c_{21} & & \\ & & \ddots & \\ & & & c_{21} \end{bmatrix}.$$

The spatially discretized model (4.31) represents a microscopic interconnected form of the two-phase flow model, which is similar to the interconnected form of the single-phase flow presented in Section 3.4.1. Although the spatially discretized model might be difficult to approach and influence due to the size of the system matrix $\begin{bmatrix} \mathbf{A}_{11} & \mathbf{A}_{12} \\ \mathbf{A}_{21} & \mathbf{A}_{22} \end{bmatrix}$, the discretized model have a rather deterministic structure which can be exploited to reduce the computational complexity and design a simple spatially distributed controller. The spatially distributed control designs for the two-phase flow systems will be discussed in Chapter 6.

To illustrate the deterministic structure of the discretized two-phase flow model and to visualize sparsity patterns of the system matrices, the two-phase flow model written as (4.28) is descretized with $i = 1, 2, ..., 10$. The sparsity of the state matrix in (4.31) for two different cases are shown in Figure 4.5. Figure 4.5(a) shows the sparsity of the system matrix for the decoupled system where $c_{11} = c_{12} = c_{21} = c_{22} = 0$, and Figure 4.5(b) for the coupled system where $c_{11} \neq 0$, $c_{12} \neq 0$, $c_{21} \neq 0$, and $c_{22} \neq 0$. Both systems have rather deterministic structures which will be explored more on a numerical example in Section 4.5. Before we present the numerical results, we will introduce possible operational regimes that can be used as equilibrium points for the linearization derived in Section 4.3.3.

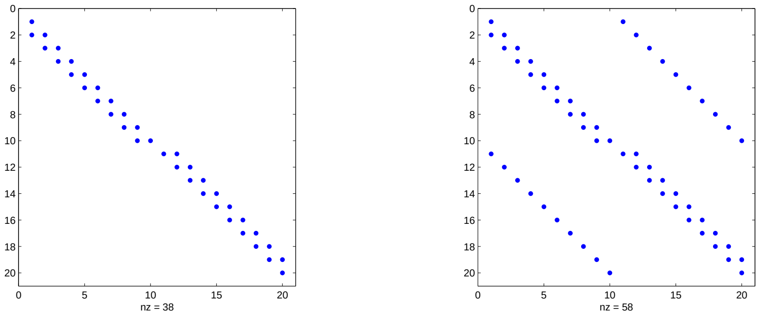

(a) (b)

Figure 4.5: Sparsity of the state matrix in (4.31) for i=1,2,...,10 where the dot indicates a non-zero entry for (a) a decoupled system where $A_{12} = A_{21} = 0_{10,10}$*, and (b) a coupled system were* $A_{12} \neq A_{21} \neq 0_{10,10}$.

4.4 Operational Regimes

4.4.1 Steady-State Solutions

As discussed in Section 1.3.2, there is a wide range of possible operational regimes in a bubble column [70]. For example, the bubble column reactor in a homogeneous regime is characterized by a more or less uniform gas volume fraction distribution within the reactor, whereas a heterogeneous regime is characterized by a non-uniform distribution and an internal re-circulation of the phases (see Figure 1.2). This means that a steady-state solution is space dependent for the non-uniform flow, whereas for the uniform flow, the gas distribution is constant in the entire space $\overline{\Phi} = \text{const.}$ As discussed in the previous sections, in this thesis we will only considered the space independent operational regimes and the linearized model (4.28) which represents the perturbation of the variables $\begin{bmatrix} W_1' \\ W_2' \end{bmatrix}$ around the space independent operational regime. This space independent steady-state solution will be called the quasi steady-state solution.

In the quasi steady-state situation, the gravitational force and the drag force are in balance, and the flow is uniform through the whole domain $[0, L]$ as illustrated in Figure 4.6 where the observed space is discretized according to the numerical methods presented in Section 4.3.5. The figure also illustrates two different flow regimes that often appear in bubble columns. Figure 4.6(a) illustrates a counter-current flow, whereas Figure 4.6(b) illustrates a co-current flow. The distinction between those flows is based on the direction of the phase velocities. Roughly speaking, if both phases move upwards (i.e., from bottom to top), the flow is considered to be co-current; whereas for fluid systems in which the phases flow in opposite directions, the flow is considered to be counter-current. To predict the direction of the velocities in the quasi steady-state regime, we introduce a slip velocity as a difference between the velocity of the gas phase and the velocity of the liquid phase, i.e., $v_s = v_g - v_l$. According to the definition of the slip velocity and its relationship to the velocities v_g and v_l, we can obtain the following expression from the momentum equations (4.3) and (4.4)

$$v_s = \sqrt{\frac{4}{3}\frac{(\rho_l - \rho_g) g d_b (1 - \alpha_g)}{C_d \rho_l}}.$$

In order to determine the gas and liquid velocities v_g and v_l in the quasi steady-state regime, we need an additional relation that will relate v_g and v_l. The additional equation can be obtained from the volumetric fluxes across the discretized volume sections. For a bubble column with an open flow through the boundaries (see Figure 4.6), the compensating volumetric flux across the volume in the quasi steady-state equals zero, i.e.,

$$\alpha_g v_g + \alpha_l v_l = 0.$$

In this case, the velocity of each phase can be computed as

$$\begin{aligned} v_g &= \alpha_l v_s, \\ v_l &= -\alpha_g v_s. \end{aligned}$$

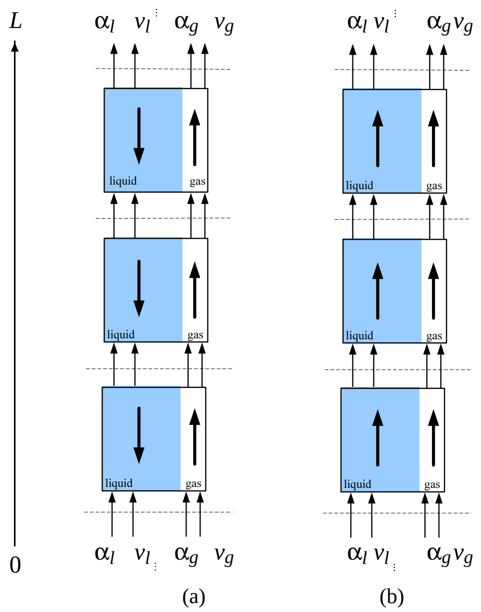

Figure 4.6: A spatially discretized model of bubble column reactor with open boundaries operating in two regimes: (a) counter-current and (b) co-current.

These relationships give a closing to the slip velocity and determine the quasi steady-state regime.

In the case of real flows, a certain amount of fluid moves downwards and a certain amount moves upwards. For the 1D two-phase flow, the liquid velocity simply represents a sum of the upwards and downwards flow:

$$v_l^{\text{down}} + v_l^{\text{up}} = v_l.$$

Which of the two liquid velocities is more dominant depends on the gas and liquid injection at the boundaries. In Section 4.5, we will illustrate the use of the quasi steady-state operational regimes in analyzing the boundary conditions, which leads to the development of well-posed actuation strategies.

4.4.2 Pressure Recovery

In the previous section, we studied the gas and liquid velocities in the quasi steady-state regime. Here, we will return to the momentum equations (4.3) and (4.4) to define the pressure in the quasi steady-state regime. Due to the fact that the model is obtained after a few simplification steps, in order to recover the pressure term in the steady-state regime, we have to consider (4.3) and (4.4) for $\frac{\partial v_g}{\partial t} = 0$ and $\frac{\partial v_l}{\partial t} = 0$ which are given by

$$\alpha_g v_g \rho_g \frac{\partial v_g}{\partial x} + \alpha_g \frac{dp}{dx} = -\alpha_g \rho_g g - \beta\,(v_g - v_l)\,, \tag{4.32}$$

and

$$\alpha_l v_l \rho_l \frac{\partial v_l}{\partial x} + \alpha_l \frac{dp}{dx} - C_p \rho_l (v_g - v_l)^2 \frac{\partial \alpha_g}{\partial x} = -\alpha_l \rho_l g + \beta\,(v_g - v_l)\,. \tag{4.33}$$

Adding (4.32) and (4.33), the pressure gradient can be calculated directly as

$$\frac{dp}{dx} = -\alpha_g v_g \rho_g \frac{\partial v_g}{\partial x} - \alpha_l v_l \rho_l \frac{\partial v_l}{\partial x} + C_p \rho_l (v_g - v_l)^2 \frac{\partial \alpha_g}{\partial x} - (\alpha_g \rho_g + \alpha_l \rho_l) g, \tag{4.34}$$

for the steady-state solution, and

$$\frac{dp}{dx} = -(\alpha_g \rho_g + \alpha_l \rho_l) g,$$

for the quasi steady-state where $\alpha_g = \text{const}$. As expected, the pressure in the quasi steadiness equals a hydrostatic pressure. Equation (4.34) has a form similar the Bernoulli equation written for the two-phase flow model [47]. To prove this statement, we can set $\alpha_g = 1$ in (4.34) which gives the following relation between the pressure and the gas velocity

$$\frac{dp}{dx} = -v_g \rho_g \frac{\partial v_g}{\partial x} - \rho_g g. \tag{4.35}$$

This verifies that our modeling assumptions introduced in Section 4.2.2 are well-posed.

In the following section, we will present numerical results of the discritized two-phase flow model (4.31) which is obtained from the linearized two phase flow model around the quasi steady-state solution.

4.5 Numerical Example

In this section, we establish the well-posed boundary conditions for the derived linearized two-phase flow model (4.31). This numerical example aims to get an additional insight behind fluid dynamics of two-phase flow and to develop a well-posed actuation strategy based on the theoretical framework previously discussed. The fluid properties and the system parameters are given in Table 4.2.

The fluid variables in the quasi steady-state are obtained from a constant gas distribution in the entire space divided into $N = 10$ volume elements. According to the analysis of the operational regimes given in Section 4.4, for constant gas fraction $\overline{\alpha_g} = 0.1$, the slip velocity is $v_s = 0.17$ m/s, the gas velocity is $\overline{v_g} = 0.155$ m/s, and the liquid velocity $\overline{v_l} = -0.017$ m/s. According to the signs of the velocities $\overline{v_g}$ and $\overline{v_l}$, the phases move in the opposite spatial direction which is illustrated in Figure 4.6(a).

For the given quasi steady-state situation, the eigenvalues are $\lambda_1 = 0.0954$ and $\lambda_2 = -0.064$, and they suggest the choice of the boundary conditions. According to

Table 4.2: Fluid properties and system parameters.

Symbol	Value	Unit
ρ_g	1	[kg/m^3]
ρ_l	1000	[kg/m^3]
C_d	0.440	[-]
d_b	0.001	[m]
C_p	1/4	[-]
g	9.81	[m/s^2]

(4.31), the analysis given in Section 4.3.2 for λ_1 the boundary condition has to be defined at the inlet, i.e., $W_1'(t,0)$, and the boundary condition for λ_2 has to be defined at the outlet, i.e., $W_2'(t,L)$. Figures 4.7 and 4.8 illustrate the wave propagation of the characteristic solutions from the boundaries without force term, i.e., the right-hand side of (4.28) equals zero,

$$\frac{\partial \mathbf{W}'}{\partial t} + \begin{bmatrix} 0.064 & 0 \\ 0 & -0.095 \end{bmatrix} \frac{\partial \mathbf{W}'}{\partial x} = \begin{bmatrix} 0 & 0 \\ 0 & 0 \end{bmatrix} \mathbf{W}'. \tag{4.36}$$

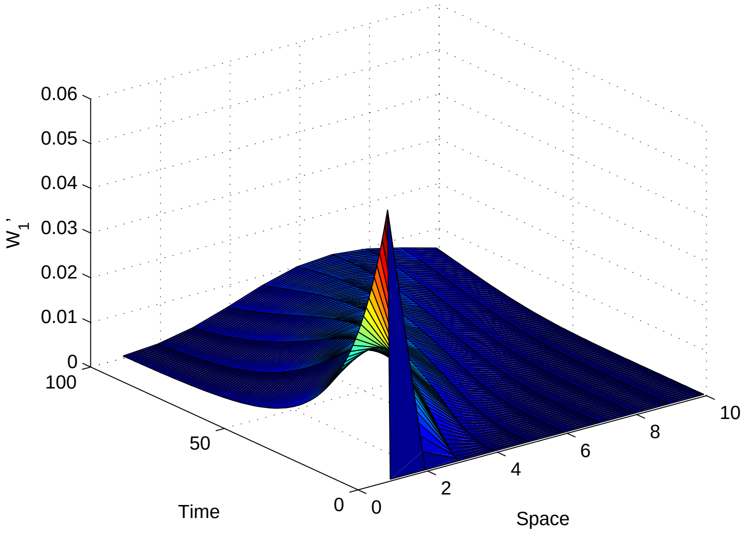

Figure 4.7: The wave propagation of $W_1'(t,x)$ with the speed λ_1 without the force term $c_{11}W_1' + c_{12}W_2'$.

The simulation results clearly show the direction of the wave propagation and the stability of the solutions $W_1'(t,x)$ and $W_2'(t,x)$, respectively. As shown, for the given boundary conditions the linearized model, which represent the perturbations around the chosen operational regime, without force term (i.e., only directional derivatives) is stable. This verifies the well-posedness of the boundary conditions which were obtained through the analysis of the eigenvalues $\lambda_1 = 0.0954$ and $\lambda_2 = -0.064$. Furthermore, Figures 4.7 and 4.8 show a typical behavior of the first order hyperbolic system [81].

Now, we will introduce the right-hand side of (4.28) to examine the influence of the linearized force vector. The influence of the linearized force vector, i.e., the right-hand side of (4.28) is calculated from

$$\frac{\partial \mathbf{W}'}{\partial t} + \begin{bmatrix} 0.064 & 0 \\ 0 & -0.095 \end{bmatrix} \frac{\partial \mathbf{W}'}{\partial x} = \begin{bmatrix} 521.26 & 1647.64 \\ -521.26 & -1647.64 \end{bmatrix} \mathbf{W}', \tag{4.37}$$

and presented in Figures 4.9 and 4.10.

For the wave that propagates from bottom to top, the effect of drag force is observed mostly at the top boundary caused by $c_{11}W_1'(t,x)$ and $c_{12}W_2'(t,x)$ with a minor oscillation with respect to space (Figure 4.9). The drag force has much stronger effect on the wave that propagates from top to bottom. Although the system is still stable, the wave velocities are rather influenced by the force coefficients c_{11}, c_{12}, c_{21}, and c_{22}. Since $c_{12} > c_{11} > 0$ and $c_{11} = -c_{21}$ whereas $c_{12} = -c_{22}$, the stability of the wave which

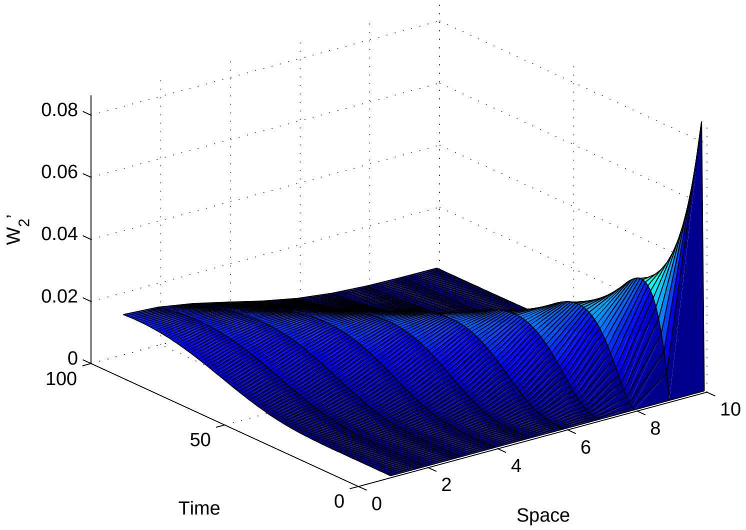

Figure 4.8: The wave propagation of $W_2'(t,x)$ with the speed λ_2 without the force term $c_{21}W_1' + c_{22}W_2'$.

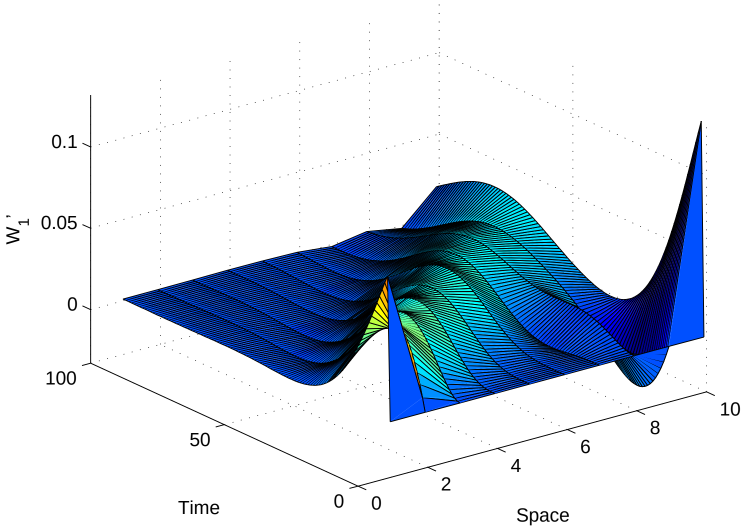

Figure 4.9: The wave propagation of $W_1'(t,x)$ *with the speed* λ_1 *forced by* $c_{11}W_1' + c_{12}W_2'$.

propagates with the velocity λ_2 is largely influenced by c_{22}.

The simulation results given in Figures 4.7, 4.8, 4.9, and 4.10 are given in the $\mathbf{W}'$ coordinates, which were obtained in Section 4.3.2. As discussed in Section 4.3.4, the original coordinate system Φ' can be recovered using the inverse transformation of the coordinate transformation matrix $\mathbf{T}$. To recover the original set of PDEs given as (4.8), we can use the following expression to, first, recover the coordinate system Ψ'

$$\mathbf{V}^{-1}\frac{\partial \Psi''}{\partial t} + (\mathbf{V}^{-1}\mathbf{A}_{\text{red}}\mathbf{V})\mathbf{V}^{-1}\frac{\partial \Psi''}{\partial x} = (\mathbf{V}^{-1}\mathbf{F}_{\text{red}}\mathbf{V})\mathbf{V}^{-1}\Psi'', \tag{4.38}$$

where the inverse transformation matrix $\mathbf{V}$ is

$$\mathbf{V}^{-1} = \begin{bmatrix} 44.6726 & 0.5 \\ -44.6726 & 0.5 \end{bmatrix},$$

and, after that, to recover the original PDE model using the transformation matrix $\mathbf{T}$.

The time evolution of the original linearized two-phase flow model (4.28) along the characteristic directions for the given eigenvalues can be obtained from the following equations

$$\text{for} \quad \lambda_1 = 0.064 \tag{4.39}$$

$$+44.6726\frac{d\alpha_g'}{dt} + 0.5\frac{d(\rho_g v_g' - \rho_l v_l')}{dt} = 2177.014\alpha_g' - 12.66(\rho_g v_g' - \rho_l v_l'),$$

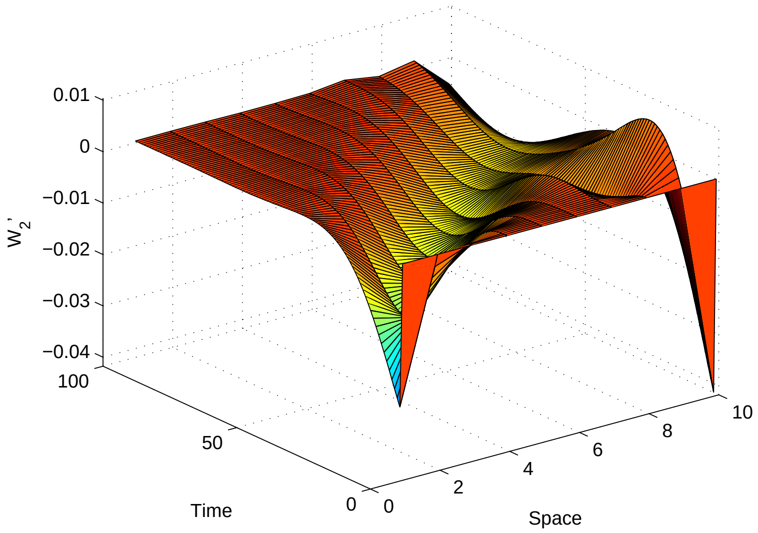

Figure 4.10: The wave propagation of $W_2'(t,x)$ *with the speed* λ_2 *forced by* $c_{21}W_1' + c_{22}W_2'$.

and

$$\text{for} \quad \lambda_2 = -0.095 \tag{4.40}$$
$$-44.6726\frac{d\alpha_g'}{dt} + 0.5\frac{d(\rho_g v_g' - \rho_l v_l')}{dt} = -2177.014\alpha_g' + 12.66(\rho_g v_g' - \rho_l v_l').$$

Equations (4.39) and (4.40) represent the time evolution in the original coordinate system Φ'. In this coordinate system, the influence of the drag force can be observed through the coefficients on the right-hand side of (4.39) and (4.40) for the eigenvalues λ_1 and λ_2, respectively. The coefficients have a strong influence on the system dynamics, which explains the system behavior illustrated in Figures 4.9 and 4.10. According to the signs of the coefficients, we can conclude that the drag and the gravitational force have a negative delay response regarding the impulse injection at the boundary. This explains the oscillation in the simulation results shown in Figures 4.9 and 4.10. The effect is much stronger on the wave that propagates from bottom to top compared to the wave that propagates from top to bottom.

4.6 Discussion

In this chapter, we derived a control-oriented 1D two-phase model that has several unique features which make this model very attractive for control design. Advantages of the derived two-phase flow model can be summarized as follows.

1. Physical aspects of the derived two-phase flow model:
    - The system of equations (4.8) for the two-phase flow have been obtained using mass and momentum balance equations of a purely hydrodynamical nature. The system is consistent in two ways. Firstly, all equations have been obtained by macroscopic observation of a large number of bubbles in a given volume, omitting the effects of individual bubbles. Secondly, it is assumed that the mixture is diluted and that the changes in the velocity at a given point is due to the motion of phases excluding the effect of the individual bubbles. These two assumptions allow us to simplify the complex set of equations for multiphase flow given in Section 2.2.3 as (2.10)-(2.11) to the control-oriented two-phase flow model given as (4.8). The list of assumptions used to derive the control-oriented model is given in Section 4.2.2.
    - The derived 1D two-phase model is well-posed, and it has a hyperbolic-like nature (see Chapter 2). The well-posedness of the boundary conditions is studied using the method of characteristics that utilizes only the system matrix to obtain well-posed boundary conditions. We have shown that the hyperbolic nature of the solution is a function of system matrices only, and any coupling term that is not a function of the directional derivatives will not influence the well-posedness of the model formulation.
    - The interfacial pressure difference for the liquid phase is found to be the most significant in determining the behavior of wave propagation of the two-phase flow and well-posedness of the model formulation. The interfacial pressure, which is introduced in order to guarantee the well-posedness, is described by the interfacial coefficient C_p. The interfacial coefficient remains an open flow parameter that can be used to describe different flow regimes. It can also overcome the problem of shared pressure effect which might be crucial for different pressure conditions [51]. The derived gas wave speed based on the eigenvalue analysis agrees well with the gas wave data of bubbly air/water flow [73].
    - Due to the presence of the two pressure terms (i.e., interfacial pressure and total pressure), the derived two-phase flow model is the two-pressure model of two-phase flow [80]. The two-pressure models are motivated by the fact that the single-pressure models of two-phase flow do not provide well-posed solutions. The ill-posed single-pressure model appears to result from an unrealistic assumption, called the “hydrostatic assumption” [80]. The hydrostatic assumption gives an unrealistic flow propagation speed in

  a dynamic flow situation. In general, models with a real and complex set of solutions are ill-posed, and any numerical scheme used to solve such a system will be unstable. In our formulation of the two-phase flow model, the interfacial pressure is considered in order to avoid ill-posed model formulation.

  - The key aspect of the derived two-phase fluid flow model given as (4.8) is the elimination of total pressure by subtracting (4.1) from (4.7). This allows analysis related to different control aspects without using CFD algorithms and complex gridding as presented in Chapter 3 for the single-phase flow.

2. Control perspectives of the derived two-phase flow model:

  - The numerical simulations of complex two-phase flow models can be largely simplified by the wave propagation analysis of processes described by the hyperbolic-like PDAE/PDE models. It also allows a complete algebraic evaluation of the solutions using an explicit formulation of the eigenvalue and its eigenvectors.
  - The decoupled model given as (4.28) in a new coordinate system has the same eigenvalues and dynamics as the original PDAE model given as (4.8) and can be directly used to determine the boundary conditions based on the signs of eigenvalues. This is an important aspect of the derived two-phase flow model since the eigenvalue analysis directly linked the system dynamics and boundary conditions.
  - Solutions to the problem of defining well-posed actuation strategies can be divided into two parts:
    (a) linearizing the model around a steady-state, i.e., quasi steady-state solution that casts the problem into the form that we can handle, and
    (b) applying different coordinate transformations in order to eliminate the remaining algebraic constraint equation of the derived PDAE model and to the decouple directional derivatives without applying any discretization scheme.
  - Using the linearized representation of a flow regime and wave propagation analysis, the two-phase flow can be brought into a control framework which is easy to implement on a real practical setup. Once the model structure is well-posed for dominant dynamics, the model can be redesigned following the same modeling framework.
  - Due to the model simplicity in the final compact form given as (4.28), the derived control-oriented two-phase flow model gives a new perspective from the control point of view. The spatial domain can be seen as the actuation domain where the inputs can be placed at the boundaries or at any point in space. This will be utilized in Chapter 6 to design different spatially distributed control strategies.

- The main difference between this new decomposed linearized two-phase flow model and the observation in classical fluid dynamic theory is that the new results offer a real equivalence between the global system behavior and the boundary conditions, not only in terms of initial-boundary value problems, but also in terms of causal input/output structures.
- Finally, the computational load is reduced tremendously (a few seconds) compared to the computational load of the CFD models, which makes the derived two-phase flow model attractive for control design.

In the next two chapters, we will demonstrate the use of the derived control-oriented two-phase flow model to build different spatially distributed designs.

Chapter 5

Causal Input/Output Structures in Linearized PDE Models

This chapter focuses on causal input/output structures of the linearized two-phase flow model presented in Chapter 4. The main contribution of this chapter is to interpret the effect of the coupling terms c_{11}, c_{12}, c_{21}, and c_{22} in (4.28) using functional relationships that connect the properties at the boundaries. To investigate the influence of those coefficients on the overall system behavior, the Laplace-space representation of the linearized two-phase flow model and causal input/output structures will be introduced. The results are illustrated using the same numerical example of the linearized two-phase flow model as given in Chapter 4.

5.1 Causality in PDE models

5.1.1 Input/Output Structures

In the model-based control approach to spatially distributed systems, it is crucial to have a causal input/output structure between actuators and sensors (see Section 2.4). In ODE systems causality comes almost naturally, whereas in PDE systems causality also involves the space, which makes the problem of defining input/output structures in PDE models more involved. Even when a PDE is approximated with a large number of ODEs, we may face a challenging problem which concerns the causality of large scale model and possible input/output strategies. The input/output structure shown in Figure 2.2 for the discretized PDE model indicates not only the number and position of actuators and sensors, it also indicates relationships between causes (inputs) and effects (outputs). Therefore, the causality of an input/output structure is a very important aspect in designing a controller for all systems. It is essential not only to develop a well-posed actuation strategy for PDE systems, as discussed in Chapter 4, but also to define causal input/output structures and functional relationships. Although the theoretical frameworks presented in Chapter 4 and in this chapter are developed for two-phase fluid flow systems, they can be easily extended to a large class of hyperbolic-like PDE systems.

The main focus of this chapter is to determine functional relationships that describe the behavior of a two-phase flow system through a causal input/output structure with a structure-preserving boundary actuation strategy. Section 5.2.1 will investigate causality of different input/output structures using the Laplace-space representation of (4.28). For ease of reference, we repeat (4.28) here

$$\frac{\partial}{\partial t}\begin{bmatrix} W_1' \\ W_2' \end{bmatrix} + \begin{bmatrix} \lambda_1 & 0 \\ 0 & \lambda_2 \end{bmatrix} \frac{\partial}{\partial x}\begin{bmatrix} W_1' \\ W_2' \end{bmatrix} = \begin{bmatrix} c_{11} & c_{12} \\ c_{21} & c_{22} \end{bmatrix}\begin{bmatrix} W_1' \\ W_2' \end{bmatrix}. \tag{5.1}$$

The Laplace-space representation of (5.1) will eventually lead to functional relationships between the chosen inputs and outputs including the coupling terms c_{11}, c_{12}, c_{21}, and c_{22}, i.e., the right-hand side of (5.1). As we discussed in Chapter 4, the boundary actuation strategy based on the method of characteristics considers only the directional derivatives of (5.1). The main advantage of the Laplace-space representation of the two-phase flow model compared to the spatially discretized model (4.31) is that it relies on a causal input/output structure described by functional relationships. Furthermore, the functional relationships are computationally rather attractive since they do not require complex discretization schemes (e.g., the staggered grid as described in Chapter 3 for the single-phase flow) and complex numerical algorithms to solve the PDE model (see Appendix A for the Navier-Stokes equations). Several properties of the functional relationships and the analysis presented in this chapter can play a crucial role in designing spatially distributed controllers, which will be discussed in Chapter 6.

5.1.2 Causality of the Two-Phase Flow Model

The boundary actuation strategies for the two-phase fluid flow described in Chapter 4 relate to the direction of the fluid flow at the boundaries. The boundary actuation strategies are based on the method of characteristics, i.e., the eigenvalues analysis of the linearized two-phase flow model (5.1). The concept of wave front propagation and possible placement of actuators and sensors at the boundaries based on the results presented in Section 4.3.2 is shown in Figure 5.1. As indicated in Figure 5.1(a) for co-current flow, two inputs $W_1'(t,0)$ and $W_2'(t,0)$ in (5.1) and their respective outputs $W_1'(t,L)$ and $W_2'(t,L)$ define a causal input/output structure for $\lambda_1 > 0$ and $\lambda_2 > 0$ according to the method of characteristics. If we impose different actuation strategies on the co-current flow, the system will be non-causal. In essence, a non-causal input/output structure forecasts a difference in inputs before it actually occurs. Therefore, the location of actuators and sensors should predict the system behavior at the chosen locations as illustrated in Figure 5.1. For example, placing the actuators behind sensors, i.e., at the position x_2 of the bubble column for the wave that propagates with $\lambda_2 > 0$ and $\lambda_2 > 0$ (see Figure 5.1(b)) which corresponds to the location x_2 at the characteristic curves (see Figure 5.1(a)), gives a non-causal input/output structure

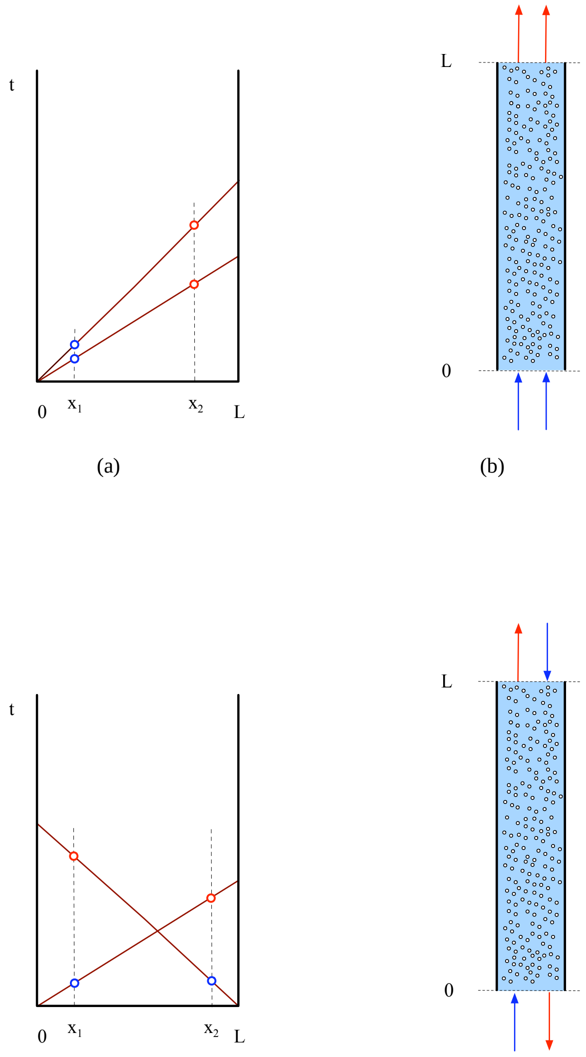

(a) (b)

(c) (d)

Figure 5.1: Causality of the input/output structures (a) for $\lambda_1 > 0$ *and* $\lambda_2 > 0$ *using the characteristic curves, (b) pertaining to the co-current flow in a bubble column, (c) for* $\lambda_1 > 0$ *and* $\lambda_2 < 0$ *using the characteristic curves, and (d) pertaining to the counter-current flow in a bubble column. The blue circles in (a) and (c), and blue arrows in (b) and (d) represent inputs while the red circles in (a) and (c), and red arrows in (b) and (d) represent the outputs.*

that cannot be used to describe system dynamics [74]. The same observation holds for the system with directional derivatives that are described by $\lambda_1 > 0$ and $\lambda_2 < 0$, i.e., the counter-current flow, as illustrated in Figures 5.1(c) and 5.1(d). For the counter-current flow, a causal input/output structure has to be defined by two inputs $W_1'(t,0)$ and $W_2'(t,L)$ and two outputs $W_1'(t,L)$ and $W_2'(t,0)$. However, the method of characteristics involves only directional derivatives, i.e., the eigenvalues λ_1 and λ_2, which is a sufficient condition in the case of small coefficients c_{11}, c_{12}, c_{21}, and c_{22}. The large magnitude of those coefficients can change the sign of the eigenvalues and consequently influence the established causality. This severely limits the causality analysis of the linearized two-phase flow systems for flow regimes that have large coefficients on the right-hand side of (5.1). In order to establish a causal input/output structure for a wide range of operational regimes, we will introduce the Laplace transformations of the linearized two-phase flow model (5.1). The Laplace domain allows the decomposition of the two-phase flow model into individual components connected through their inputs and outputs with rational transfer functions as relationships between the chosen inputs and outputs, including the eigenvalues λ_1 and λ_2 and the coefficients c_{11}, c_{12}, c_{21}, and c_{22}.

5.2 Functional Relationships

5.2.1 Laplace-Space Domain

In a control design, one of the first modeling concepts for causal systems is developed in the frequency domain using the Laplace transformations. As discussed in Section 5.1.1, the Laplace representation of PDE models can also be efficiently used to choose a causal input/output structure between quantities at the boundaries, i.e., any location in space. The concept of the Laplace transformation is to some extent similar to the Fourier transformation of the spatial derivatives, which is commonly used in CFD to approximate spatial variations of an infinite dimensional space[98].

Applying the Laplace transformation to the model (5.1) yields

$$s\begin{bmatrix} W_1'(s,x) \\ W_2'(s,x) \end{bmatrix} + \begin{bmatrix} \lambda_1 & 0 \\ 0 & \lambda_2 \end{bmatrix} \frac{\partial}{\partial x} \begin{bmatrix} W_1'(s,x) \\ W_2'(s,x) \end{bmatrix} = \begin{bmatrix} c_{11} & c_{12} \\ c_{21} & c_{22} \end{bmatrix} \begin{bmatrix} W_1'(s,x) \\ W_2'(s,x) \end{bmatrix}, \tag{5.2}$$

which can be reordered providing a set of ODEs parametrized by the Laplace varaible s in the space coordinate x

$$\frac{d}{dx}\begin{bmatrix} W_1'(s,x) \\ W_2'(s,x) \end{bmatrix} = \begin{bmatrix} \lambda_1 & 0 \\ 0 & \lambda_2 \end{bmatrix}^{-1} \left(\begin{bmatrix} c_{11} & c_{12} \\ c_{21} & c_{22} \end{bmatrix} - sI \right) \begin{bmatrix} W_1'(s,x) \\ W_2'(s,x) \end{bmatrix}. \tag{5.3}$$

The advantage of the Laplace-space representation of the two-phase flow model given by (5.3) is that it can be solved analytically by integrating (5.3) over the spatial domain. This means that the relationships between the inputs and outputs are given by transfer functions. The following relationship between the inputs and outputs defined at the bottom boundary $x = 0$ and at any location $x > 0$ can be obtained

$$\begin{bmatrix} W_1'(s,x) \\ W_2'(s,x) \end{bmatrix} = \exp\left(\mathcal{A}(s)x\right) \begin{bmatrix} W_1'(s,0) \\ W_2'(s,0) \end{bmatrix}, \tag{5.4}$$

with $\mathcal{A}(s)$ being the system matrix parametrized by s

$$\mathcal{A}(s) = \begin{bmatrix} \dfrac{c_{11}-s}{\lambda_1} & \dfrac{c_{12}}{\lambda_1} \\ \dfrac{c_{21}}{\lambda_2} & \dfrac{c_{22}-s}{\lambda_2} \end{bmatrix}. \tag{5.5}$$

Equation (5.4) directly connects the inputs and outputs, where the system dynamics are described by the system matrix $\mathcal{A}(s)$. A causal input/output structure for the system (5.4) can be determined by decoupling the system in the similar manner as it was presented in Chapter 4. In contrast to the decoupling presented in Section 4.3.4, decoupling of (5.4) includes the directional derivatives λ_1 and λ_2 and the coupling coefficients c_{11}, c_{12}, c_{21}, and c_{22}. The Laplace-space representation of the two-phase flow model allows us to examine the influence of the drag force on the boundary conditions and to define the causal input/output structures. The advantage of the decoupled system is that the system dynamics can be fully decoupled preserving the dynamics described by the eigenvalues of the system matrix $\mathcal{A}(s)$. The coordinates $\mathbf{W}'(s,x)$ can be transformed into the new coordinate system $\mathbf{Z}'(s,x)$ using the following general expression

$$\begin{bmatrix} Z_1'(s,x) \\ Z_2'(s,x) \end{bmatrix} = \mathbf{Q}(s) \begin{bmatrix} W_1'(s,x) \\ W_2'(s,x) \end{bmatrix}, \tag{5.6}$$

where $\mathbf{Q}(s)$ represents a transformation matrix which contains the eigenvectors corresponding to the eigenvalues of $\mathcal{A}(s)$ in the right order, i.e.,

$$\mathbf{Q}(s) = \begin{bmatrix} q_{11}(s) & q_{12}(s) \\ q_{21}(s) & q_{22}(s) \end{bmatrix},$$

with the following elements

$$\begin{aligned} q_{11}(s) &= 1, \qquad q_{12}(s) = \frac{1}{2c_{21}\lambda_1}\left(\lambda_2 c_{11} - \lambda_1 c_{22} + (\lambda_1-\lambda_2)s + \sqrt{\varepsilon(s)}\right), \\ q_{21}(s) &= 1, \qquad q_{22}(s) = -\frac{1}{2c_{21}\lambda_1}\left(-\lambda_2 c_{11} + \lambda_1 c_{22} - (\lambda_1-\lambda_2)s + \sqrt{\varepsilon(s)}\right). \end{aligned}$$

where

$$\varepsilon(s) = \left((\lambda_1-\lambda_2)s + (c_{11}\lambda_2 - \lambda_1 c_{22})\right)^2 + 4\lambda_1\lambda_2 c_{21}. \tag{5.7}$$

Note that the elements $q_{12}(s)$ and $q_{22}(s)$ are irrational functions since they are a function of $\sqrt{\varepsilon(s)}$. This will be further discussed in Section 5.3.2.

Using the coordinate transformation (5.6), the fully decoupled system in the new coordinate system $\mathbf{Z}'$ can be written as

$$\begin{bmatrix} Z_1'(s,x) \\ Z_2'(s,x) \end{bmatrix} = \begin{bmatrix} e^{\lambda_1^*(s)x} & 0 \\ 0 & e^{\lambda_2^*(s)x} \end{bmatrix} \begin{bmatrix} Z_1'(s,0) \\ Z_2'(s,0) \end{bmatrix}. \tag{5.8}$$

Table 5.1: Wave propagation and input/output structures based on the eigenvalue analysis in the Laplace-space domain in the $\mathbf{Z}'(s,x)$ *coordinate system.*

Case	Eigenvalues of the system parametrized by s	Inputs	Outputs
1	$\lambda_1^*(s) < 0$ $\lambda_2^*(s) < 0$	$\begin{bmatrix} Z_1'(s,0) \\ Z_2'(s,0) \end{bmatrix}$	$\begin{bmatrix} Z_1'(s,L) \\ Z_2'(s,L) \end{bmatrix}$
2	$\lambda_1^*(s) > 0$ $\lambda_2^*(s) < 0$	$\begin{bmatrix} Z_1'(s,L) \\ Z_2'(s,0) \end{bmatrix}$	$\begin{bmatrix} Z_1'(s,0) \\ Z_2'(s,L) \end{bmatrix}$
3	$\lambda_1^*(s) < 0$ $\lambda_2^*(s) > 0$	$\begin{bmatrix} Z_1'(s,0) \\ Z_2'(s,L) \end{bmatrix}$	$\begin{bmatrix} Z_1'(s,L) \\ Z_2'(s,0) \end{bmatrix}$
4	$\lambda_1^*(s) > 0$ $\lambda_2^*(s) > 0$	$\begin{bmatrix} Z_1'(s,L) \\ Z_2'(s,L) \end{bmatrix}$	$\begin{bmatrix} Z_1'(s,0) \\ Z_2'(s,0) \end{bmatrix}$

Then, the eigenvalues of $\mathcal{A}(s)$ can be obtained from the following expressions

$$\lambda_1^*(s) = \frac{1}{2}\frac{-(\lambda_1+\lambda_2)s+\lambda_1 c_{22}+\lambda_2 c_{11}+\sqrt{\varepsilon(s)}}{\lambda_1\lambda_2}, \tag{5.9}$$

$$\lambda_2^*(s) = \frac{1}{2}\frac{-(\lambda_1+\lambda_2)s+\lambda_1 c_{22}+\lambda_2 c_{11}-\sqrt{\varepsilon(s)}}{\lambda_1\lambda_2}. \tag{5.10}$$

The signs of the eigenvalues $\lambda_1^*(s)$ and $\lambda_2^*(s)$ determine the causality of the input/output structure for the linearized two-phase flow system. Note that $\lambda_1^*(s)$ and $\lambda_2^*(s)$ contain the eigenvalues λ_1 and λ_2 and the coefficients c_{11}, c_{12}, c_{21}, and c_{22}. Different input/output structures are possible according to the signs of $\lambda_1^*(s)$ and $\lambda_2^*(s)$. Table 5.1 outlines four different cases.

For example, suppose that $\lambda_1^*(s) < 0$ and $\lambda_2^*(s) < 0$ (case 1 in Table 5.1), then the inputs have to be defined at $x = 0$ and the outputs at $x = L$ as illustrated in Figure 5.2(a). Then, according to (5.8), the connections between the inputs $Z_1'(s,0)$ and $Z_2'(s,0)$ and the outputs $Z_1'(s,L)$ and $Z_2'(s,L)$ are defined by the delay functions $e^{\lambda_1^*(s)L}$ and $e^{\lambda_2^*(s)L}$, respectively, i.e.,

$$\begin{bmatrix} Z_1'(s,L) \\ Z_2'(s,L) \end{bmatrix} = \begin{bmatrix} e^{\lambda_1^*(s)L} & 0 \\ 0 & e^{\lambda_2^*(s)L} \end{bmatrix} \begin{bmatrix} Z_1'(s,0) \\ Z_2'(s,0) \end{bmatrix}. \tag{5.11}$$

Suppose now that $\lambda_1^*(s) > 0$ and $\lambda_2^*(s) < 0$ (case 2 in Table 5.1), then the first equation in (5.8) is the inverse of a time delay function which is not physically realizable. In terms of dynamics, (5.8) represents a non-causal relationship between inputs and

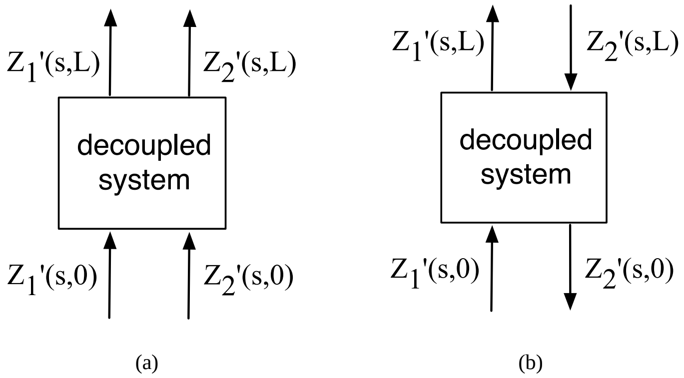

Figure 5.2: Input/output structures of the decoupled system in the $Z'(s,x)$ coordinate system, which has waves $\lambda_1^*(s)$ and $\lambda_2^*(s)$ that propagate (a) in the same direction and (b) in the opposite directions (also known as a bilaterally coupled system).

outputs. This means that the wave with $\lambda_1^*(s) > 0$ propagates in the spatial direction opposite to the predicted one, i.e., from top to bottom. By reordering (5.11), the system can be put into a causal input/output form that follows the direction of the wave propagation, i.e.,

$$\begin{bmatrix} Z_1'(s,0) \\ Z_2'(s,L) \end{bmatrix} = \begin{bmatrix} e^{-\lambda_1^*(s)L} & 0 \\ 0 & e^{\lambda_2^*(s)L} \end{bmatrix} \begin{bmatrix} Z_1'(s,L) \\ Z_2'(s,0) \end{bmatrix}. \tag{5.12}$$

This inversion of the relationship between the input $Z_1'(s,L)$ and the output $Z_1'(s,0)$ renders the set of equations (5.12) into a causal form. Figure 5.2(b) illustrates the inversion which implies that the resulting system is bilaterally coupled [74]. As illustrated in Figure 5.2, the causal input/output structures between the properties at the boundaries can be viewed as an extension of the system boundaries to their surroundings.

5.2.2 Laplace-Space Domain and Method of Characteristics

In Section 4.3.2, we used the method of characteristics to develop the well-posed boundary conditions based on the eigenvalue analysis of the pair ($\mathbf{A(\Phi)}$,$\mathbf{E}$). According to the eigenvalues λ_1 and λ_2, the well-posed boundary conditions were set based on the signs of the eigenvalues. For the numerical example given in Section 4.5, the top boundary was required for the wave that has the positive eigenvalue, whereas the bottom boundary was required for the wave that has the negative eigenvalue. The sign of λ_1 indicates the inversion of the boundary conditions that creates the well-posed boundary actuation strategy for the wave $W_1'(s,x)$. Basically, the method of characteristics presented in Section 4.3.2 used only the coefficients of directional derivatives, i.e., the eigenvalues λ_1 and λ_2, to indicate the well-posed boundary conditions without taking into account the coefficients c_{11}, c_{12}, c_{21}, and c_{22}. The influence of these coefficients was illustrated in Figures 4.9 and 4.10 for $W_1'(s,x)$ and $W_2'(s,x)$, respectively.

In order to derive more general requirements for setting well-posed boundary conditions, the coefficients have to be included in the analysis. These coefficients c_{11}, c_{12}, c_{21}, and c_{22} are included in the model representation given as (5.4). In the Laplace-space representation of the two-phase flow model (5.4), the coefficients c_{11}, c_{12}, c_{21}, and c_{22} appear in $\mathcal{A}(s)$, and together with the eigenvalues λ_1 and λ_2 give the input/output responses of the fluid properties at the boundaries. Since both methods are used to obtain boundary conditions to define a causal input/output structure, the input/output strategy in the time-space and the Laplace-space domain for $c_{11} = c_{12} = c_{21} = c_{22} = 0$ must agree.

Here, we will examine the causal input/output structure for counter-current flow defined by $\lambda_1 = 0.064$ and $\lambda_2 = -0.095$ given in Section 4.5. For $c_{11} = c_{12} = c_{21} = c_{22} = 0$, the eigenvalues in the Laplace-space domain read as

$$\lambda_1^*(s) = -\frac{s}{\lambda_1}, \quad \text{and} \quad \lambda_2^*(s) = \frac{s}{\lambda_2},$$

which gives

$$\begin{bmatrix} Z_1'(s,0) \\ Z_2'(s,L) \end{bmatrix} = \begin{bmatrix} e^{-\frac{s}{\lambda_1}L} & 0 \\ 0 & e^{\frac{s}{\lambda_2}L} \end{bmatrix} \begin{bmatrix} Z_1'(s,L) \\ Z_2'(s,0) \end{bmatrix}. \tag{5.13}$$

This means that the eigenvalue $\lambda_1 = 0.064$ requires an inversion in order to define a causal input/output structure. Equation (5.13) shows the same inversion between the inputs and the outputs as given in Section 4.3.2. This result verifies both theoretical frameworks. For analyzing the influence of the coefficients c_{11}, c_{12}, c_{21}, and c_{22} on input/output structures, the eigenvalues in the Laplace domain $\lambda_1^*(s)$ and $\lambda_2^*(s)$ change according to the expression (5.9) and (5.10), which will be evaluated in Section 5.3.2.

5.2.3 Coordinate Transformations

As already discussed in Chapter 4, a simple coordinate transformation allows us to transform a PDE model from one coordinate system to another by applying the inverse of the transformation matrix (see Section 4.3.4). However, a coordinate transformation for PDE models in the Laplace-space domain is a bit more involved. In this section, we will present two coordinate transformations for the two-phase flow model (5.4) for: the co-current flow illustrated in Figure 5.3(a) and the counter-current flow illustrated in Figure 5.3(b).

The coordinate transformation can be recovered using the following relationship

$$\begin{bmatrix} W_1'(s,x) \\ W_2'(s,x) \end{bmatrix} = \mathbf{Q}^{-1}(s) \begin{bmatrix} Z_1'(s,x) \\ Z_2'(s,x) \end{bmatrix}. \tag{5.14}$$

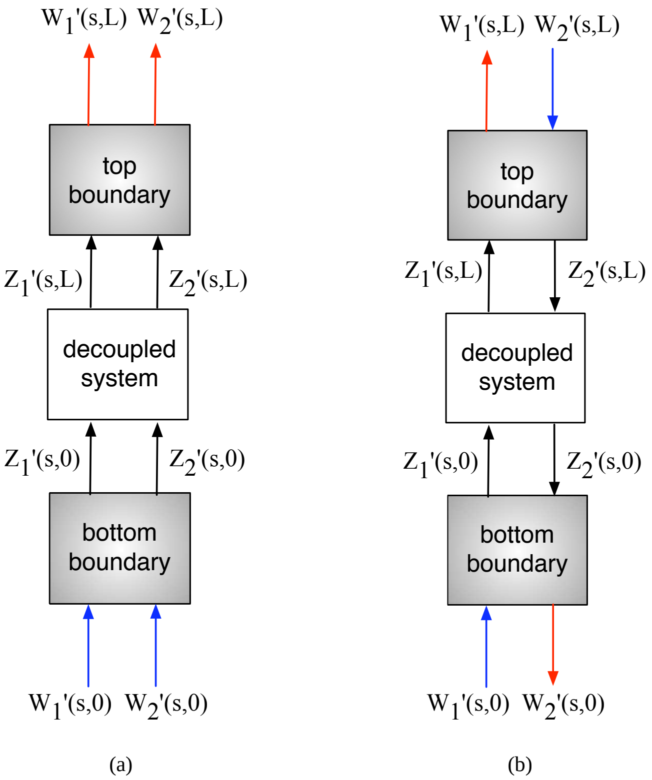

Figure 5.3: Input/output structures for (a) a co-current flow and (b) a counter-current flow. The blue arrows represent inputs, whereas the red arrows represent the outputs.

- **Co-current flow**

The following model representation in the $\mathbf{W}'(s,x)$ coordinates can be obtained on basis of the actuation strategy shown in Figure 5.3(a)

$$\begin{bmatrix} W_1'(s,L) \\ W_2'(s,L) \end{bmatrix} = \mathbf{G}_{\mathrm{co}}(s) \begin{bmatrix} W_1'(s,0) \\ W_2'(s,0) \end{bmatrix}, \tag{5.15}$$

where

$$\mathbf{G}_{\mathrm{co}}(s) = \mathbf{Q}^{-1}(s) \begin{bmatrix} e^{\lambda_1^*(s)x} & 0 \\ 0 & e^{\lambda_2^*(s)x} \end{bmatrix} \mathbf{Q}(s).$$

- **Counter-current flow**

  Figure 5.3(b) shows the way to recover the $\mathbf{W}'(s,x)$ coordinates for the counter-current flow. The bottom boundary can be recovered as

$$\begin{bmatrix} Z_1'(s,0) \\ W_2'(s,0) \end{bmatrix} = \begin{bmatrix} q_{11}(s) - \frac{q_{12}(s)q_{21}(s)}{q_{22}(s)} & \frac{q_{12}(s)}{q_{22}(s)} \\ -\frac{q_{21}(s)}{q_{22}(s)} & \frac{1}{q_{22}(s)} \end{bmatrix} \begin{bmatrix} W_1'(s,0) \\ Z_2'(s,0) \end{bmatrix}, \tag{5.16}$$

  whereas the top boundary can be recovered as

$$\begin{bmatrix} W_1'(s,L) \\ Z_2'(s,L) \end{bmatrix} = \begin{bmatrix} \frac{1}{q_{11}(s)} & -\frac{q_{12}(s)}{q_{11}(s)} \\ \frac{q_{21}(s)}{q_{11}(s)} & q_{22}(s) - \frac{q_{12}(s)q_{21}(s)}{q_{11}(s)} \end{bmatrix} \begin{bmatrix} Z_1'(s,L) \\ W_2'(s,L) \end{bmatrix}. \tag{5.17}$$

  Using the linear combination of the given boundaries (5.16) and (5.17), the original coordinates can be fully recovered as

$$\begin{bmatrix} W_1'(s,0) \\ W_2'(s,L) \end{bmatrix} = \mathbf{G}_{\mathrm{cc}}(s) \begin{bmatrix} W_1'(s,L) \\ W_2'(s,0) \end{bmatrix}, \tag{5.18}$$

  where

$$\mathbf{G}_{\mathrm{cc}}(s) = \begin{bmatrix} q_{11}(s) & -q_{12}(s)e^{-\lambda_1^*(s)} \\ q_{21}(s)e^{\lambda_2^*(s)} & -q_{22}(s) \end{bmatrix}^{-1} \begin{bmatrix} q_{11}e^{-\lambda_1^*(s)} & -q_{12}(s) \\ q_{21}(s) & -q_{22}(s)e^{\lambda_2^*(s)} \end{bmatrix}.$$

  Equation (5.18) represents a causal input/output structure between the properties at the boundaries, where the system dynamics are described by the elements of $\mathbf{G}_{\mathrm{cc}}(s)$.

The functional relationships (5.15) and (5.18) are algebraic representations of the two-phase flow model using the Laplace transformation. Due to the simple algebraic expressions $\mathbf{G}_{\mathrm{co}}(s)$ and $\mathbf{G}_{\mathrm{cc}}(s)$, the behavior of the system in the Laplace-space domain can be easily observed with a little computational effort. In general, a rational transfer function has many useful interpretations and features which are often associated with important system properties and control designs. This will be discussed in Chapter 6. The following section presents numerical methods needed to approximate the irrational transfer functions $\mathbf{G}_{\mathrm{co}}(s)$ and $\mathbf{G}_{\mathrm{cc}}(s)$ to a set of rational transfer functions.

5.3 Numerical Approximations in the Laplace-Space Domain

5.3.1 Numerical Methods

The numerical approximation of the Laplace-space representation of the two-phase flow model starts with a series expansion after which the Padé approximation of the irrational elements can be effectively used. The Padé approximations can take on many increasingly complicated forms, depending upon the degree of accuracy needed. The total approximation is based on a numerical approximation of an infinite series representation of a transportation delay by a rational polynomial fraction in which the coefficients and orders are defined by the required accuracy.

First, we start with the series functions computed as a truncated series expansion of $\lambda_i^*(s)$ with respect to the variable s as the series variable, i.e.,

$$\lambda_i^*(s) = h_{i,0} + h_{i,1}s + h_{i,2}s^2 + \cdots + h_{i,n}s^n, \tag{5.19}$$

where the index i denotes the wave characterized by either one or the other wave $i = 1,2$, with the polynomial coefficients $h_{i,0}$, $h_{i.1}$, $h_{i,2}$, $\ldots$, $h_{i,n}$. The first three polynomial coefficients for the numerical approximation of $\lambda_1^*(s)$ can be computed from the following expressions

$$
\begin{aligned}
h_{1,0} &= \frac{1}{2}\frac{\lambda_1 c_{22} + \lambda_2 c_{11} + \sqrt{(\lambda_1 c_{22} - \lambda_2 c_{11})^2 + 4\lambda_1\lambda_2 c_{21} c_{12}}}{\lambda_1\lambda_2}, \\
h_{1,1} &= -\frac{1}{2}\left(\left(\frac{1}{\lambda_2} + \frac{1}{\lambda_1}\right) + \frac{{\lambda_2}^2 c_{11} + {\lambda_1}^2 c_{22} - \lambda_2\lambda_1 c_{22} - \lambda_2 c_{11}\lambda_1}{\left((\lambda_2 c_{11} - \lambda_1 c_{22})^2 + 4\lambda_1\lambda_2 c_{21} c_{12}\right)^{1/2}}\right), \quad \text{and} \\
h_{1,2} &= \frac{c_{21} c_{12}\,(\lambda_2 - \lambda_1)^2}{\left((\lambda_2 c_{11} - \lambda_1 c_{22})^2 + 4\lambda_1\lambda_2 c_{21} c_{12}\right)^{3/2}},
\end{aligned}
$$

whereas for $\lambda_2^*(s)$, the coefficients read as

$$
\begin{aligned}
h_{2,0} &= -\frac{1}{2}\frac{-\lambda_1 c_{22} - \lambda_2 c_{11} + \sqrt{(\lambda_1 c_{22} - \lambda_2 c_{11})^2 + 4\lambda_1\lambda_2 c_{21} c_{12}}}{\lambda_1\lambda_2}, \\
h_{2,1} &= -\frac{1}{2}\left(\left(\frac{1}{\lambda_2} + \frac{1}{\lambda_1}\right) - \frac{{\lambda_2}^2 c_{11} + {\lambda_1}^2 c_{22} - \lambda_2\lambda_1 c_{22} - \lambda_2 c_{11}\lambda_1}{\left((\lambda_2 c_{11} - \lambda_1 c_{22})^2 + 4\lambda_1\lambda_2 c_{21} c_{12}\right)^{1/2}}\right), \quad \text{and} \\
h_{2,2} &= -\frac{c_{21} c_{12}\,(\lambda_2 - \lambda_1)^2}{\left((\lambda_2 c_{11} - \lambda_1 c_{22})^2 + 4\lambda_1\lambda_2 c_{21} c_{12}\right)^{3/2}}.
\end{aligned}
$$

The given coefficients are obtained using Maple Symbolic Toolbox. Since the symbolical representation is more complex for the higher order coefficients, we explicitly present here only the coefficients $h_{i,0}$, $h_{i,1}$, and $h_{i,2}$, and in Section 5.3.2, we will evaluate the influence of the higher order coefficients in (5.19) numerically.

Once the eigenvalues are approximated by the series (5.19), the exponential functions in (5.8) can be further approximated using the Padé approximations. The exponential functions, which represent the transportation delays characterized by the eigenvalues $\lambda_1^*(s)$ and $\lambda_2^*(s)$, can be approximated by rational transfer functions. One way to obtain an approximate model is to assume a model structure and match terms in the power series expansion of the approximation to that of the exact solution of the model, i.e.,

$$e^{\lambda_i^*(s)} = e^{h_{i,0}+h_{i,1}s+h_{i,2}s^2+\cdots+h_{i,n}s^n} = e^{h_{i,0}}e^{h_{i,1}s}e^{h_{i,2}s^2}\cdots e^{h_{i,n}s^n}. \tag{5.20}$$

Each of the terms in (5.20) represent matching of moments, which can be analyzed numerically using the Padé approximation [33]. The Padé approximation brings the system (5.8) into a form of the rational transfer function matrices $\mathbf{G}_{\mathrm{co}}(s)$ and $\mathbf{G}_{\mathrm{cc}}(s)$ for co-current flow and counter-current flow, respectively.

Applying the proposed numerical approximations brings a number of advantages for the spatially distributed control designs that will be discussed in Chapter 6. Before we introduce different spatially distributed control strategies, we will evaluate the Laplace-space representation of the two-phase flow model given in Section 5.2.1. In the next section, the Laplace-space representation of the two-phase flow model will be tested on the same numerical example as the one given in Section 4.5.

5.3.2 Numerical Example

The Laplace-space domain of the derived two-phase flow model according to (5.8) for the parameters given in Table 4.2 in Section 4.5 for counter-current flow reads as

$$\begin{bmatrix} W_1'(L) \\ W_2'(L) \end{bmatrix} = \exp\begin{bmatrix} 8144.7 - 15.62s & 25744.4 \\ 5486.9 & 17343.6 + 10.5s \end{bmatrix}\begin{bmatrix} W_1'(0) \\ W_2'(0) \end{bmatrix}, \tag{5.21}$$

with eigenvalues

$$\lambda_1^*(s) = 12744 - 2.549342105s - \sqrt{\varepsilon(s)} \tag{5.22}$$

$$\lambda_2^*(s) = 12744 - 2.549342105s + \sqrt{\varepsilon(s)}, \tag{5.23}$$

where

$$\varepsilon(s) = 0.00025^2(2.6\cdot 10^{15} + 1.9\cdot 10^{12}s + 2.7\cdot^{9} s^2)$$

The changes of s in the expressions for the eigenvalues $\lambda_1^*(s)$ and $\lambda_2^*(s)$ can have large or small influences on the overall system behavior. The irrational functions (5.22) and (5.23), which are generated by the matrix $\mathcal{A}(s)$, are parametrized by the Laplace varaible s that influences the magnitude of the eigenvalues. The influence of the Laplace varaible s on the eigenvalues $\lambda_1^*(s)$ and $\lambda_2^*(s)$ is shown in Figure 5.4 for both eigenvalues in the frequency domain.

The magnitude of $\lambda_2^*(s)$ is almost the same for the whole frequency range, whereas the magnitude of $\lambda_1^*(s)$ shows small changes for low frequencies. The phase shift between the eigenvalues is around 100 degrees, which in essence represents the dominant dynamics. In order to understand these findings and possible means of the complex eigenvalues, we use the numerical approximations given in Section 5.3 in order to obtain the rational transfer function $\mathbf{G}_{\mathrm{cc}}(s)$ and check the causality requirement.

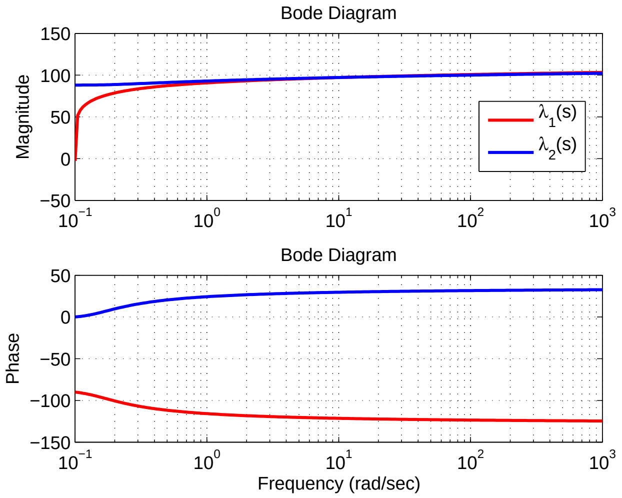

Figure 5.4: Bode diagram of the Padé approximation of the eigenvalues $\lambda_1^*(s)$ and $\lambda_2^*(s)$.

First, we start with the series expansion of the eigenvalues $\lambda_i^*(s)$ where $i = 1,2$. The values of the first seven coefficients in the series expansion, i.e, $h_{i,0}$, $h_{i,1}$,...,$h_{i,7}$, are

Table 5.2: Polynomial coefficients in the series expansion for the eigenvalues $\lambda_1^*(s)$ and $\lambda_2^*(s)$ given as 5.23 and 5.23, respectively.

	$\lambda_1^*(s)$	$\lambda_2^*(s)$
$h_{i,1}$	0	25488.32648
$h_{i,2}$	-7.268436753	2.169752
$h_{i,3}$	-0.00583416	-0.005841
$h_{i,4}$	0.0000021603	0.00000216035
$h_{i,5}$	$5.354 \cdot 10^{-10}$	$5.3544 \cdot 10^{-10}$
$h_{i,6}$	$-1.18 \cdot 10^{-12}$	$1.187 \cdot 10^{-12}$
$h_{i,7}$	$3.77 \cdot 10^{-16}$	$3.776 \cdot 10^{-16}$

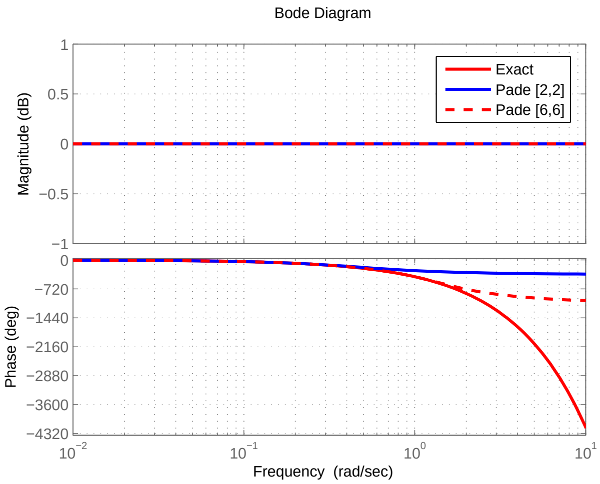

(a)

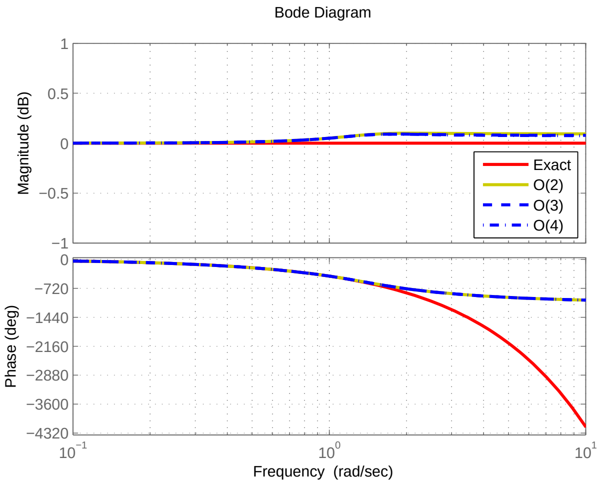

(b)

Figure 5.5: Frequency responses of the exact and approximate solutions of $e^{\lambda_i^*(s)}$ *using different (a) Padé approximations and (b) order of accuracy of the series expansion.*

given in Table 5.2. Figures 5.5 and 5.6 show the influence of the Padé approximation and the higher order terms in the series expansion on the accuracy of approximate solutions for both eigenvalues. As can be seen, the higher order terms have almost no influence on the magnitude of approximate solution and have a large influence on the

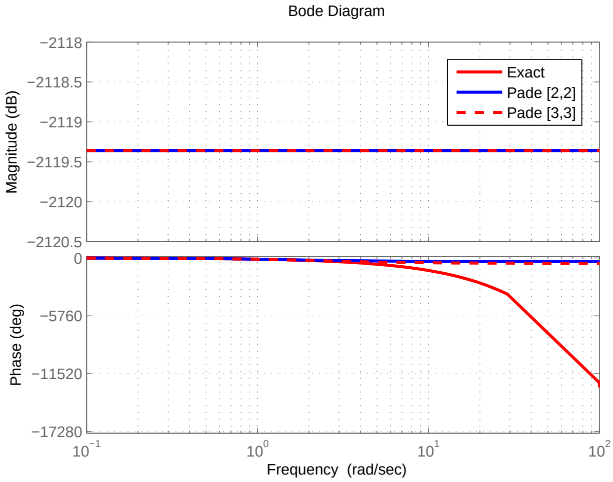

(a)

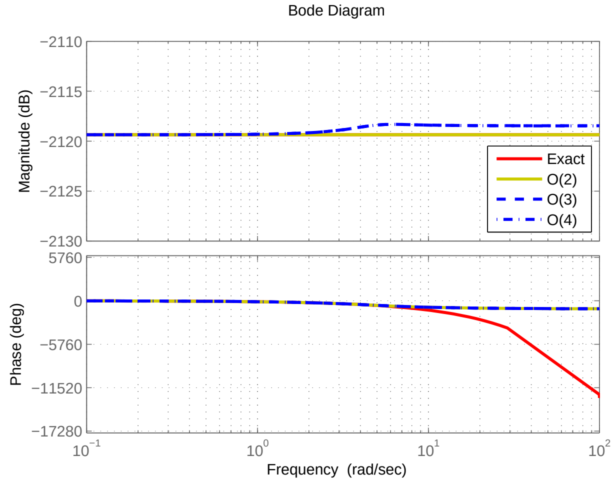

(b)

Figure 5.6: Frequency responses of the exact and approximate solutions of $e^{\lambda_i^*(s)}$ *using different (a) Padé approximations and (b) order of accuracy of the series expansion.*

phases for the high frequency range. Due to the fact that the waves represent pure delays of the flow betwen the boundaries, these results are to be expected. Using these findings, we can limit the approximate solutions of $e^{\lambda_i^*(s)}$ for both eigenvalues to $e^{h_{i,0}+h_{i,1}}$. This means that the delay function in the case of $\lambda_1^*(s)$ is $e^{-7.26s}$, and in the case of $\lambda_2^*(s)$ is $e^{-25488-2.1s}$ (see Table 5.2 for the coefficients). For $\lambda_2^*(s)$, the inversion of the boundary condition is imposed on the wave that propagates with $\lambda_2^*(s)$, i.e., $e^{-25488-2.1s}$ according to the theoretical framework presented in Section 5.2.1. The inversion gives the following causal input/output structure

$$\begin{bmatrix} Z_1'(s,L) \\ Z_2'(s,0) \end{bmatrix} = \begin{bmatrix} e^{-7.26sL} & 0 \\ 0 & e^{(-25488-2.1s)L} \end{bmatrix} \begin{bmatrix} Z_1'(s,0) \\ Z_2'(s,L) \end{bmatrix}. \tag{5.24}$$

The responses of the approximate solutions shown in Figures 5.5 and 5.6 are close to the exact solution for low frequencies, whereas for high frequencies the approximate solutions show a large error. This is to be expected since the pure delay functions are rarely known accurately. For a control design, it is often more important to understand the delays and system dynamics in order to choose a proper numerical approximation than to predict the delay functions accurately. To illustrate this, we create the following example.

Suppose that the following external dynamics are imposed at the boundaries

$$G = \frac{(s+3)}{(s^2+0.3s+1)}.$$

The cooresponding responses in the time domain are shown in Figure 5.7. Figures 5.7(a) and 5.7(b) show the step responces with different accuracies of the approximate solutions of the wave that propagates with speed $\lambda_1^*(s)$, whereas Figures 5.7(c) and 5.7(d) show the step responses of the wave that propagates with speed $\lambda_2^*(s)$. As shown, the higher order terms have no influence on the accuracy of $e^{\lambda_1^*(s)}$ and $e^{\lambda_2^*(s)}$.

Figure 5.7 shows different Padé approximations. The choice of the most appropriate Padé approximation is, generally, based on the desired accuracy and the convergence of the approximation. Here, a few Padé approximations with different accuracy are used (see Appendix D). First, we show in Figure 5.5 [2,2] and [6,6] Padé. As a general rule, we can say the higher the accuracy, the more exact solutions can be obtained. The effect of the higher order terms in the Padé are more visible in the time domain as illustrated in Figures 5.7(a) and 5.7(c). The approximation error of [2,2] for $e^{\lambda_1^*(s)}$ is rather large, while for $e^{\lambda_1^*(s)}$ it gives already a good approximation. To get a better approximation of $e^{\lambda_1^*(s)}$, the Padé [6,6] is introduced. The Padé [6,6] gives the solution close to the exact solution of $e^{\lambda_1^*(s)}$.

Furthermore, the wave with the speed $\lambda_1^*(s)$ represents the dominant system behavior since the magnitude of its change is much higher than the magnitude of the wave with the speed $\lambda_2^*(s)$. This can be also concluded from the approximation $e^{-25488-2.1s} = e^{-25488}e^{-2.1s} \approx 0 \cdot e^{-2.1s}$. The reason behind the small magnitude of $\lambda_2^*(s)$ lies in the effect of the coupling coefficients c_{11}, c_{12}, c_{21}, and c_{22}. These coefficients represent the effect of the drag force on the overall behavior. Basically, the drag force balances the transportation of the two-phase fluid flow, which dissipates through the boundaries. The dissipation of the two-phase fluid flow can have a positive or negative effect on the overall system behavior. As shown in Figure 5.7, the wave that propagates from bottom to top is slowed down by the other wave, which explains the small changes in

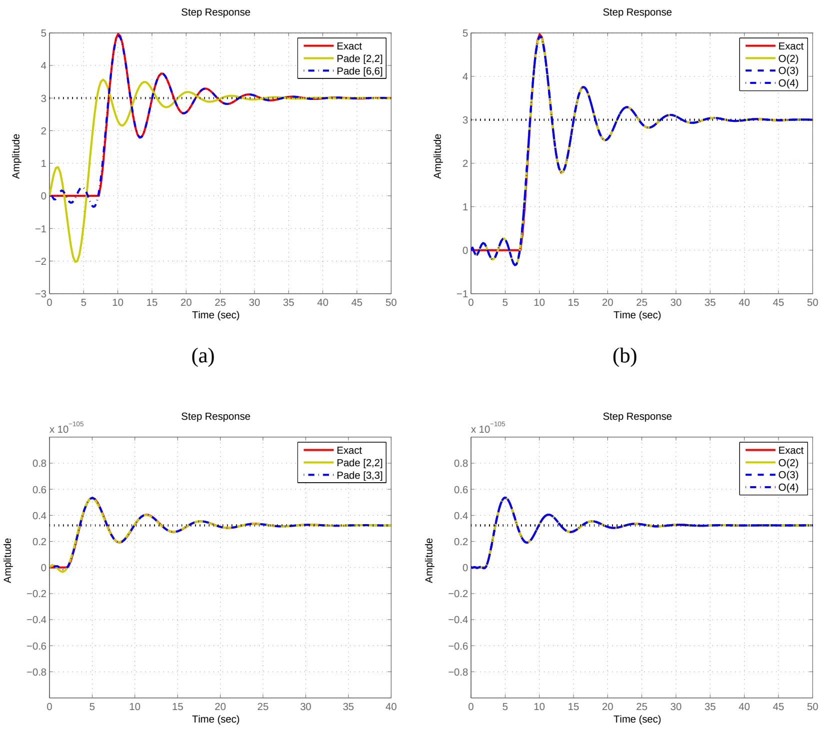

(a)

(b)

(c)

(d)

Figure 5.7: Step responses of the exact and approximate solutions to (5.24) with the external dynamics G of the wave that propagates with the speed (a) $\lambda_1^*(s)$ using [2,2] and [6,6] Padé, (b) $\lambda_1^*(s)$ with O(2), O(3), and O(4), (c) $\lambda_2^*(s)$ using [2,2] and [3,3] Padé, and (d) $\lambda_2^*(s)$ with O(2), O(3), and O(4).

the magnitude of the wave characterized by the speed $\lambda_2^*(s)$.

The simulation results presented in this sections are to be taken mainly qualitatively due to the fact that they illustrate the responses of the two-phase flow with the causal input/output structure in the Laplace-space domain by imposing the arbitrary dynamics *G* imposed on the boundaries. In the next chapter, the efficacy and benefits of the the Laplace-space representation of the two-phase flow will be explored quantitatively for stabilizing/destabilizing the two-phase flow system using different spatially distributed control designs.

5.4 Discussion

In this chapter, we introduced the concept of input/output causality for the linearized two-phase flow model using the Laplace-space representation of the model. The derived Laplace-space representation of the linearized two-phase flow model and the resulting functional relationships lead to the conditions for causal input/output structures for two-phase fluid flow.

From the numerical results presented in this chapter, the following conclusions can be drawn:

- Putting the decoupled system into a causal input/output structure strictly determines the placement of the actuators at the boundaries and this results in only one possible solution. This means that a well-posed actuation strategy has to be defined on the basis of the causality between the inputs and outputs as illustrated in Figure 5.1.

- The functional relationships between the properties at the boundaries (i.e., inputs and outputs) are fully described by the output delay functions where the eigenvalues $\lambda_1^*(s)$ and $\lambda_2^*(s)$ determine the magnitude of the delays and the signs of $\lambda_1^*(s)$ and $\lambda_2^*(s)$ determine the causal input/output structure. Such delay functions do not change the values of the quantity under consideration. The delay function, in principle, introduces a constant travel time from one boundary to the other.

- As illustrated in Figure 5.2, the boundary conditions and the delay functions of fluid flow are defined by a transformation from $\mathbf{Z}'(s,x)$ to $\mathbf{W}'(s,x)$. Although the coordinate transformation represents the system in two different state representations, it still describes exactly the same input/output behavior as the original model.

- Furthermore, the computational complexity associated with the CFD modeling can be greatly simplified by making use of theory associated with the rational transfer functions and the Padé approximations. The simulation time required for rational transfer functions in Matlab is just a few seconds. This is a huge advantage of the two-phase flow model in the Laplace-space domain.

The analysis presented in this chapter establishes a modeling framework of two-phase fluid flow systems (i.e., input/output relationships of a system) and proposes a new approach to influencing the fluid flow without using the CFD models. The main advantage of this approach is that it guarantees the causality of the input/output structures for a wide range of operating regimes, and provides insights needed for control designs. Furthermore, the Laplace-space representation of the two-phase flow systems does not rely on the accuracy of the spatial discretization nor on complicated numerical schemes. Instead, it gives functional relationships between inputs and outputs. The derived rational transfer functions, which describe the behavior of the two-phase fluid system at the boundaries, put the flow control into a new perspective for spatially distributed control designs. The spatially distributed designs will be introduced in the next chapter.

Chapter 6

Distributed Control Designs

All the modeling perspectives of fluid flow systems introduced in the previous chapters have served to provide the control-oriented models of fluid systems. In Chapter 3, the macroscopic model of single-phase flow was introduced for designing a boundary feedback controller, whereas in Chapter 4 great attention was given to the development of the control-oriented two-phase flow model. In this chapter, we will show how to design spatially distributed controllers for the derived control-oriented two-phase flow model. The numerical results for the boundary and centralized controller will be given in order to illustrate the advantages of applying the spatially distributed control designs. The spatially distributed control designs presented in this chapter can easily be extended to a wide range of hyperbolic-like PDE models.

6.1 Introduction

As discussed in the previous chapters, the most important feature of the microscopic modeling approach to the hydrodynamics is that it offers a wide range of possibilities to influence the hydrodynamics using spatially distributed causal input/output structures (see Section 2.4). In this chapter, we consider the problem of designing spatially distributed controllers for the two-phase flow model derived in Chapter 4 with the causal input/output structure defined in Chapter 5. Although the control laws will be given for the Laplace-space representation of the model (5.4) for a better illustration of possible spatially distributed control designs, in this chapter, we will use the spatially discretized model (4.31) as given in Figure 4.6 [91].

The aim of this chapter is to give an overview of possible spatially distributed control designs that can be used to control the two-phase flow system and to deliver a theoretical framework accomplishing the primary objective of this thesis. The chapter is organized as follows. In Section 6.2.3, we will present different spatially distributed control designs that can be imposed on the bubble column (see Section 1.3.2). The choice of the spatially distributed control designs depends on the problem formulation and desired process performances, which can be motivated by a particular application of the bubble columns. Different control objectives will be presented in Section 6.2.2, and in Section 6.2.3 mathematical descriptions of two types of spatially distributed controllers will be given. Section 6.3 will present numerical results for both controllers: boundary and centralized.

6.2 Control of Two-Phase Flow Systems

6.2.1 Spatially Discretized Two-Phase Flow Model

As we discussed in Chapter 4, the linearized two-phase flow model was obtained from the control-oriented two-phase flow model which was linearized around the quasi steady-state regime. In order to define a causal input/output structure, the linearized model was decoupled in the Laplace-space domain (5.8). The Laplace representation of the PDE model makes the two-phase flow model very attractive for various spatially distributed control designs due to the simplicity of the functional relationships and a very short computation time.

The spatially discretized two-phase flow model can be obtained by dividing the total volume of a bubble column into N volume elements with the system boundary around each element. These volume elements have the same volume $\triangle V$, which was illustrated in Figure 4.6. According to the theoretical framework given in Chapter 5, the interconnection between the volume elements $\triangle V$ (i.e., compartments) must be causal. The causality follows from the direction of wave propagation. Since the two-phase flow model belongs to a class of PDAE models, we distinguish two sets of variables: *explicit system variables* and *implicit system variables*. The explicit system variables are the flow rates of gas phase $v_{g,i}$ and the liquid phase $v_{l,i}$, as well as the volume fraction of the gas phase $\alpha_{g,i}$ and the liquid phase $\alpha_{l,i}$ in each compartment i. The implicit variable is the pressure which appears between the elements, i.e., on locations $i-\frac{1}{2}$ and $i+\frac{1}{2}$ (see Figure 4.6) and the interfacial pressure which appears between the phases in each element.

Before we introduce different spatially distributed control designs for the spatially discretized two-phase flow model, we will give an overview of different control goals that are relevant for the bubble column design.

6.2.2 Control Goals

There is a wide range of possible control objectives for the system described in Section 1.3.2. The control objective mainly depends on the practical application. In this section, we will outline some of the control objectives concerning the application of two-phase flow as discussed in Section 1.3.2.

The main control objectives concerning the two-phase flow that appears in the bubble columns are:

- stabilization of flow around an equilibrium (i.e., suppressing fluctuations caused by disturbances or secondary flow),

- destabilization of flow (i.e., enhancement of turbulence and intensification of fluid mixing), and
- endorsing of fluid separation (i.e., extraction of phases).

These control objectives cannot be achieved by a unique input/output strategy and control design. Instead, a wide range of control designs is needed in order to achieve the above given control objectives. For instance, enhancement of mixing of phases inside a bubble column can be easily obtained by introducing more valves on the side wall and using a more powerful pump/compressor equipment (see Figure 6.1(a)). On the other hand, for a laminar flow regime which is characterized by less drag force between the phases, the flow can be stabilized around the laminar flow applying a controller at the boundaries only (see Figure 6.1(b)). Therefore, it is important to outline all possible spatially distributed control designs.

6.2.3 Distributed Control Designs

In this section, we will investigate four different types of spatially distributed control designs and discuss the implementation of such controllers (see Figures 6.1(a), 6.1(b), 6.2(a), and 6.2(b)).

The design presented in Figure 6.1(a) is known as a boundary control design which is commonly used to stabilize the flow between the boundaries [12, 34, 60]. The design is based on a feedback control of the flow from one boundary to another. The controllers K_{12} and K_{21} in the feedback loops represent the control parameters that can influence the fluid properties from one boundary to another. The controllers K_{11} and K_{22} can be additionally added at the boundaries to improve the closed-loop process performance, and can be regarded as a set of valves that regulates the amount of gas phase injected to the column. This type of spatially distributed controller is common for a system governed by hyperbolic PDEs which describes a pure wave propagation from one boundary to another. The key point in this control design is that the fluid properties at the boundaries $x = 0$ and $x = L$ are used as control actions to regulate the flow. This design can be effectively used to stabilize the flow around an operational regime as described in Section 4.4. In general, the boundary controller has a goal to minimize the fluctuation of the flow inside the column and shorten the residence time of the fluctuations. This will be further discussed in Section 6.3.

In contrast to the boundary control design, the centralized control designs illustrated in Figures 6.1(b) allow the actuation and sensing from the side walls at each volume element. In practice, this means that we have to decide where to place the valves (i.e., inputs) and where to place the flow-meter (i.e., outputs) along the side wall. The centralized approach is the simplest spatially distributed design in terms of its derivation and implementation. As indicated in Figure 6.1(b), the implementation of this approach is straightforward since it requires a secondary flow that is connected to the bubble column. This type of experimental realization was recommended in [27] for the single-phase flow.

Depending on the communication between controllers K_i in each volume element, we can distinguish two different distributed designs: fully decentralized controller (see

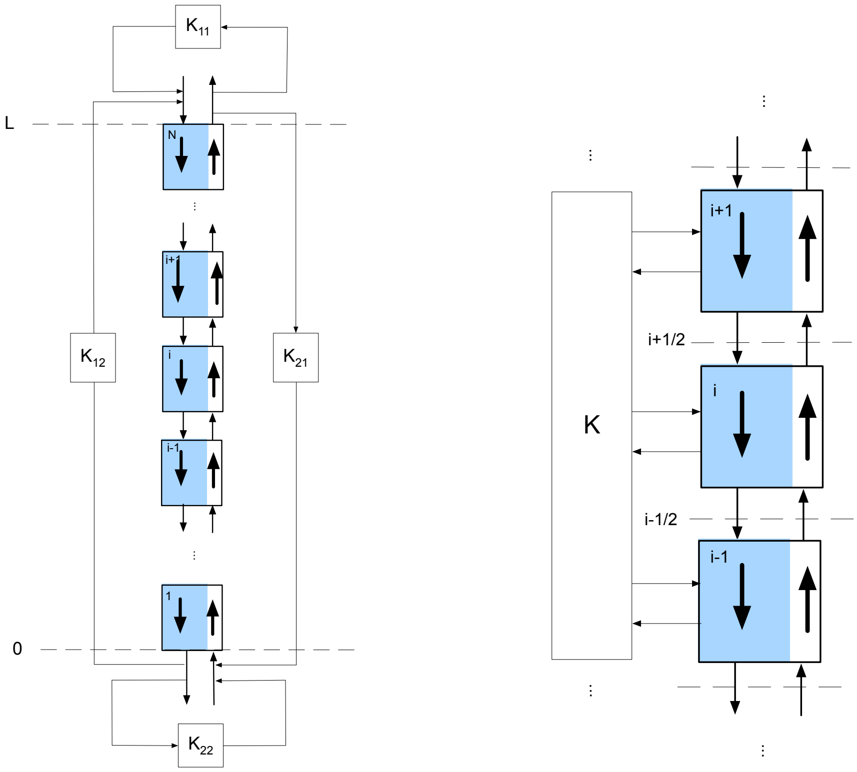

(a) (b)

Figure 6.1: Control strategies for the spatially discretized two-phase flow model using (a) boundary controller and (b) centralized controller.

Figure 6.2(a)) and distributed controller, i.e., localized (see Figure 6.2(b)). In fully decentralized strategies, the control parameter K_i uses only information from the i-th compartment, and there is no communication between the controllers from the neighboring compartments K_{i+1} and K_{i-1}. This approach usually results in the best performance, but it requires excessive communication [14, 76].

Another localized control strategy is the distributed controller shown in Figure 6.2(b). The aim of this spatially distributed control design is to provide a good performance by using communication capability of the flow between the controllers K_{i+1}, K_i, and K_{i-1}. In this way a smooth transient flow between the waves is possible. In contrats to the decentralized control strategy, here the controllers are interconnected in the same manner as the volume elements. For the bubble column, this means that there is a valve for injection of a secondary flow or suction of the primary flow inside the column in each volume element. The controllers K_{i-1}, K_i, K_{i+1} can act independently and exchange the information between each other. This control design requires mas-

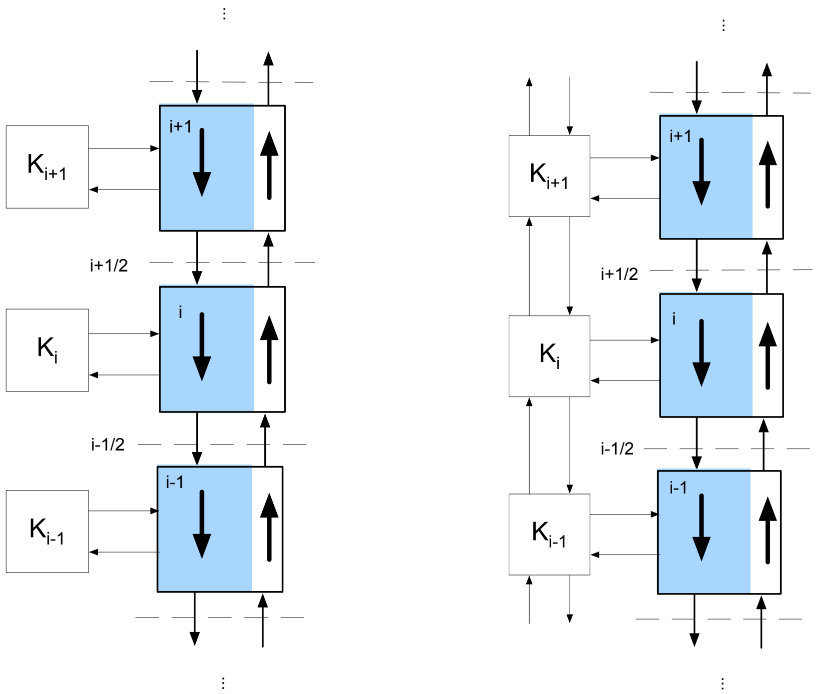

(a) (b)

Figure 6.2: Control strategies for the spatially discretized two-phase flow model based on (a) a fully decentralized controller, (b) a distributed controller (i.e., a localized controller).

sive arrays of actuators and sensors that is rather difficult to implement. This can be considered a drawback of the distributed control design when applying the distributed controller in practice. Thus, the designs presented in Figure 6.2 will be beyond the scope of this thesis.

6.2.4 Control Laws in the Laplace-Space Domain

Taking advantage of the system causality and the spatially distributed control designs presented in Section 6.2.3, we derive the following control laws for the designs shown in Figure 6.1:

1. **Boundary controller design**
   The boundary control law can be derived for the Laplace-space model representation of the two-phase flow
   $$\frac{d}{dx}\begin{bmatrix} W_1'(s,x) \\ W_2'(s,x) \end{bmatrix} = \mathcal{A}(s)\begin{bmatrix} W_1'(s,x) \\ W_2'(s,x) \end{bmatrix}, \tag{6.1}$$
   using the following conditions
   $$W_1'(s,0) = K_{12}W_1'(s,L), \tag{6.2}$$
   $$W_2'(s,L) = K_{21}W_2'(s,0), \tag{6.3}$$
   where the controllers K_{12} and K_{21} are placed at location $x = 0$ and $x = L$, respectively. The controllers connect the flow between the phases at the opposite boundaries. This design represents a boundary feedback control design. According to the design shown in Figure 6.1(a), a more general formulation of the boundary control law for the two-phase flow can be given taking into account the additional controllers K_{11} and K_{22}
   $$\begin{bmatrix} W_1'(s,0) \\ W_2'(s,L) \end{bmatrix} = \begin{bmatrix} K_{11} & K_{12} \\ K_{21} & K_{22} \end{bmatrix}\begin{bmatrix} W_1'(s,L) \\ W_2'(s,0) \end{bmatrix}. \tag{6.4}$$
   Numerical results of the boundary control of the two-phase flow model are given in Section 6.3, and final concluding remarks are made in Section 6.4.

2. **Centralized controller design**
   The centralized controller for the system given as (5.4) and illustrated in Figure 6.1(b) can be described by the following expression
   $$\frac{d}{dx}\begin{bmatrix} W_1'(s,x) \\ W_2'(s,x) \end{bmatrix} = \mathcal{A}(s)\begin{bmatrix} W_1'(s,x) \\ W_2'(s,x) \end{bmatrix} + \mathbf{B}(x)U(s), \tag{6.5}$$
   where $U(s)$ is the input vector and $\mathbf{B}(x)$ is the spatially distributed input matrix given in the Laplace-space domain that satisfies the following feedback control law
   $$U(s) = -K(s)\begin{bmatrix} W_1'(s,x) \\ W_2'(s,x) \end{bmatrix}. \tag{6.6}$$
   According to (6.5), the controller directly influences the dynamics of the uncontrolled flow by shaping the transfer functions defined by (5.15) for co-current flow, i.e., (5.18) for counter-current flow.

In the next section, we will give simulation results of the presented designs using the Laplace-space representation of the two-phase flow model. We will first present the feedback control designs for the system without the coupling terms $c_{11} = c_{12} = c_{21} = c_{22} = 0$. After that, we will introduce the coupling terms $c_{11} \neq c_{12} \neq c_{21} \neq c_{22} \neq 0$. Both spatially distributed control designs presented in this section will be considered as numerical examples using the same numerical example of the two-phase flow as given in Chapters 4 and 5.

6.3 Numerical Results

Example 1: Boundary controller

Following the boundary control design illustrated in Figure 6.1(a) and described by (6.1), the simulation results for the proposed boundary control of the two-phase flow are illustrated in Figures 6.3 for the two-phase flow without the coupling terms, i.e., $c_{11} = c_{12} = c_{21} = c_{22} = 0$, and in Figure 6.5 for the two-phase flow with the coupling terms $c_{11} \neq c_{12} \neq c_{21} \neq c_{22} \neq 0$. In essence, the coupling terms represent the effect of the drag force on the two-phase flow.

Figure 6.3 shows the effect of the control coefficient K_{21} on stabilizing the fluid flow in contrast to the uncontrolled flow. The control coefficient K_{21} from the top boundary to the bottom boundary is tuned based on the expected performance. The values for the proportional action K_{21}^P and the integral action K_{21}^I are given in Table 6.1. As can be seen, the controller K_{21} influences the internal delay of the flow between the properties at the bottom and top boundaries. The oscillations of the flow should be as small as possible in order to keep the flow close to the plug flow regime. Furthermore, the plug flow regime that is created in this way has the shortest travel time of the two-phase flow from one boundary to the other. This means that the control objective is to place the eigenvalues $\lambda_1^*(s)$ and $\lambda_2^*(s)$ closer to zero. The zero eigenvalues represent the flow without the delays $e^{\lambda_1^*(s)}$ and $e^{-\lambda_2^*(s)}$ of the two-phase flow between the boundaries.

Figure 6.3 shows the simulation results obtained for different values of the control coefficient K_{21}^P for the wave that propagates with the speed $\lambda_1^*(s)$. The value of the coefficients K_{21}^P and K_{21}^I are tuned until there is no oscillation of the two-phase flow close to the top boundary. The flow is almost totally damped out for the wave that propagates with the speed $\lambda_1^*(s)$. The similar results can be expected for the wave that propagates in the opposite direction with the speed $\lambda_2^*(s)$.

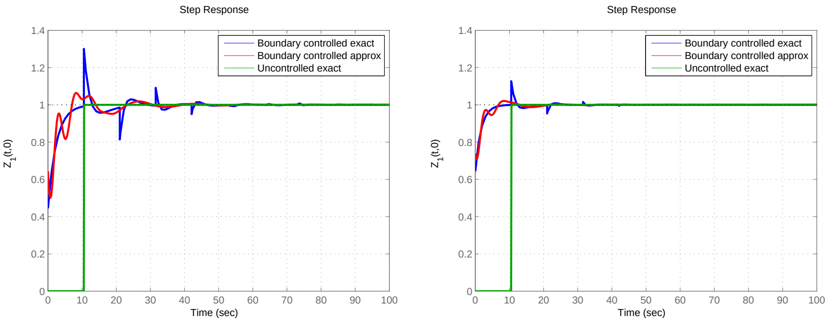

(a) (b)

Figure 6.3: Step responses of the boundary feedback controlled system illustrated in Figure 6.1(a) (a) with the proportional gain $K^P = 0.8$ *and (b) with the proportional gain* $K^P = 1.8$.

Table 6.1: Control coefficients for the control design shown in Figure 6.1(a) and given by (6.1).

Eigenvalues	K_{21}^{P}	K_{21}^{I}
$\lambda_1^*(s)$	0.8	0.1840
$\lambda_2^*(s)$	1.8	0.012

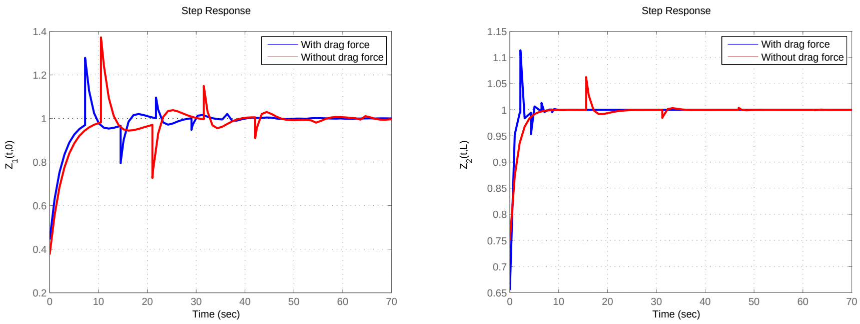

(a) (b)

Figure 6.4: Step responses of the controlled system with and without the drag force for the wave that propagates (a) from the bottom and (b) from the top of the bubble column.

In order to evaluate the effectiveness of the boundary controller on the two-phase flow, we show the simulation results of the controlled two-phase flow with and without the drag force. Figure 6.4 illustrates the controlled two-phase flow for the both waves with and without the drag force. When comparing the deviations of the waves in Figure 6.4, it is clear that the drag force has a shifting effect on the controlled flow and the flow arise earlier in time, but it still follows the same dynamics as the pure flow without the drag force. As can be seen, the proposed boundary controller minimizes the effect of the drag force almost completely.

The results are also illustrated in the frequency domain as shown in Figure 6.5. In some cases, the time and frequency responses of the delay functions can look odd in the Bode diagrams. The Bode diagrams of the delay functions are not software or numerical errors, but very often real features of such systems that can be validated comparing the approximated and exact results.

Example 2: Centralized controller

Figure 6.6 shows the simulation results obtained by applying the centralized controller on the two-phase flow model without the drag force. The simulations results given here

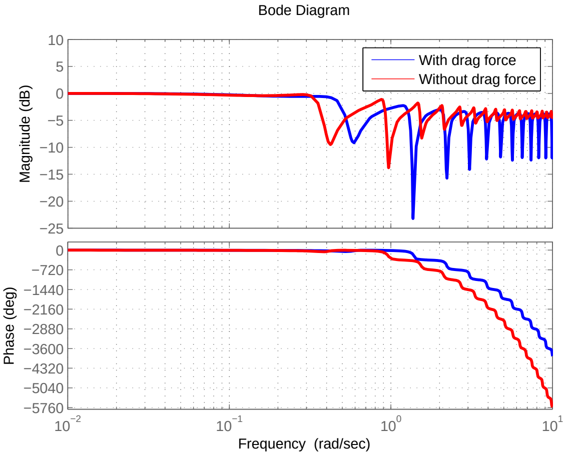

Figure 6.5: Frequency responses of the decoupled system for the wave that propagates with the speed $\lambda_1^*(s)$ *(i.e., with the drag force) and* λ_1 *(i.e., without the drag force) according to (5.12).*

evaluate the exact and approximated solutions of the controlled and uncontrolled flow in the Laplace-space domain, which was also discussed in Chapter 5.

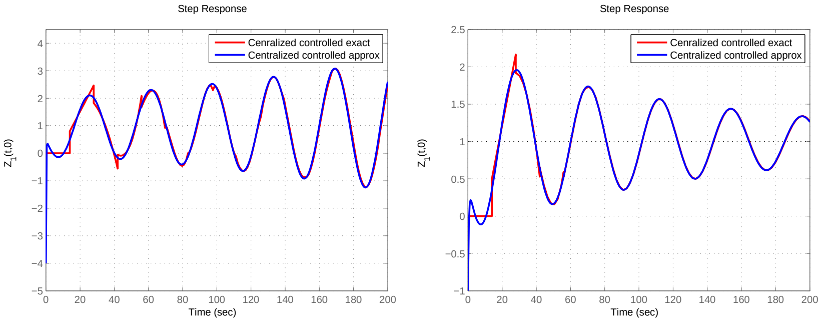

(a) (b)

Figure 6.6: Step responses of the boundary feedback controlled system with the centralized controller (a) with the proportional gain $K^P = 0.8$ *and (b) with the proportional gain* $K^P = 0.5$*.*

The approximate solutions are obtained using the series expansion and the Padé approximations as discussed in Chapter 5. The exact solution is in good agreement with the approximate solution, which is illustrated in the frequency domain in Figure

6.9.

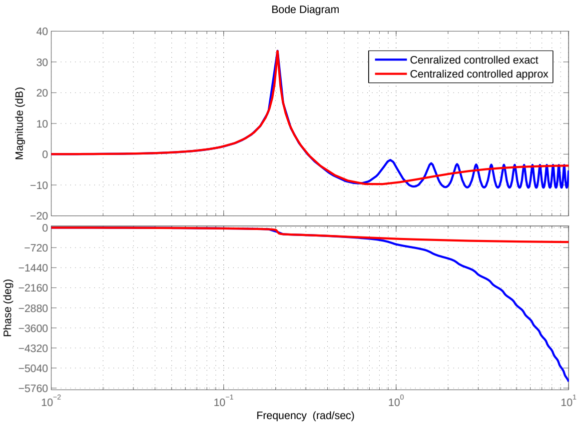

Figure 6.7: Frequency responses of the exact and approximated solutions of the wave that propagates with the speed $\lambda_1^*(s)$.

As expected, the controlled flow shown in Figure 6.8 oscillates around the unity input due to the simultaneous injection of the secondary flow at each location, i.e., compartment. The control parameter $K(s)$ in (6.6) is tuned in such a way to enhance the oscillations of the flow around the unity input. Basically, the highly oscillated controlled flow represents the highest possible mixing of the injected flow into the primary uncontrolled flow. Note that the control parameters are added to the open-loop dynamics as given in (6.5). Using the side-wall injection, we can influence the drag force manipulating the two-phase flow in the entire space and enhancing the mixing in the entire volume.

Figure 6.9 depicts the step response of the linearized two-phase flow model. For the proportional gain $K(s)^P = 0.1$, the controlled flow is marginally stable. For the proportional gain $K(s)^P > 0.1$ the closed-loop becomes unstable because the amplitude of the oscillations increases (see Figure 6.6(a)), whereas for the proportional gain $K^P < 0.1$, the oscillations fade out. The discrepancies occur at the high frequencies and at the small gain, which is why they are not clearly visible in the step response given in Figure 6.8. This corresponds to the fact that a lower order Padé approximation of the delay function influences accuracy of the approximation. The oscillations induce the degree of the chosen polynomial given in numerator and does not provide any physical explanations.

Although the given analysis of the two-phase flow without the drag force does not have a real physical meaning, it has a major contribution in understanding the two-phase flow system. Figures 6.10 and 6.9 incorporate the design in one single figure in the time domain and in the frequency domain, respectively. As shown, the wave that propagates from bottom to top can oscillate largely with respect to the step input,

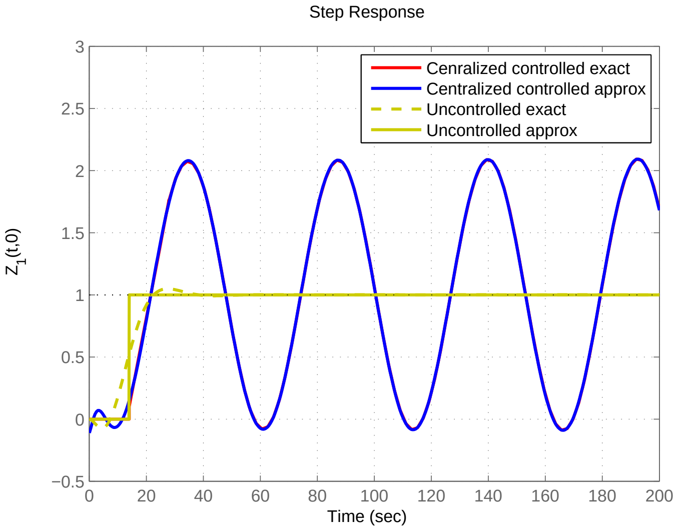

Figure 6.8: *Step responses of the boundary feedback controlled system with the centralized controller without the drag force.*

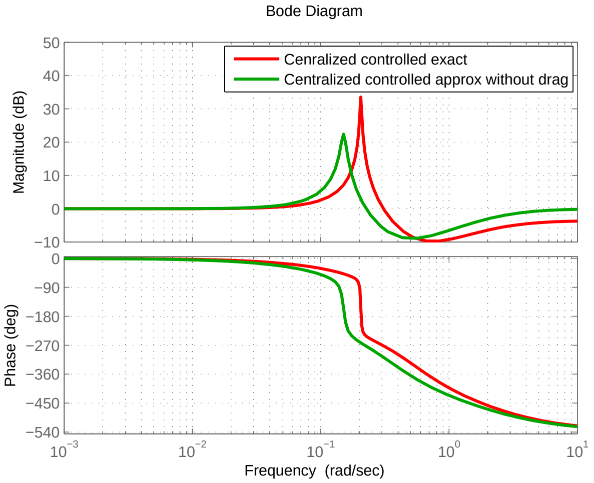

Figure 6.9: *Frequency responses of the decoupled system for the wave propagation defined by* $\lambda_1^*(s)$ *(i.e., with the drag force) and* λ_1 *(i.e., without the drag force) according to (5.12).*

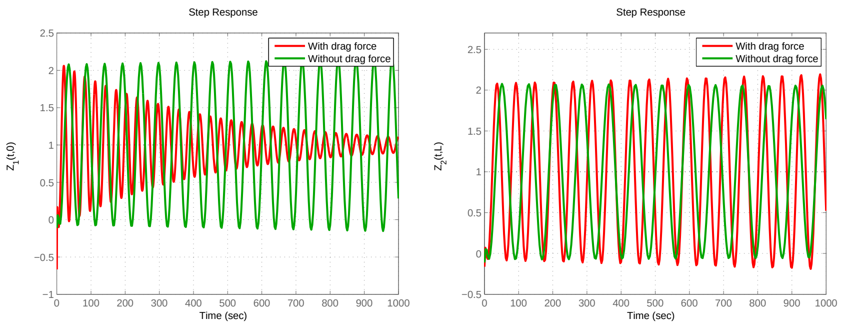

(a) (b)

Figure 6.10: Time responses of the controlled system with and without the drag force for the wave that propagates (a) from the bottom and (b) from the top of the bubble column.

whereas the wave that propagates in the opposite direction fades out faster. The reason for this lies in the drag force. The effect of the drag force is smaller in one direction compared to the other direction. The centralized control design can be also supported by scheduling the control action with respect to space and different oscillation according to the size of the chosen compartments.

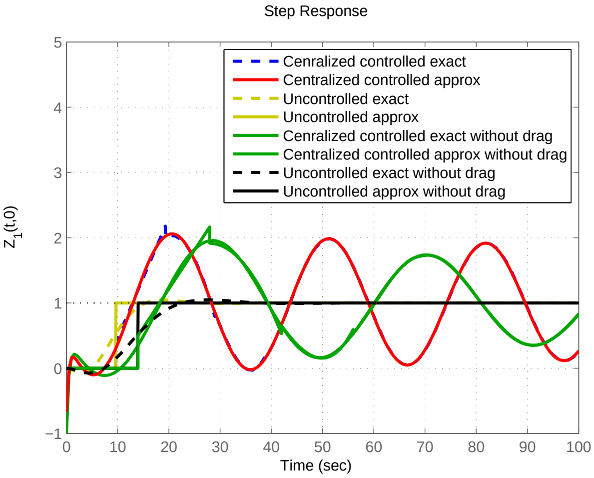

Figure 6.11: Time responses of the controlled and uncontrolled flow with and without the drag flow using the exact and approximate solutions of the wave propagation of the two-phase flow.

6.4 Discussion

In this chapter, we presented different spatially distributed control designs for the control-oriented two-phase flow model derived in Chapter 4. All of the designs presented indicate that the spatially distributed control design for controlling the two-phase flow is not unique. The most suitable design relies on a particular application of the two-phase flow model and control objective. The control objective is extremely important for deriving a model-based control strategy for any practical application of the two-phase flow (e.g., enhancement of mixing, transportation of gas phase in mixture of gas and liquid). To illustrate different control objectives, we derived control laws for two different spatially distributed control designs: boundary and centralized. These two designs are analytically given in Section 6.2.4 and tested on the same numerical example given in Chapters 4 and 5. The results presented in this chapter close the research direction **RD3** and highlight the importance of the control-oriented modeling of fluid systems. The following results that support the development of the control-oriented two-phase flow model can be determined:

- The control laws of distributed control designs presented in Figure 6.1 allow for changes in fluid properties across an entire space. The flow inside a bubble column is controlled by injection and suction of fluid at the boundaries and side wall. This network of actuators and sensors gives new column designs that can operate the flow in a desirable manner which depends on the application of bubble columns.

- The centralized and boundary control designs given in Figure 6.1 are tested on the same numerical example given in Chapter 5. Both of the proposed designs showed performances which satisfy different control goals. The benefits that can be gained from these control goals include reduction of the influence of the drag force in the fluid flow (see Section 6.3, Example 1), and enhancement of mixing of the gas phase and the liquid phase (see Section 6.3, Example 2). These completely different control goals can cause extremely different flow regimes, and cannot be achieved applying a unique actuation strategy.

- The implementation of the proposed spatially distributed control designs involves actuation of the flow at different locations according to the design. The actuation at the boundaries for boundary controller means suction and injection of the fluid throughout the boundaries. The injection/suction at the boundaries particularly affects the shape of the velocity profile near the boundaries and changes the boundary layer shape. The proposed boundary control design can reduce the delay of the flow between the top and bottom boundary of the column and can suppress the fluctuations at the boundaries. Applying the small gain at the boundaries, the delay can be considerably reduced with a small fluctuation of the fluid flow. The actuation strategy in the case of a centralized controller means suction and injection of a secondary flow at the side wall into an already established flow which is in the quasi-steady state regime. The centralized controller improves mixing of the primary flow inside the bubble column and can significantly affect the overall fluid flow field.

- Although in this chapter the unity step responses were presented, which are unlikely to happen in reality for the two-phase flow, they show the system dynamics of the two-phase flow model and influence of the controllers on the dynamics. The input can be easily scaled in the control design in order to described the real injections and suctions throughout the valves. In order to have more realistic simulations, a practical setup and measurements are needed to validate the design.
- Finally, from a computational point of view, the control-oriented modeling based on microscopic conservation laws is very efficient since it takes only a few seconds to simulate the functional relationships of the uncontrolled and controlled flow. This again emphasizes the need for development of the control-oriented two-phase flow model that can be used to structurally influence the fluid flow in real time.

These results conclude the research direction **RD3**, which indicates the steps from control-oriented modeling towards the spatially distributed control designs for the two-phase flow. The results presented in this chapter complete the research objective and show how to structurally influence the hydrodynamics of two-phase flow using the control-oriented model. The main conclusions and recommendations for future work will be summarized in Chapter 7.

Chapter 7

Conclusions and Recommendations

This thesis introduces a new control-oriented microscopic modeling approach to fluid flow systems that leads to different spatially distributed control designs that can be used to structurally influence the fluid flow. In the previous chapters, different modeling and control techniques have been provided in order to develop causal input/output structures and spatially distributed control designs for single-phase and two-phase flow. This chapter summarizes the findings and discusses future research directions in the control-oriented microscopic modeling of fluid flow systems and in the distributed control designs.

7.1 Conclusions

This research project was started in order to develop a control-oriented microscopic two-phase flow model with a causal input-output structure that is well-suited for spatially distributed control designs. The control-oriented microscopic modeling leads to a large number of possible control designs and provides a solution for spatially distributed actuation strategies. In many cases, the microscopic model (PDE model) is much more computationally demanding compared to a spatially uniform model (ODE model). Most of the currently used PDE models of fluid flow systems include the detailed flow phenomena (CFD models), which increase the model complexity and computation time. Although model accuracy is an obvious requirement for any modeling approach, it is still important to establish an exact requirement for a specific application since the accuracy can tremendously increase the computation time and reduce the applicability of a PDE model. Developing control-oriented microscopic models can bridge the gap between the detailed PDE/CFD models of fluid flow systems and spatially nonuniform models (ODE models). The derived control-oriented models can fulfill the increasing expectation of improved performances of processes on the microscopic scale, which is very important in developing sustainable processes in the chemical industry.

In this thesis, we have proposed a theoretical framework for developing a control-oriented microscopic model of a two-phase flow system that can be used to design different spatially distributed controllers. Three research directions were proposed in Section 1 (see Figure 1.3). In the following paragraphs, the conclusions are grouped along two research directions that have been considered in this thesis.

RD1 Numerical approach to microscopic models

- As shown in Chapter 2, microscopic models governed by a set of PDEs require a significant amount of mathematical analysis in order to prove the existence of solutions and to compute the solutions numerically. At the same time, high accuracy means large model complexity. It has been shown that the model complexity and numerical methods are the core of the problem of modeling fluid flow systems, which leads to the main motivation behind the macroscopic properties. Putting a large effort into developing numerical algorithms in order to obtain a solution is, therefore, not a solution to flow control. For a practical application, it is more attractive to observe the problem on a higher level of aggregation defined on a macroscopic scale and to have real-time computation.

- In Chapter 3, the higher level of aggregation, i.e., multiscale modeling, has been tested on single-phase flow in a simple geometry. An important advantage of the macroscopic approach presented in Chapter 3 is that it considers only a few outputs which represent a large set of microstates. The macroscopic flow properties are not only interesting from the application point of view and verification of the mathematical equations, but they can also be considered as output regulation quantity of the fluid properties.

- In Chapter 3, it has been shown that a simple boundary feedback controller can be designed on the already developed CFD model of single-phase flow based on the macroscopic outputs. The boundary feedback controller presented in Chapter 3 succeeded in stabilizing the flow around a desired macroscopic energy with a considerably small control error and with a fast convergence to the desired macroscopic energy. The major conclusion has been that the model-based control of fluid flow is more feasible for systems with a simple geometry relying on less complex models with multiscale modeling compared to the complex CFD models that are currently used to model fluid flow systems.

- In general, the control design presented in Chapter 3 represents a trade-off between the accuracy of discretization and the control design. The results presented in Chapter 3 motivated the introduction of the control-oriented modeling of fluid flow systems.

RD3 Control-oriented modeling

- In the scope of the main research objective, we have investigated two-phase fluid systems and the control-oriented modeling of such systems. As has been discussed in Chapter 1, the main obstacle in using CFD models is the lack of available numerical tools and understanding of dominant dynamics in two-phase flow systems. For this reason, in Chapter 2, different modeling aspects have been outlined, which have to be taken into account while deriving a control-oriented model of the two-phase flow system.

- In Chapter 4, a control-oriented model has been derived under a set of assumptions that were made following the modeling aspects given in Section 2.5. It has been shown that the drag force and interfacial pressure fully determine the well-posedness of any 1D two-phase flow model. This proves to be the key issue in deriving the well-posed control-oriented model with a preserved input/output structure. The derived control oriented-model is a simple mathematical representation of the two-phase flow system in 1D, which is suitable for a wide range of spatially distributed control designs easy to implement.

- In Chapter 4, the eigenvalue analysis and the method of characteristics have been used to analyze the well-posedness of the derived control-oriented model. It has been discovered that the method of characteristics and the eigenvalue analysis can be a guide to help in the selection of the coupling terms and the boundary actuation strategies and causal input/output structures.

- Following the findings from Chapter 4, in Chapter 5 the concept of causal input/output structures of the control-oriented two-phase flow model has been introduced. The causality in case of the PDE models is rather involved, and requires extensive analysis. For this reason, a new representation of the two-phase flow model has been proposed using the Laplace-space transformation of the derived control-oriented two-phase flow model. It was also shown that the selection of inputs and outputs is uniquely determined at the boundaries for the causal two-phase flow. The causality defined in this way gives the exact condition for developing causal input/output structures, which are spatially distributed. The Laplace-space representation of the two-phase flow model was also successfully used to derive rational transfer functions that show the fluid behavior between the boundaries. The computational load has been tremendously reduced, which is very beneficial for on-line control.

- The control-oriented modeling derived in Chapter 4 plays an important role in the development of different actuation strategies which eventually lead to different spatially distributed control designs. This type of modeling represents a trade-off between the accuracy and preservation of the causality discussed in Chapter 5. As shown in Chapter 5, the control-oriented PDE model of two-phase flow is easy to use in a control design where control parameters are tuned based on desired process performances. In general, control-oriented modeling relies on the input/output structure which allows us to structurally influence the flow regimes in a bubble column and to establish the corresponding control design.

- In Chapter 6, we have suggested different spatially distributed control designs. Based on the control laws for spatially distributed controllers, different controllers have been designed that can maintain different flow regimes of two-phase flow in a bubble column. It was also shown that different control problem formulations require different control strategies. Adjusting the control designs, we have shown that the mixing can be enhanced using the spatially distribute centralized controller, whereas the plug flow regime can be adjusted using the boundary controller. Both spatially distributed designs have been tested on the two-phase flow model represented in the Laplace-space domain. The Laplace-space representation of the two-phase flow model is a rather attractive model representation since it does not rely on the choice of discretization methods. Instead, the Laplace-space representation of the two-phase flow model uses rational transfer functions to model the system behavior between the boundaries. These functional relationships can simplify control designs tremendously.

Based on these observations, it can be concluded that the control-oriented modeling of two-phase flow fulfills the main objective of this thesis and gives a new modeling framework for the control of fluid flow systems which advocates low complexity and high applicability of fluid flow models. We would also like to stress that while we have considered the particular two-phase flow problem and specific spatially distributed designs, the techniques and algorithms presented herein can be of use in many other areas of microscopic modeling.

7.2 Recommendations

As a continuation of the results presented and open research questions in the field of flow control, the following challenges can be suggested for future research:

- While a well-posed input/output structure and development of distributed controllers are very promising steps towards automatic operation of a bubble column, there are several issues that need to be addressed before the method can be applied in practice.

- Dissipation of fluid properties at the boundaries is very dependent on the design of practical equipment, and it should be also considered in the design. In practice, different macroscopic scales should be included in control design.

- The quasi steady-state and steady-state regimes have to be validated. This requires a further investigation of the linearization technique presented in Section 4.3.3. This mainly involves different operational regimes and linearized model representations which are not uniform in space. Further investigation in this direction will build a stronger concept of stabilizing different operational regimes.

- Two-phase flow systems can have a wide range of two-phase flow patterns. For instance, the homogeneous two-phase flow is characterized by small-size bubbles which move in a very regular and deterministic way with considerably less drag between the phases, whereas the heterogeneous flow is characterized by small-scale fluctuations that appear to be stochastic and less deterministic in nature. Studying different operational regimes and flow patterns would be an interesting research direction that should aim to underline the physical phenomena behind the two-phase fluid flow and their contribution to the overall spatially distributed control designs. Also, cross-effects have to be taken into account which will result in 2D and 3D two-phase flow models. The analysis should involve model robustness and parameter uncertainty (e.g., bubble diameter, interfacial pressure coefficient, and drag coefficient).

- In the proposed distributed control designs, applying the feedback controller was conceptually straightforward. It would be interesting to investigate other possible spatially distributed control designs that have a feedforward structure. We also suggested localized spatially distributed control designs in Chapter 6, which have not been treated in this thesis, and they can also be investigated in the future.

- Finally, testing the derived two-phase flow model and the proposed spatially distributed designs in practice is required for verification and possible redesigns. Comparing numerical results with experimental results is an essential step in model validation. This might lead to new insights and experiences that will bring the control-oriented modeling from the simulation environment to reality.

The main challenge for future research is to use and improve the microscopic control framework while keeping the necessary practical requirements for industrial purposes. Clearly, this will be a guarantee for the structural development in intensifying chemical processes on the microscopic scale and designing sustainable plants in the future.

Appendix A

Numerical Algorithm for Solving the Single-Phase Flow Model

Assume we have the velocity field $u^n_{i,j}$ and $v^n_{i,j}$ at the n-th time step, and the condition given by (3.1) that has to be satisfied. First, we have to find the solution at the $(n+1)$-th time step $(t+\triangle t)$ by the following three-step approach:

1. *Explicit solutions of the nonlinear terms*
   The nonlinear terms are treated explicitly. This circumvents the solution of the nonlinear terms, introducing the CFL condition that limits the time step by the spatial resolution $\triangle x$

$$\frac{u^*_{i,j} - u^n_{i,j}}{\triangle t} = -((u^n_{i,j})^2_x - (u^n_{i,j} v^n_{i,j})_y,$$
$$\frac{v^*_{i,j} - v^n_{i,j}}{\triangle t} = -((u^n_{i,j} v^n_{i,j})_x - (v^n_{i,j})^2_y.$$

2. *Implicit viscosity*
   The viscosity terms are treated implicitly. If they were treated explicitly, we would have a time step restriction proportional to the spatial discretization squared. This results in two linear systems that have to be solved in each time step.

$$\frac{u^{**}_{i,j} - u^*_{i,j}}{\triangle t} = \frac{1}{Re}(u^{**}_{i,j_{xx}} + u^{**}_{i,j_{yy}}),$$
$$\frac{v^{**}_{i,j} - v^*_{i,j}}{\triangle t} = \frac{1}{Re}(v^{**}_{i,j_{xx}} + v^{**}_{i,j_{yy}}).$$

3. *Pressure correction*
   The intermediate velocity field $(u_{i,j}, v_{i,j})$ are corrected by the gradient of a pressure p_{n+1} to enforce the incompressibility condition (3.1)

$$\frac{u_{i,j}^{n+1} - u_{i,j}^{**}}{\triangle t} = -(p^{n+1})_x,$$
$$\frac{v_{i,j}^{n+1} - v_{i,j}^{**}}{\triangle t} = -(p^{n+1})_y.$$

The pressure is denoted by p^{n+1}, since it is only given implicitly. The pressure term in each point in space is obtained by solving a linear system. In a vector notation, the correction equation reads as

$$\frac{1}{\triangle t}\mathbf{U}^{n+1} - \frac{1}{\triangle t}\mathbf{U}^{n} = -\nabla \mathbf{P}^{n+1},$$

where the capital letters denote the numerical approximation of the discretized PDEs (3.2) and (3.3).

Applying the divergence to both sides yields the linear system

$$-\triangle p^{n+1} = -\frac{1}{\triangle t}\nabla \cdot \mathbf{U}^{n}.$$

Table A.1: Algorithm which is used to correct the pressure term.

Correction steps	
Step 1	Compute $\mathbf{J}^n = \nabla \cdot \mathbf{U}^n$
Step 2	Solve the Poisson equation $\triangle \mathbf{P}^{n+1} = \frac{1}{\triangle t}\mathbf{J}^n$
Step 3	Compute $\mathbf{H}^{n+1} = \nabla \mathbf{P}^{n+1}$
Step 4	Update the velocity field $\mathbf{U}^{n+1} = \mathbf{U}^n - \triangle t \mathbf{H}^{n+1}$

A standard approach to the pressure correction at the boundaries is to prescribe the homogeneous Neumann boundary conditions for **P** whenever the no-slip boundary conditions are prescribed for the velocity field. For the lid-driven cavity problem, this means that the homogeneous Neumann boundary conditions are prescribed for the pressure at each boundary (i.e., the top, bottom, and side walls). This implies that the pressure **P** is only defined up to a constant, since the gradient of **P** enters the momentum equations (3.2) and (3.3).

Appendix B

Linearization of the Two-Phase Flow Model

This section gives a short overview of the linearization of the two-phase flow model derived in Chapter 4, which is used to develop a well-posed actuation structure. The same linearization technique is also used to derive the linearized Navier-Stokes equations [1].

First, we start with the two-phase flow model (4.1), (4.5) and (4.6), where (4.19) is inserted for each state separately

$$\begin{aligned}
&\frac{\partial(\overline{\alpha_g}+\alpha_g')}{\partial t}+\frac{\partial(\overline{\alpha_g}+\alpha_g')}{\partial x}(\overline{v_g}+v_g')+(\overline{\alpha_g}+\alpha_g')\frac{\partial(\overline{v_g}+v_g')}{\partial x}=0,\\
&\rho_g\frac{\partial(\overline{v_g}+v_g')}{\partial t}-\rho_l\frac{\partial(\overline{v_l}+v_l')}{\partial t}+\rho_g(\overline{v_g}+v_g')\frac{\partial(\overline{v_g}+v_g')}{\partial x}-\rho_l(\overline{v_l}+v_l')\frac{\partial(\overline{v_l}+v_l')}{\partial x}\\
&\qquad\qquad+C_p\rho_l((\overline{v_g}+v_g')-(\overline{v_l}+v_l'))^2\frac{\partial(\overline{\alpha_g}+\alpha_g')}{\partial x}\\
&\qquad\qquad=-(\rho_g-\rho_l)g-\big((\overline{v_g}+v_g')-(\overline{v_l}+v_l')\big)\frac{3}{4}\frac{C_d}{d_b}\sqrt{\big((\overline{v_g}+v_g')-(\overline{v_l}+v_l')\big)^2},\\
&\frac{\partial(\overline{\alpha_g}+\alpha_g')}{\partial x}((\overline{v_g}+v_g')-(\overline{v_l}+v_l'))+\frac{\partial(\overline{v_g}+v_g')}{\partial x}(\overline{\alpha_g}+\alpha_g')\\
&\qquad\qquad+(1-(\overline{\alpha_g}+\alpha_g'))\frac{\partial(\overline{v_l}+v_l')}{\partial x}=0.
\end{aligned}$$

Notice that the drag force is simplified using the following relation

$$\alpha_g\alpha_l\left(\frac{1}{\alpha_g}+\frac{1}{\alpha_l}\right)=1,$$

Now, we can evaluate each equation separately in order to obtain the linearized two-phase flow model, which can be written as

$$\frac{\partial\overline{\alpha_g}}{\partial t}+\frac{\partial\overline{\alpha_g}}{\partial x}\overline{v_g}+\overline{\alpha_g}\frac{\partial\overline{v_g}}{\partial x}=0,$$

where $\alpha'_g \frac{\alpha'_g}{\partial x} \approx 0$ for the perturbation in the vicinity of the steady-state solution, i.e.,

$$\frac{\partial \alpha'_g}{\partial t} + \frac{\partial \alpha'_g}{\partial x}\overline{v_g} + \overline{\alpha_g}\frac{\partial v'_g}{\partial x} + \frac{\partial \overline{\alpha_g}}{\partial x}v'_g + \alpha'_g\frac{\partial \overline{v_g}}{\partial x} = 0. \tag{B.1}$$

Equation (B.1) is the linearized mass equation which accounts the variation of the steady-state solution with respect to space $\frac{\partial \overline{\alpha_g}}{\partial x}v'_g$ and $\alpha'_g\frac{\partial \overline{v_g}}{\partial x}$. If the steady-state solution is space independent, the linearized mass equation equals

$$\frac{\partial \alpha'_g}{\partial t} + \frac{\partial \alpha'_g}{\partial x}\overline{v_g} + \overline{\alpha_g}\frac{\partial v'_g}{\partial x} = 0.$$

In contrast to the linearization of the mass equation, the linearization of the momentum equation is more computationally involved due to the nonlinear interfacial pressure and the drag force.

$$\begin{aligned}
\rho_g\frac{\partial(\overline{v_g}+v'_g)}{\partial t} &- \rho_l\frac{\partial(\overline{v_l}+v'_l)}{\partial t} + \rho_g(\overline{v_g}+v'_g)\frac{\partial(\overline{v_g}+v'_g)}{\partial x} - \rho_l(\overline{v_l}+v'_l)\frac{\partial(\overline{v_l}+v'_l)}{\partial x} \\
&+ C_p\rho_l((\overline{v_g}+v'_g)-(\overline{v_l}+v'_l))^2\frac{\partial(\overline{\alpha_g}+\alpha'_g)}{\partial x} \\
&= -(\rho_g-\rho_l)g - \left((\overline{v_g}+v'_g)-(\overline{v_l}+v'_l)\right)\frac{3}{4}\frac{C_d}{d_b}\sqrt{\left((\overline{v_g}+v'_g)-(\overline{v_l}+v'_l)\right)^2},
\end{aligned}$$

which gives

$$\begin{aligned}
\rho_g\frac{\partial \overline{v_g}}{\partial t} - \rho_l\frac{\partial \overline{v_l}}{\partial t} + \rho_g\overline{v_g}\frac{\partial \overline{v_g}}{\partial x} - \rho_l\overline{v_l}\frac{\partial \overline{v_l}}{\partial x} + C_p\rho_l(\overline{v_g}-\overline{v_l})^2\frac{\partial \overline{\alpha_g}}{\partial x}& \\
= -(\rho_g-\rho_l)g - (\overline{v_g}-\overline{v_l})\frac{3}{4}\frac{C_d}{d_b}\sqrt{(\overline{v_g}-\overline{v_l})^2}&.
\end{aligned}$$

The linearized momentum equation is given by

$$\begin{aligned}
\rho_g\frac{\partial v'_g}{\partial t} - \rho_l\frac{\partial v'_l}{\partial t} + \rho_g\overline{v_g}\frac{\partial v'_g}{\partial x} + \rho_g v'_g\frac{\partial \overline{v_g}}{\partial x} - \rho_l\overline{v_l}\frac{\partial v'_l}{\partial x} - \rho_l v'_l\frac{\partial \overline{v_l}}{\partial x}& \\
+ C_p\rho_l\left(\overline{v_g}-\overline{v_l}\right)^2\frac{\partial \alpha'_g}{\partial x} + C_p\rho_l\left(v'_g-v'_l\right)^2\frac{\partial \alpha'_g}{\partial x}& \\
+ 2C_p\rho_l(\overline{v_g}-\overline{v_l})\left(v'_g-v'_l\right)\frac{\partial \alpha'_g}{\partial x}& \\
+ C_p\rho_l\left(v'_g-v'_l\right)^2\frac{\partial \overline{\alpha_g}}{\partial x} + 2C_p\rho_l(\overline{v_g}-\overline{v_l})\left(v'_g-v'_l\right)\frac{\partial \overline{\alpha_g}}{\partial x}& \\
= -\frac{3}{4}\frac{C_d}{d_b}\left(v'_g-v'_l\right)^2 - 2\frac{3}{4}\frac{C_d}{d_b}(\overline{v_g}-\overline{v_l})\left(v'_g-v'_l\right)&.
\end{aligned}$$

Note that the terms $\left(v'_g-v'_l\right)^2\frac{\partial \alpha'_g}{\partial x} \approx 0$, $\left(v'_g-v'_l\right)\frac{\partial \alpha'_g}{\partial x} \approx 0$, and $\left(v'_g-v'_l\right)^2 \approx 0$, thus the final form of the linearized momentum equation is

$$\begin{aligned}\rho_g \frac{\partial v_g'}{\partial t} - \rho_l \frac{\partial v_l'}{\partial t} + \rho_g \overline{v_g} \frac{\partial v_g'}{\partial x} + \rho_g v_g' \frac{\partial \overline{v_g}}{\partial x} - \rho_l \overline{v_l} \frac{\partial v_l'}{\partial x} - \rho_l v_l' \frac{\partial \overline{v_l}}{\partial x} \\ + C_p \rho_l \left(\overline{v_g} - \overline{v_l}\right)^2 \frac{\partial \alpha_g'}{\partial x} + 2 C_p \rho_l \left(\overline{v_g} - \overline{v_l}\right)\left(v_g' - v_l'\right) \frac{\partial \overline{\alpha_g}}{\partial x} \\ = -2 \frac{3}{4} \frac{C_d}{d_b} \sqrt{(\overline{v_g} - \overline{v_l})^2} \left(v_g' - v_l'\right).\end{aligned}$$

And finally, we linearize the algebraic part of the two-phase flow model suggested in Chapter 4. The linearized algebraic equation can be written in terms of perturbations as

$$\begin{aligned}\frac{\partial(\overline{\alpha_g} + \alpha_g')}{\partial x}\left((\overline{v_g} + v_g') - (\overline{v_l} + v_l')\right) + \frac{\partial(\overline{v_g} + v_g')}{\partial x}(\overline{\alpha_g} + \alpha_g') \\ + \left(1 - (\overline{\alpha_g} + \alpha_g')\right)\frac{\partial(\overline{v_l} + v_l')}{\partial x} = 0.\end{aligned} \tag{B.2}$$

The final form of the linearized algebraic equation (B.2) can be obtained from the following equation

$$\frac{\partial \overline{\alpha_g}}{\partial x}(v_g' - v_l') + \frac{\partial \alpha_g'}{\partial x}(\overline{v_g} - \overline{v_l}') + \frac{\partial \overline{v_g}}{\partial x}\alpha_g' + \frac{\partial v_g'}{\partial x}\overline{\alpha_g} + (1 - \overline{\alpha_g})\frac{\partial v_l'}{\partial x} - \alpha_g' \frac{\partial \overline{v_l}}{\partial x} = 0.$$

The linearized two-phase flow model can be written in a compact matrix form as

$$\mathbf{E}\frac{\partial \Phi'}{\partial t} + \mathbf{A}(\overline{\Phi})\frac{\partial \Phi'}{\partial x} + \overline{\mathbf{A}}(\Phi')\frac{\partial \overline{\Phi}}{\partial x} = \mathbf{F}\Phi', \tag{B.3}$$

with

$$\mathbf{A}(\overline{\Phi}) = \begin{bmatrix} \overline{v_g} & \overline{\alpha_g} & 0 \\ C_p \rho_l \left(\overline{v_g} - \overline{v_l}\right)^2 & \rho_g \overline{v_g} & -\rho_l \overline{v_l} \\ \overline{v_g} - \overline{v_l} & \overline{\alpha_g} & 1 - \overline{\alpha_g} \end{bmatrix},$$

$$\overline{\mathbf{A}}(\Phi') = \begin{bmatrix} {v_g}' & {\alpha_g}' & 0 \\ 2C_p \rho_l \left(\overline{v_g} - \overline{v_l}\right)\left({v_g}' - {v_l}'\right) & \rho_g {v_g}' & -\rho_l {v_l}' \\ v_g' - v_l' & {\alpha_g}' & -{\alpha_g}' \end{bmatrix},$$

representing the linearized system matrices, and

$$\mathbf{F} = \begin{bmatrix} 0 & 0 & 0 \\ 0 & -3/2\,\frac{C_d \rho_l \sqrt{\left(\overline{v_g} - \overline{v_l}\right)^2}}{db} & 3/2\,\frac{C_d \rho_l \sqrt{\left(\overline{v_g} - \overline{v_l}\right)^2}}{d_b} \\ 0 & 0 & 0 \end{bmatrix}$$

representing the linearized force vector.

Appendix C

Coordinate Transformations

The coordinate transformation presented in Chapter 4 is based on the following transformation

$$\mathbf{E}^D = \mathbf{E}\mathbf{T} = \begin{bmatrix} 1 & 0 & 0 \\ 0 & 1 & 0 \\ 0 & 0 & 0 \end{bmatrix}, \quad \text{and} \quad \mathbf{T} = \begin{bmatrix} 1 & 0 & 0 \\ 0 & {\rho_g}^{-1} & \rho_l \\ 0 & 0 & \rho_g \end{bmatrix} \quad \text{with } \Phi' = \mathbf{T}\Psi',$$

where **T** stands for the coordinate transformation matrix. Now, we can transform the state vector Φ' into a new state vector Ψ' such that according to the given fluid variables (α_g, v_g, and v_l), the new states are given as

$$\Psi' = \begin{bmatrix} \alpha'_g \\ \rho_g v'_g - \rho_l v'_l \\ \dfrac{v'_l}{\rho_g} \end{bmatrix}.$$

The two-phase flow model written in the Ψ' coordinates reads as

$$\mathbf{E}\mathbf{T}\frac{\partial \Psi'}{\partial t} + \mathbf{A}(\overline{\Psi})\mathbf{T}\frac{\partial \Psi'}{\partial x} = \mathbf{F}\mathbf{T}\Psi', \tag{C.1}$$

which gives

$$\begin{bmatrix} 1 & 0 & 0 \\ 0 & 1 & 0 \\ 0 & 0 & 0 \end{bmatrix} \frac{\partial \Psi'}{\partial t} + \begin{bmatrix} \overline{v_g} & \frac{\overline{\alpha_g}}{\rho_g} & \overline{\alpha_g}\rho_l \\ C_p\,\rho_l\,(\overline{v_g}-\overline{v_l})^2 & \overline{v_g} & \rho_g\overline{v_g}\rho_l - \rho_l\overline{v_l}\rho_g \\ \overline{v_g}-\overline{v_l} & \frac{\overline{\alpha_g}}{\rho_g} & \overline{\alpha_g}\rho_l + (1-\overline{\alpha_g})\,\rho_g \end{bmatrix} \frac{\partial \Psi'}{\partial x} = \tag{C.2}$$

$$\begin{bmatrix} 0 & 0 & 0 \\ 0 & \frac{3}{2}\dfrac{C_d\rho_l\,(\overline{v_g}-\overline{v_l})}{d_b} & -\frac{3}{2}\dfrac{C_d\rho_l\,(\overline{v_g}-\overline{v_l})}{d_b} \\ 0 & 0 & 0 \end{bmatrix} \Psi'$$

From (C.2), the algebraic equation reads as

$$\frac{\partial \Psi_3}{\partial x} = \frac{(\rho_g \overline{v_g} - \rho_g \overline{v_l})}{\rho_g\,(-\overline{\alpha_g}\rho_l - \rho_g + \rho_g \overline{\alpha_g})} \frac{\partial \Psi_1}{\partial x} + \frac{\overline{\alpha_g}}{\rho_g\,(-\overline{\alpha_g}\rho_l - \rho_g + \rho_g \overline{\alpha_g})} \frac{\partial \Psi_2}{\partial x}. \tag{C.3}$$

By subtracting (C.3) from (C.2), the PDAE model of the two-phase flow can be reduced to PDE model

$$\begin{bmatrix} 1 & 0 \\ 0 & 1 \end{bmatrix} \frac{\partial \Psi'}{\partial t} + \begin{bmatrix} \frac{-\rho_g\overline{v_g}+\overline{v_g}\rho_g\overline{\alpha_g}-\overline{\alpha_g}\rho_l\overline{v_l}}{-\overline{\alpha_g}\rho_l-\rho_g+\rho_g\overline{\alpha_g}} & \frac{\overline{\alpha_g}\left(-1+\overline{\alpha_g}\right)}{-\overline{\alpha_g}\rho_l-\rho_g+\rho_g\overline{\alpha_g}} \\ \frac{\left(\overline{v_g}-\overline{v_l}\right)^2\rho_l\left(-C_p\,\rho_l\overline{\alpha_g}+\rho_g\overline{\alpha_g}Cp+\rho_g-\rho_gCp\right)}{-\overline{\alpha_g}\rho_l-\rho_g+\rho_g\overline{\alpha_g}} & \frac{-\rho_g\overline{v_g}+v_{gi}\rho_g\overline{\alpha_g}-\overline{\alpha_g}\rho_l\overline{v_l}}{-\overline{\alpha_g}\rho_l-\rho_g+\rho_g\overline{\alpha_g}} \end{bmatrix} \frac{\partial \Psi'}{\partial x} = \tag{C.4}$$

$$\begin{bmatrix} 0 & 0 \\ -\frac{3}{2}\frac{C_d\rho_l\left(\overline{v_g}-\overline{v_l}\right)\left(-\rho_l\overline{v_g}+\rho_l\overline{v_l}+\rho_g\overline{v_g}-\rho_g\overline{v_l}\right)}{d_b\left(-\overline{\alpha_g}\rho_l-\rho_g+\rho_g\overline{\alpha_g}\right)} & -\frac{3}{2}\frac{C_d\rho_l\left(\overline{v_g}-\overline{v_l}\right)}{d_b\left(-\overline{\alpha_g}\rho_l-\rho_g+\rho_g\overline{\alpha_g}\right)} \end{bmatrix} \Psi',$$

The directional derivatives in (C.4) can be decoupled using the second coordinate transformation which gives the following equation written in the **W**′ coordinates as

$$\frac{\partial \mathbf{W}'}{\partial t} + \mathbf{V}^{-1} \begin{bmatrix} \frac{-\rho_g\overline{v_g}+\overline{v_g}\rho_g\overline{\alpha_g}-\overline{\alpha_g}\rho_l\overline{v_l}}{-\overline{\alpha_g}\rho_l-\rho_g+\rho_g\overline{\alpha_g}} & \frac{\overline{\alpha_g}\left(-1+\overline{\alpha_g}\right)}{-\overline{\alpha_g}\rho_l-\rho_g+\rho_g\overline{\alpha_g}} \\ \frac{\left(\overline{v_g}-\overline{v_l}\right)^2\rho_l\left(-C_p\,\rho_l\overline{\alpha_g}+\rho_g\overline{\alpha_g}C_p+\rho_g-\rho_gC_p\right)}{-\overline{\alpha_g}\rho_l-\rho_g+\rho_g\overline{\alpha_g}} & \frac{-\rho_g\overline{v_g}+v_{gi}\rho_g\overline{\alpha_g}-\overline{\alpha_g}\rho_l\overline{v_l}}{-\overline{\alpha_g}\rho_l-\rho_g+\rho_g\overline{\alpha_g}} \end{bmatrix} \mathbf{V}\frac{\partial \mathbf{W}'}{\partial x} \tag{C.5}$$

$$= \begin{bmatrix} 0 & 0 \\ -\frac{3}{2}\frac{C_d\rho_l\left(\overline{v_g}-\overline{v_l}\right)\left(-\rho_l\overline{v_g}+\rho_l\overline{v_l}+\rho_g\overline{v_g}-\rho_g\overline{v_l}\right)}{d_b\left(-\overline{\alpha_g}\rho_l-\rho_g+\rho_g\overline{\alpha_g}\right)} & -\frac{3}{2}\frac{C_d\rho_l\left(\overline{v_g}-\overline{v_l}\right)}{d_b\left(-\overline{\alpha_g}\rho_l-\rho_g+\rho_g\overline{\alpha_g}\right)} \end{bmatrix} \mathbf{W}',$$

where the transformation matrix **V** equals

$$\mathbf{V} = \begin{bmatrix} 1/2 & 1/2 \\ 1/2\sigma & -1/2\sigma \end{bmatrix},$$

with σ being

$$\sigma = \frac{\rho_l\,(\overline{v_g} - \overline{v_l})^2\,(-C_p\,\rho_l\overline{\alpha_g} + \rho_g\overline{\alpha_g}C_p + \rho_g - \rho_g C_p)}{\sqrt{\alpha_{gi}\rho_l\,(\overline{v_g} - \overline{v_l})^2\,(-1 + \overline{\alpha_g})\,(-C_p\,\rho_l\overline{\alpha_g} + \rho_g\overline{\alpha_g}C_p + \rho_g - \rho_g C_p)}}.$$

Finally, the two-phase flow model written as the PDE model with the decoupled directional derivatives can be written as

$$\frac{\partial \mathbf{W}'}{\partial t} + \begin{bmatrix} \lambda_1 & 0 \\ 0 & \lambda_2 \end{bmatrix} \frac{\partial \mathbf{W}'}{\partial x} = \begin{bmatrix} c_{11} & c_{12} \\ c_{21} & c_{22} \end{bmatrix} \mathbf{W}', \tag{C.6}$$

where

$$\lambda_1 = \frac{\overline{\alpha_g}\rho_l\overline{v_l} + \overline{\alpha_l}\rho_g\overline{v_g}}{\overline{\alpha_g}\rho_l + \overline{\alpha_l}\rho_g} + \sqrt{D_c}, \tag{C.7}$$

$$\lambda_2 = \frac{\overline{\alpha_g}\rho_l\overline{v_l} + \overline{\alpha_l}\rho_g\overline{v_g}}{\overline{\alpha_g}\rho_l + \overline{\alpha_l}\rho_g} - \sqrt{D_c}, \tag{C.8}$$

with

$$D_c = \overline{\alpha_g}\rho_g\rho_l\left(\overline{v_g} - \overline{v_l}\right)^2\left(-1 + \overline{\alpha_g}\right)\left(1 - \left(\frac{\rho_l\overline{\alpha_g} + \overline{\alpha_l}\rho_g}{\rho_g}\right)C_p\right). \tag{C.9}$$

Appendix D

Padé Approximant

The second step in the numerical approximation of the boundary conditions and the transportation delays described in Chapter 5 is the Padé approximation. In general, the Padé approximation uses the quotient of two polynomials to estimate a power series which can be defined as

$$[L,M] = \frac{P_L(s)}{R_M(s)},$$

where $P_L(s)$ is a polynomial of degree L and $R_M(s)$ is a polynomial of degree M [7]. The explicit equation that approximate the power series $e^{\lambda_i^*(s)}$ reads from

$$\lim_{s\to+\infty} \frac{R_M(s)h(s) - P_L(s)}{s^{L+M+1}} = 0.$$

The more accurate approximations can be obtained using higher degree of polynomials to replace the output delay element. To clarify this, consider a delay, of which the Taylor expansion is given by the following series

$$e^{-h_1 s} = 1 - h_1 s + \frac{1}{2}h_1^2 s^2 - \frac{1}{6}h_1^3 s^3 + \ldots + \frac{1}{2!}h_1^n s^n$$

The first three terms of the expansion are 1, $h_1 s$ and $\frac{1}{2}h_1^2 s^2$. Suppose now that we approximate the delay by the following first order system

$$\frac{1}{1+as} = 1 - as + a^2 s^2.$$

Then, by choosing $a = h_1$, the first two terms of the approximation match those of the delay. If, instead, we approximate the delay by the following expression

$$\frac{1 - \frac{h_1}{2}s}{1 + \frac{h_1}{2}s} = 1 - h_1 s + \frac{1}{2}h_1^2 s^2 - h_1^3 s^3 + \ldots + h_1^n s^n,$$

then, we can expect more accuracy since its first three coefficients match those of the delay $e^{-h_1 s}$. Usually, the more coefficients in $P_L(s)$ and $R_M(s)$ that match the delay, the more accurate the approximation becomes. As an illustration, we consider here a pure delay function e^{-s} which is approximated by the first-order [1,1], second-order [2,2], and third-order [3,3] Padé approximations as

$$\begin{aligned}
[1,1] &= \frac{1-\frac{1}{2}s}{1+\frac{1}{2}s} = 1 - s + \frac{1}{2}s^2 - \frac{1}{4}s^3 + \frac{1}{8}s^4 + O(s^5),\\
[2,2] &= \frac{1-\frac{1}{2}s+\frac{1}{12}s^2}{1+\frac{1}{2}s+\frac{1}{12}s^2} = 1 - s + \frac{1}{2}s^2 - \frac{1}{6}s^3 + \frac{1}{24}s^4 + O(s^5),\\
[3,3] &= \frac{1-\frac{1}{2}s+\frac{1}{10}s^2-\frac{1}{120}s^3}{1+\frac{1}{2}s+\frac{1}{10}s^2+\frac{1}{120}s^3} = 1 - s + \frac{1}{2}s^2 - \frac{1}{6}s^3 + \frac{1}{24}s^4 + O(s^5).
\end{aligned}$$

As shown, the polynomial coefficients for the second and third-order approximations are the same for the first four terms, whereas for the higher order terms, they differ slightly from each other.

Bibliography

[1] O.M. Aamo and M. Krstić. *Flow control by feedback: stabilization and mixing*. Springer Verlag, 2003.

[2] O.M. Aamo, M. Krsti, and T.R. Bewley. Control of mixing by boundary feedback in 2D channel flow. *Automatica*, 39(9):1597–1606, 2003.

[3] J. Alvare and M.H. Al-Dahhan. Liquid phase mixing in trayed bubble column reactors. *Chemical Engineering Science*, 61(6):1819–1835, 2006.

[4] J.D. Anderson and J.F. Wendt. *Computational fluid dynamics*. McGraw-Hill New York, 1995.

[5] P. Astrid. *Reduction of process simulation models-a proper orthogonal decomposition approach*. PhD thesis, Eindhoven University of Technology, 2004.

[6] P.W. Atkins. *Concepts in physical chemistry*. Oxford University Press Oxford, 1995. ISBN 0198559291.

[7] G.A. Baker. The existence and convergence of subsequences of Padé approximants. *Journal of Mathematical Analysis and Applications*, 43(2):498–528, 1973.

[8] A. Balogh, W.J. Liu, and M. Krstic. Stability enhancement by boundary control in 2-D channel flow. *IEEE Transactions on Automatic Control*, 46(11):1696–1711, 2001.

[9] A. Balogh, O.M. Aamo, and M. Krstic. Optimal mixing enhancement in 3-d pipe flow. *IEEE Transactions on Control Systems Technology*, 13(1):27–41, 2005.

[10] O.S. Balogun, M. Hubbard, and J.J. DeVries. Automatic control of canal flow using linear quadratic regulator theory. *Journal of Hydraulic Engineering*, 114 (1):75–102, 1988.

[11] B. Bamieh, F. Paganini, and M.A. Dahleh. Distributed control of spatially invariant systems. *IEEE Transactions on Automatic Control*, 47(7):1091–1107, 2002.

[12] G. Bastin, J.M. Coron, and B. d'Andrea Novel. Boundary feedback control and Lyapunov stability analysis for physical networks of 2× 2 hyperbolic balance laws. In *Proceedings of the 47th IEEE Conference on Decision and Control*, pages 1454–1458, 2008.

[13] G. Besancon. Observer design for nonlinear systems. *Advanced Topics in Control Systems Theory*, 328:61–89, 2006.

[14] T.R. Bewley. Flow control: new challenges for a new renaissance. *Progress in Aerospace Sciences*, 37(1):21–58, 2001.

[15] T.R. Bewley, P. Moin, and R. Temam. DNS-based predictive control of turbulence: an optimal benchmark for feedback algorithms. *Journal of Fluid Mechanics*, 447:179–225, 2001.

[16] A. Biesheuvel and L. Wijngaarden. Two-phase flow equations for a dilute dispersion of gas bubbles in liquid. *Journal of Fluid Mechanics*, 148:301–18, 1984.

[17] R.B. Bird, W.E. Stewart, and E.N. Lightfoot. *Transport phenomena*. Madison, USA, 1960.

[18] K.B. Bischoff and O. Levenspiel. Fluid dispersion-generalization and comparison of mathematical models. I. Generalization of models. *Chemical Engineering Science*, 17:245–255, 1962.

[19] A. Bressan. *Hyperbolic systems of conservation laws: the one-dimensional Cauchy problem*. Oxford University Press, USA, 2000.

[20] E.F. Camacho and C. Bordons. *Model predictive control*. Springer Verlag, 2004.

[21] L. Cattafesta, D. Williams, C. Rowley, and F. Alvi. Review of active control of flow-induced cavity resonance. *The American Institute of Aeronautics and Astronautics*, 3567:2003, 2003.

[22] J.C. Charpentier. Modern chemical engineering in the framework of globalization, sustainability, and technical innovation. *Industrial & Engineering Chemistry Research*, 46(11):3465–3485, 2007.

[23] P. Chen, M.P. Dudukovic, and J. Sanyal. Three-dimensional simulation of bubble column flows with bubble coalescence and breakup. *AIChE journal*, 51(3): 696–712, 2005.

[24] A.J. Chorin. Numerical study of slightly viscous flow. *Journal of Fluid Mechanics*, 57(04):785–796, 1973.

[25] P.D. Christofides. *Nonlinear and robust control of PDE systems: methods and applications to transport-reaction processes*. Birkhauser, 2001.

[26] J.M. Coron, B. d'Andrea Novel, and G. Bastin. A strict Lyapunov function for boundary control of hyperbolic systems of conservation laws. In *Proceedings of the 43rd IEEE Conference on Decision and Control*, pages 3319–3323, 2004.

[27] L. Cortelezzi and J.L. Speyer. Robust reduced-order controller of laminar boundary layer transitions. *Physical Review E*, 58(2):1906–1910, 1998.

[28] L. Cortelezzi, K.H. Lee, J. Kim, and J.L. Speyer. Skin-friction drag reduction via robust reduced-order linear feedback control. *International Journal of Computational Fluid Dynamics*, 11:79–92, 1998.

[29] R. Courant and D. Hilbert. *Methods of mathematical physics. Vol.2. Partial differential equations*. Interscience New York, 1989.

[30] E.L. Cussler. *Diffusion: Mass transfer in fluid systems*. Cambridge University Press, 1997.

[31] R. D'Andrea and G.E. Dullerud. Distributed control design for spatially interconnected systems. *IEEE Transactions on Automatic Control*, 48(9):1478–1495, 2003.

[32] D.C. Dankworth and S. Sundaresan. Time-dependent vertical gas-liquid flow in packed beds. *Chemical Engineering Science*, 47:337–46, 1992.

[33] A.M. Davidson and I.R. Walters. Linear system reduction using approximate momentum matching. *IEE Proceedings D, Control Theory and Applications*, 135:73–78, 1988.

[34] J. De Halleux, C. Prieur, J.M. Coron, B. d'Andrea Novel, and G. Bastin. Boundary feedback control in networks of open channels. *Automatica*, 39(8):1365–1376, 2003.

[35] W.-D. Deckwer. *Bubble column reactors*. Wiley, 1992.

[36] S. Degaleesan, S. Roy, S.B. Kumar, and M.P. Duduković. Liquid mixing based on convection and turbulent dispersion in bubble columns. *Chemical Engineering Science*, 51(10):1967–1976, 1996.

[37] S. Degaleesan, M.P. Dudukovic, B.A. Toseland, and B.L. Bhatt. A two-compartment convective-diffusion model for slurry bubble column reactors. *Industrial and Engineering Chemistry Research*, 36:4670–4680, 1997.

[38] S. Djordjevic, P.M.J. Van den Hof, D. Jeltsema, and R. vent Veen. Control of cavity flow based on a macroscopic observation. In *Proceedings of the European Control Conference 2009*, pages 1233–1238, 2009.

[39] S. Djordjevic, O.H. Bosgra, P.M.J. Van den Hof, and D. Jeltsema. Boundary actuation structure of linearized two-phase flow. In *Proceedings of the American Control Conference 2010*, pages 3759–3764, 2010.

[40] S. Djordjevic, O.H. Bosgra, and P.M.J. Van den Hof. Boundary control of two-phase fluid flow using the Laplace-space domain. In *Proceedings of the American Control Conference 2011*, 2011.

[41] D.A. Drew. Mathematical modeling of two-phase flow. *Annual review of fluid mechanics*, 15(1):261–291, 1983.

[42] J.H. Ferziger. *Numerical methods for engineering applications, 2nd Edition*. John Wiley & Sons Inc, 1998.

[43] A. Forret, J.M. Schweitzer, T. Gauthier, R. Krishna, and D. Schweich. Scale up of slurry bubble reactors. *Oil and Gas Science and Technology*, 61(3):443, 2006.

[44] M. Gad-el Hak. *Flow control: passive, active, and reactive flow management*. Cambridge University Press, 2000. ISBN 0521770068.

[45] S.D. Gharat and J.B. Joshi. Transport phenomena in bubble column reactors I: Flow pattern. *The Chemical Engineering Journal*, 48(3):141–151, 1992.

[46] S.K. Godunov. A finite difference method for the numerical computation of discontinuous solutions of the equations of fluid dynamics. *Mat. Sb*, 47(3):271–290, 1959.

[47] M. Ishii and T. Hibiki. *Thermo-fluid dynamics of two-phase flow*. Springer, 2006.

[48] A. Isidori. *Nonlinear control systems*. Springer Verlag, 1995.

[49] H.A. Jakobsen, B.H. Sannæs, S. Grevskott, and H.F. Svendsen. Modeling of bubble driven vertical flows. *Industrial & Engineering Chemistry Research*, 36: 4052–4074, 1997.

[50] A. Jeffrey. *Applied partial differential equations: an introduction*. Academic Press, 2002. ISBN 0123822521.

[51] J.B. Joshi. Computational flow modelling and design of bubble column reactors. *Chemical Engineering Science*, 56:5893–5933, 2001.

[52] S.S. Joshi, J.L. Speyer, and J. Kim. A systems theory approach to the feedback stabilization of infinitesimal and finite-amplitude disturbances in plane Poiseuille flow. *Journal of Fluid Mechanics*, 332:157–184, 1997.

[53] S.S. Joshi, J.L. Speyer, and J. Kim. Finite dimensional optimal control of Poiseuille flow. *Journal of Guidance Control and Dynamics*, 22:340–348, 1999.

[54] M.R. Jovanovic and B. Bamieh. Lyapunov-based distributed control of systems on lattices. *IEEE Transactions on Automatic Control*, 50(4):422–433, 2005.

[55] M.R. Jovanovic and B. Bamieh. Componentwise energy amplification in channel flows. *Journal of Fluid Mechanics*, 534:145–183, 2005.

[56] S.M. Kang, V. Ryder, L. Cortelezzi, and J.L. Speyer. State-space formulation and controller design for three-dimensionalchannel flows. In *American Control Conference, 1999. Proceedings of the 1999*, volume 3, 1999.

[57] K. Karhunen. Zur spektraltheorie stochastischer prozesse. *Ann. Acad. Sci. Fennicae, Ser.A1*, 34, 1946.

[58] D. Kondepudi. *Introduction to modern thermodynamics*. John Wiley & Sons Inc, 2008.

[59] R. Krishna and S.T. Sie. Design and scale-up of the Fischer–Tropsch bubble column slurry reactor. *Fuel Processing Technology*, 64(1-3):73–105, 2000.

[60] M. Krstic and A. Smyshlyaev. Boundary control of PDEs, 2008.

[61] R.T. Lahey and D.A. Drew. On the development of multidimensional two-fluid models for vapor/liquid two-phase flows. *Chemical engineering communications*, 118:125–139, 1992.

[62] D. Lathouwers. *Modelling and Simulation of Turbulent Bubbly Flow*. PhD thesis, Delft University of Technology, The Netherlands, 1999.

[63] G. Lavalle, A. Clausse, and J. Converti. A contribution to a kinetic formulation of gas-liquid flows. *Chemical Engineering Communications*, 120:99–109, 1993.

[64] O. Levenspiel. *Chemical engineering reaction*. Jhon Wiley & Sons, NewYork, 1999.

[65] X. Litrico and D. Georges. Robust LQG control of single input multiple-outputs dam-river systems. *International Journal of Systems Science*, 32(6):795–805, 2001.

[66] M. Loève. Funcions aléatoire de second ordre. *Comptes Rendus Acad. Sci. Paris*, 220, 1945.

[67] J.D. Logan and K. Ames. *An introduction to nonlinear partial differential equations*. Wiley New York, 1994.

[68] O. Moleurs and M. Kurtin. Hydrodynamics of bubble columns in the uniform bubbling regime. *Chemical Engineering Science*, 40(4):647–652, 1985.

[69] B. Moore. Principal component analysis in linear systems: Controllability, observability, and model reduction. *IEEE Transactions on Automatic Control*, 26 (1):17–32, 1981.

[70] R.F. Mudde. Gravity-driven bubbly flows. *Annual review of fluid mechanics*, 37 (1):393, 2005.

[71] M. Ndjinga, A. Kumbaro, F. De Vuyst, and P. Laurent-Gengoux. Influence of interfacial forces on the hyperbolicity of the two-fluid model. In *5th International Symposium on Multiphase Flow, Xian, China*, 2005.

[72] R.S. Oey. *Gas-liquid flows in a two-fluid formalism: Modeling and validation of closure relations*. PhD thesis, Delft Universioty of Technology, 2005.

[73] J.W. Park, D.A. Drew, and R.T. Lahey, Jr. The analysis of void wave propagation in adiabatic monodispersed bubbly two-phase flows using an ensemble-averaged two-fluid model. *International Journal of Multiphase Flow*, 24(7):1205–1244, 1999.

[74] H.M. Paynter. *Analysis and design of engineering systems*. MIT press Cambridge, Mass., 1961.

[75] P. Philips, M. Weiss, and H.A. Preisig. A design strategy for discrete control of continuous systems. In *Proceedings of the American Control Conference 1999*, volume 3, pages 2097–2101, 1999.

[76] P. P.H.H. Philips. *Modelling, control and fault detection of discretely-observed systems*. PhD thesis, Eindhoven University of Technology, 2001.

[77] M.A. Pinsky and A. Gray. *Partial differential equations and boundary-value problems with applications*. McGraw-Hill New York, 1991.

[78] H.A. Preisig. A mathematical approach to discrete-event dynamic modelling of hybrid systems. *Computers & Chemical Engineering*, 20:1301–1306, 1996.

[79] J. Raisch and S.D. O'Young. Discrete approximation and supervisory control of continuous systems. *IEEE Transactions on Automatic Control*, 43(4):569–573, 1998.

[80] V.H. Ransom and D.L. Hicks. Hyperbolic two-pressure models for two-phase flow. *Journal of Computational Physics*, 53(1):124–151, 1984.

[81] H.K. Rhee, R. Aris, and N.R. Amundson. *First-order partial differential equations, vol. 1: Theory and application of hyperbolic systems of quasilinear equations*. Courier Dover Publications, 2001.

[82] K. Rietema. Science and technology of dispersed two-phase systems–I and II. *Chemical Engineering Science*, 37(8):1125–1150, 1982.

[83] K. Rietema and H.E.A. Van Den Akker. On the momentum equations in dispersed two-phase systems. *International Journal of Multiphase Flow*, 9:21–36, 1983.

[84] D.E. Rosner. *Transport processes in chemically reacting flow systems*. Dover Pubns, 2000.

[85] C.W. Rowley and V. Juttijudata. Model-based control and estimation of cavity flow oscillations. In *Proceedings of the 44th IEEE Conference on Decision and Control and European Control Conference 2005*, pages 512–517, 2005.

[86] C.W. Rowley, T. Colonius, and A.J. Basu. On self-sustained oscillations in two-dimensional compressible flow over rectangular cavities. *Journal of Fluid Mechanics*, 455:315–346, 2002.

[87] C.W. Rowley, T. Colonius, and R.M. Murray. Model reduction for compressible flows using POD and Galerkin projection. *Physica D: Nonlinear Phenomena*, 189(1-2):115–129, 2004.

[88] N.R. Sandell Jr, P. Varaiya, and M. Athans. Survey of decentralized control methods for large scale systems. *Tutorial, distributed control*, 23(2):195, 1982.

[89] J.M.A. Scherpen. *Balancing for Nonlinear Systems. PhD dissertation,*. PhD thesis, Department of Applied Mathematics, University of Twente, The Netherlands, 1994.

[90] Benjamin Seibold. Course 18.086: Mathematical methods for engineers: Applied mathematics, 2007. URL http://math.mit.edu/classes/18.086/.

[91] D.D. Siljak. *Large-scale dynamic systems: stability and structure*. North-Holland, 1978.

[92] H. Stadtke. *Gasdynamic aspects of two-phase flow : hyperbolicity, wave propagation phenomena, and related numerical methods*. Wiley-VCH, 2006.

[93] J.H. Stuhmiller. The influence of interfacial pressure forces on the character of two-phase flow model equations. *International Journal of Multiphase Flow*, 3: 551–560, 1977.

[94] Y. Taitel, D. Bornea, and A.E. Dukler. Modelling flow pattern transitions for steady upward gas-liquid flow in vertical tubes. *AIChE Journal*, 26(3):345–354, 1980.

[95] P. Therning and A. Rasmuson. Liquid dispersion and gas holdup in packed bubble columns at atmospheric pressure. *Chemical Engineering Journal*, 81 (1-3):69–81, 2001.

[96] P. Van Dooren. Gramian based model reduction of large-scale dynamical systems. *Numerical analysis 1999*, page 231, 2000.

[97] T. Van Gerven and A. Stankiewicz. Structure, energy, synergy, time: the fundamentals of process intensification. *Industrial & Engineering Chemistry Research*, 48(2):814–826, 2009.

[98] P. Wesseling. *Principles of computational fluid dynamics*. Springer Verlag, 2000.

[99] J.O. Wilkes and S.G. Birmingham. *Fluid mechanics for chemical engineers with Microfluidics and CFD*. Prentice Hall Professional Technical Reference, 2006.

[100] C.Z. Xu and G. Sallet. Proportional and Integral regulation of irrigation canal systems governed by the Saint–Venant equation. In *Proceedings of the 14th IFAC World Congress*, 1999.

[101] G. Yadigaroglu and R.T. Lahey Jr. On the various forms of the conservation equations in two-phase flow. *International Journal of Multiphase Flow*, 2(5-6): 477–494, 1976.

[102] Y.B. Yang, N. Devanathan, and M.P. Duduković. Liquid backmixing in bubble columns via computer-automated radioactive particle tracking (CARPT). *Experiments in Fluids*, 16(1):1–9, 1993.

Glossary

Lists of symbols and notations

Below follows a list of the most frequently used symbols and notations in this thesis.

Symbol	Description	Units
m	mass	kg
ρ	density	kg/m^3
v	velocity	m/s
E	energy	J/m^3
t	time	s
Φ	state vector	-
S	source term	-
L	length	m
V	volume	m^3
x	x-direction in the Cartesian coordinates	-
y	y-direction in the Cartesian coordinates	-
A	cross section area	m^2
n	normal vector on the surface A	m
C	concentration	mol/m^3
D_e	effective diffusion coefficient	-
r	reaction rate	1/s
Pe	Peclet number	-
p	pressure	N/m^2
μ	fluid viscosity	kg/(sm)
g	gravity acceleration	m/s^2
θ	angle	rad

Symbol	**Description**	**Units**
α	volumetric fraction	-
m	number of phases	-
ℓ	phase indicator	-
$p_{\ell,i}$	interfacial pressure	$\mathrm{N/m^2}$
F	coupling term	N
F_d	drag force	N
F_a	added mass force	N
F_l	transversal force	N
F_h	force due to collective memory effects	N
T	temperature	C
D_T	thermal diffusion coefficient	-
c_p	specific heat capacity	$\mathrm{J/K}$
κ	thermal conductivity	$\mathrm{W/(Km)}$
u	state	-
a	coefficient	-
b	coefficient	-
c	coefficient	-
d	coefficient	-
D	discriminant	-
c	Courant number	-
Ω	rectangular domain	-
u	dimensionless velocity component in x-direction	-
v	dimensionless velocity component in y-direction	-
Re	Reynolds number	-
ω	dimensionless velocity of the lid	-
z	state vector	-
w	boundary input	-
Σ	systems	-
k	macroscopic observation index	-
$z^*_{i,j}$	steady-state solution	-
$e_{i,j}$	error	-
ξ	state	-
β	drag closer term	-
C_D	drag coefficient	-
C_p	interfacial pressure coefficient	-
d	diameter of a single bubble	-
$\mathbf{E}$	system matrix	-
$\mathbf{A}$	system matrix	-
$\mathbf{c}$	state vactor	-

Symbol	Description	Units
λ_i	eigenvalues	-
a_1	coefficient of a characteristic polynomial	-
a_2	coefficient of a characteristic polynomial	-
a_3	coefficient of a characteristic polynomial	-
D_c	discriminant	-
ξ_i	states	-
$\mathbf{\Psi}$	state vector	-
$\mathbf{T}$	transformation matrix	-
$\mathbf{V}$	transformation matrix	-
$\mathbf{W}$	state vector	-
A_{11}	state matrix of spatially discretized model	-
A_{12}	state matrix of spatially discretized model	-
A_{21}	state matrix of spatially discretized model	-
A_{22}	state matrix of spatially discretized model	-
B_1	input matrix of spatially discretized model	-
B_2	input matrix of spatially discretized model	-
$\lambda_i^*(s)$	eigenvalues in the Laplace-space domain	-
$\mathcal{A}(s)$	the system matrix parametrized by s	-
$\mathbf{B}(x)$	the spatially distributed input matrix	-
$\varepsilon(s)$	function in the Laplace-space domain	-
$\mathbf{Q}$	transformation matrix	-
q_{11}	element of matrix $\mathbf{Q}$	-
q_{12}	element of matrix $\mathbf{Q}$	-
q_{21}	element of matrix $\mathbf{Q}$	-
q_{22}	element of matrix $\mathbf{Q}$	-
$\mathbf{G}$	rational transfer function matrix	-
$h_{i,0}$	coefficient of polynomial	-
$h_{i,1}$	coefficient of polynomial	-
$h_{i,2}$	coefficient of polynomial	-
$h_{i,n}$	coefficient of polynomial	-
K_{11}	boundary controller	-
K_{12}	boundary controller	-
K_{21}	boundary controller	-
K_{22}	boundary controller	-
K_i	distributed controller	-
$\mathbf{H}$	vector	-
$\mathbf{J}$	vector	-
$\mathbf{P}$	discretized pressure written as a vector	-

Operator	**Description**
∂	partial derivatives
∇	gradient operator
$\nabla\cdot$	divergence operator
$'$	fluctuations
$\triangle$	finite difference operator
$\overline{(\cdot)}$	averaged quantity
$f_{i,j}$	state function
$g_{i,j}$	state function
$\psi_{i,j}$	state function
h	output function
s	Laplace varable

Sub/Superscript	**Description**
in	inlet
out	outlet
x	x-component in the Cartesian coordinates
y	y-component in the Cartesian coordinates
z	z-component in the Cartesian coordinates
m	number of phases
ℓ	phase indicator
g	gas phase
l	liquid phase
i	spatial index in the x-direction on microscopic scale
j	spatial index in the y-direction on microscopic space
n	number of discretization points in microscopic space
k	spatial index on macroscopic space
n	number of discretization points in microscopic space
n	number of discretization points in macroscopic space
d	desired value
P	proportional action
I	integral action
$\mathbf{D}$	diagonalized
s	slip
down	downwards
up	upwards
red	reduced
in	inlet
co	co-current flow
cc	counter-current flow

Abbreviation	**Description**
CSTR	Continuous Stirred-Tank Reactor
PFR	Plug Flow Reactor
PID	Proportional-Integral-Derivative
MPC	Model-Based Predictive Controller
CFD	Computational Fluid Dynamics
RD	Research Direction
DAE	Differential Algebraic Equation
ODE	Ordinary Differential Equation
PDAE	Partial Differential Algebraic Equation
PDE	Partial Differential Equation
1D	One Dimensional
2D	Two Dimensional
3D	Three Dimensional
LQ	Linear Quadratic
DNS	Direct Numerical Simulations

Summary

The recent progress in the chemical industry is now forcing engineers and physicists to get to deal with control-oriented modeling of material properties on microscopic scale inside reactors in order to build more efficient chemical plants. The control-oriented modeling provides a new way of thinking about the purposes of models in the chemical industry, the relationships between the material properties inside the chemical reactors, and the level of details needed for control designs.

The main objective of this thesis is to offer the physics, chemical, and control communities a unified set of rules and conditions for the control-oriented microscopic modeling of fluid systems in the chemical industry. The work presented in this thesis includes not only the physics of fluid systems and first principle models, but also suggests requirements for developing causal input/output structures and spatially distributed control designs.

The first part of this thesis concerns the problem of the microscopic modeling of a fluid flow system and the requirements needed to obtain a control-oriented model of the fluid flow system. The derivation of the control-oriented model can be a rather demanding task due to the fact that the dynamics of a particular flow regime have to be determined explicitly. In order to demonstrate the flow control, a single-phase flow system in simple geometry, such as a lid-driven cavity case, is considered. The complexity of the single-phase flow model is illustrated using the Navier-Stokes equations and different discretization methods. The conventional approach to the microscopic fluid flow model involves fine discretization of the microscopic model in order to obtain microstates which can be manipulated and measured. However, the microstates give a very detailed picture of the fluid flow that, in many cases, is not directly measurable. Therefore, different modeling scales have to be considered for designing spatially distributed control strategies for the single-phase flow. In order to demonstrate the applicability of the different modeling scales for the fluid flow system, a macroscopic output regulation is studied on the lid-driven cavity case, which has a broad range of industrial applications.

The second part of this thesis deals with the problem of deriving a control-oriented model of a two-phase fluid flow system, which is complementary to the single-phase flow model given in the first part of the thesis. In essence, the control-oriented two-phase flow modeling namely means deriving a simplified model that is available from the first principles and to examine the dominant dynamics. The control-oriented model

of the two-phase flow investigates the possibility of identifying different flow regimes inside a bubble column reactor, where the fluid is injected at different locations of the reactor. Besides being useful for control, the control-oriented model of the two-phase flow inside the bubble column also suggest new reactor designs based on the most efficient actuation strategies. Following a wide range of possible actuation structures for the two-phase fluid flow, different spatially distributed control designs for the two-phase flow inside the bubble column reactor are suggested in this thesis. The spatially distributed control strategies can be successfully used to stabilize or destabilize the two-phase flow around a desired two-phase flow regime.

In general, the stabilization or destabilization of the fluid flow plays a crucial role in designing efficient and sustainable processes that rely on the manipulation of hydrodynamics. The spatially distributed control designs of the single-phase and two-phase flow systems presented in this thesis suggest more efficient reactor designs and new developments in the process intensification in the chemical industry.

Samenvatting

De recente ontwikkelingen in de chemische industrie met als doel het bouwen van efficiëntere chemische installaties zetten steeds meer ingenieurs en fysici aan tot de ontwikkeling en het gebruik van regeltechnische modellen van materiaaleigenschappen in reactoren. Het modelleren vanuit een regeltechnisch perspectief biedt een nieuwe manier van denken over de toepassing van modellen in de chemische industrie, de relaties tussen de eigenschappen van het materiaal in de chemische reactoren en het niveau van de details die nodig zijn voor het ontwerpen van een regelaar.

De belangrijkste bijdrage van dit proefschrift is het ontwerp van een uniforme set van regels en voorwaarden voor de regeltechnische modelvorming van vloeistofsystemen in de chemische industrie. Naast het gebruik van de fysica van vloeitstofsystemen en de constructie van modellen op basis van fundamentele natuurkundige wetten worden er eisen opgesteld die nodig zijn voor de constructie van causale ingang-uitgang structuren en ruimtelijk gedistribueerde regelontwerpen.

Het eerste deel van dit proefschrift heeft betrekking op de microscopische modelvorming van een vloeistofstroomsysteem en de eisen die nodig zijn om een regeltechnisch model te verkrijgen. De afleiding van een regeltechnisch model kan veeleisend zijn wanneer de dynamiek van een bepaald vloeistof regime expliciet moet worden bepaald. De complexiteit wordt geïllustreerd aan de hand van de Navier-Stokes vergelijkingen en de verschillende beschikbare discretisatiemethoden voor een eenfase stromingssysteem met een eenvoudige geometrie — het zogenaamde lid-driven cavity systeem — waarvan het principe kan worden teruggevonden in een breed scala aan industriële toepassingen. De conventionele oplossingsmethoden van het microscopische stromingsmodel gaan uit van een fijne discretisatie. De uit een fijne discretisatie verkregen microtoestanden kunnen vervolgens worden geanalyseerd en gemanipuleerd. Ondanks het feit dat de microtoestanden een zeer gedetailleerd beeld geven van de stroming zijn deze over het algemeen niet direct te meten. Daarom moeten verschillende modelvormingsschalen worden beschouwd voor het ontwerpen van ruimtelijk gedistribueerde regelontwerpen. De toepasbaarheid van de multischaal modelvormingsaanpak van een stromingssysteem wordt aangetoond door middel van een macroscopische uitgangsregelaar van het lid-driven cavity systeem.

Het tweede deel van dit proefschrift behandelt de constructie van een regeltechnisch model van een tweefasen stromingssysteem. Dit model is complementair aan het eenfase stromingsmodel zoals behandelt in het eerste deel. Vanuit de multischaal modelvormingsaanpak wordt een vereenvoudigd model op basis van fundamentele natuurkundige wetten opgesteld en vervolgens wordt de dominante dynamica bestudeerd. Op basis van het verkregen regeltechnisch model worden de verschillende stroomregimes in een bubbelkolom reactor onderzocht door vloeistof op verschillende plaatsen te injecteren. Als uitkomst van deze studie worden verschillende ruimtelijk gedistribueerde regelontwerpen voor de tweefasen stroming binnen de bubbelkolom reactor voorgesteld. Deze gedistribueerde regelontwerpen kunnen worden gebruikt om de tweefasen stroming te stabiliseren of te destabiliseren rond een gewenst stromingsregime. Naast het gebruik van het regeltechnisch model van de tweefasen stroming in een bubbelkolom voor het ontwerpen van een regelaar kan het ook bijdragen aan nieuwe reactorontwerpen gebaseerd op de meest efficinte actuatiestrategien.

In het algemeen spelen de stabilisatie en destabilisatie van een vloeistofstroming een cruciale rol bij het ontwerpen van efficinte en duurzame processen die afhankelijk zijn van de manipulatie van vloeistof-dynamica. De ruimtelijk gedistribueerde regelontwerpen van de stromingssystemen zoals gepresenteerd in dit proefschrift suggereren efficinter reactor ontwerpen en nieuwe ontwikkelingen in de procesintensivering in de chemische industrie.

About the Author

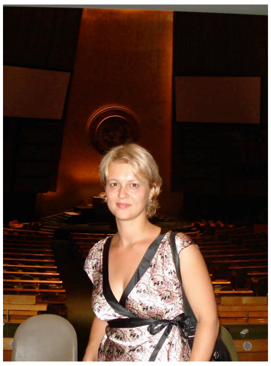

Snezana Djordjevic was born in Novi Sad, Serbia. She studied Bioprocess Engineering at the University of Novi Sad, Serbia, where she obtained the 5-year Engineer Degree in 2001. In 2005, she obtained her M.Sc. Degree in Process Technology from Wageningen University, The Netherlands. Her graduation thesis was entitled “Consequences of Model Errors in Optimal Operation Strategies, and was supervised by Dr.ir. Ton van Boxtel and Dr.ir. Hans Stigter. Since 2006, Snezana Djordjevic has been working on the Ph.D. thesis “Model-Based Control of Hydrodynamics of Bubble Columns” at Delft Center for Systems and Control, Delft University of Technology, The Netherlands. Under the supervision of Prof.dr.ir. Paul Van den Hof and Prof.ir. Okko Bosgra, she has worked on developing a control-oriented model of two-phase fluid systems. During her Ph.D. research, Snezana Djordjevic was a visiting scholar at the Dynamic Systems & Control group, University of California San Diego, U.S.A. Currently, she is with the Control System Technology group at the Faculty of Mechanical Engineering, Eindhoven University of Technology, The Netherlands, working on nuclear fusion.